Near–wall dynamics of colloidal particles studied by evanescent wave dynamic light scattering

Inaugural dissertation

for the attainment of the title of doctor
in the Faculty of Mathematics and Natural Sciences
at the Heinrich Heine University Düsseldorf

presented by

Yi Liu
from Gansu, China

Jülich, October 2016

from the institute for Complex Systems (ICS-3)
at the Forschungszentrums Jülich

Published by permission of the
Faculty of Mathematics and Natural Sciences at
Heinrich Heine University Düsseldorf

Supervisor: PD Dr. Peter R. Lang
Co-supervisor: Prof. Dr. Matthias Karg

Date of the oral examination: 09/12/2016

Preface

Part of the work presented in this thesis is already published in peer-reviewed international journals. In the following, I list all these publications, specify my personal contributions therein, and denote where a specific publication is used in the thesis.

1. **Near-wall dynamics of concentrated hard-sphere suspensions: comparison of evanescent wave DLS, virial approximation and simulations**
   Y. Liu, J. Bławzdziewicz, B. Cichocki, J K. G. Dhont, M. Lisicki, E. Wajnryb, Y.-N. Young and P R. Lang, *Soft matter* **11**, 7316-7327 (2015).
   I performed all the experiments, and I did all the data analysis and fitting of the experimental data presented in the paper, supported by helpful discussion with P. Lang. The manuscript was jointly written by P R. Lang, M. Lisicki, J. Bławzdziewicz and me.
   The content of this article is used in Chapter 4.

2. **A combined 3D and 2D light scattering study on aqueous colloidal model systems with tunable interactions**
   Y. Liu, N. Claes, B. Trepka, S. Bals and P R. Lang, *Soft Matter* Advance Article (2016).
   The synthesis and bulk characterization shown in this paper were jointly performed by B. Trepka and me. The cryo-TEM was performed by N. Claes and S. Bals in University Antwerp. The bulk and near-wall light scattering experiments, and the data analysis and fitting were performed by me. The manuscript was jointly written by P R. Lang and me.
   The content of this article is used in Chapter 5.

3. **Self-organization and encapsulation behavior of polyurethane pre-polymers**
   Y. Liu, and P R. Lang, in preparation (2016).

I did all the experiments and the data analysis. The manuscript in preparation is written by me.
Results in this manuscript in preparation are used in Chapter 6.

Abstract

This work focuses on the Brownian motion of suspended spherical colloidal particles in the ultimate vicinity of liquid-solid interfaces (particle-interface distance comparable to particle size), using evanescent wave dynamic light scattering (EWDLS) as the main experimental technique. The motion of particles close to interface is an essential feature in the studies of colloidal science. It is highly relevant to many biological processes and industrial applications like coatings, and it is an intriguing subject from the fundamental point of view. Three colloidal systems are studied here: a simple hard sphere (HS) model system, an aqueous model system with electrostatic interaction, and finally, an industrial aqueous colloidal system.

The near-wall dynamics of the hard sphere model system are studied over a broad range of volume fraction. Collaborating with theoreticians, we could provide a thorough comparison of experimental data with predictions based on virial approximation and numerical simulation. We find that the experimental results up till a volume fraction of $\phi \approx 25\%$ can be well described by virial approximation, and at higher volume fraction (e.g. $\phi \approx 30\%$) by numerical simulation. This on the one hand validates EWDLS as a reliable experimental technique for the study of near-wall dynamics, on the other hand shows that virial approximation is a fast and non-costly tool for analysis and prediction of EWDLS data. With this it is possible to obtain reliable values for the particles' near-wall self-diffusion coefficient, D_S, as a function of concentration. In qualitative agreement with earlier work, we observe that the near-wall value of D_S approaches the bulk value with increasing particle volume fraction. However we find that this effect is less pronounced than indicated earlier and we can show that the effect is different for the directions parallel and normal to the wall at constant volume fraction. The comparison and agreement between experimental result and theoretical prediction in the case of the HS suspension has paved the road for future studies on more complicated systems.

In the next step, the focus is shifted to an aqueous model system with electrostatic repulsive interaction. For this purpose, polyethyleneglycol grafted fluoroacrylate particles (PEGylated FBMA) are synthesized through emulsion polymerization and characterized with various methods, which show that the particles are mono-disperse, stable, and can be refractive index matched to aqueous solvent mixtures. This enables us to conduct light scattering measurements at higher particle volume fraction. Static and dynamic light scattering experiments in combination with cryo transmission electron microscopy reveal that the particles have a core-shell structure with a significant enrichment of the PEG chains on the particles' surface. In index-matching DMSO/water solvent the particles start to arrange into an ordered phase at volume fraction above 7%, if no additional electrolyte is present. The near-wall dynamics at low volume fraction and various salt concentrations are quantitatively described by the combination of electrostatic repulsion and hydrodynamic interaction between the particles and the wall. At volume fractions close to the isotropic-to-ordered transition ($\phi \approx 7\%$), the near-wall dynamics are more complex and qualitatively comparable to the behavior that has been observed in hard sphere suspensions at high concentrations ($\phi \approx 30\%$).
Finally, the bulk properties and the near-wall dynamics of an industrial colloidal system – polyurethane pre-polymer particles – are studied. Polyurethane pre-polymers are oligomers consisting of charged and hydrophobic units. They are shown to self-organize into colloidal particles with radius of approximately 10 nm, due to their amphiphilic nature. Moreover, such amphiphilic pre-polymers are able to encapsulate the hydrophobic (charge free) counterparts, and form colloidal particles with radius of about 130 nm. In bulk experiments, the encapsulation properties of two types of amphiphilic pre-polymer are compared, i.e. a system with random composition and a system with uniform composition that has been molecularly designed to show optimal encapsulation efficiency. The results indicate that the system with uniform composition indeed performs better than the random one in terms of encapsulation.
EWDLS is applied to suspensions of encapsulated particles. Experiments have been performed at different electrolyte concentrations to tune the electrostatic repulsion between the wall and the encapsulates. The dependence of near-wall dynamics on ionic strength is not conclusive. However, in all cases it is observed that the near-wall diffusion of PU particles is much slower than expected for hard sphere systems. This indicates significant attractive interaction between the particles and the wall outbalancing electrostatic repulsion, which is favorable for coating applications.

Zusammenfassung

In meiner Arbeit habe ich mich in erster Linie mit der Brownschen Dynamik suspendierter sphärischer, kolloidaler Partikel in der unmittelbaren Nähe einer flüssig-fest Grenzfläche, d. h. in der Nähe einer Wand, beschäftigt. Dazu benutze ich dynamische Lichtstreuung mit evaneszenter Beleuchtung (EWDLS) als wichtigste experimentelle Methode. Die Beweglichkeit von Partikeln ist eine wichtige Eigenschaft kolloidaler Suspensionen. Sie spielt eine wichtige Rolle in vielen biologischen Prozessen und auch in industriellen Anwendungen, wie z. B. Beschichtungen, und sie ist ein faszinierendes wissenschaftliches Thema.
Nach Untersuchungen am denkbar einfachsten Modelsystem quasi harter Kugeln (HS), die nur durch ihr ausgeschlossenes Volumen wechselwirken, wurden die Experimente auf ein System mit langreichender elektrostatischer Wechselwirkung erweitert. Die Arbeit wurde komplettiert durch Untersuchungen an einem System das für industrielle Beschichtungsanwendungen getestet wird.
Die grenzflächennahe Dynamik des HS Systems wurde über einen weiten Bereich von Partikelvolumenbrüchen untersucht. In Zusammenarbeit mit theoretisch arbeitenden Kollegen konnten wir einen gründlichen Vergleich zwischen experimentellen Daten, einer näherungsweisen theoretischen Voraussage, die auf einer Virialreihenentwicklung beruht, und Computersimulationen durchführen. Wir fanden, dass die Virialreihenentwicklung die experimentellen Daten bis zu Partikelvolumenbrüchen von fast 25 Prozent richtig beschreibt. Erst bei Volumenbrüchen von 30 Prozent und mehr, ist es erforderlich auf aufwändige Simulationen zurückzugreifen. Dieser Vergleich zeigt zum einen, dass EWDLS eine zuverlässige Methode zur Untersuchung von grenzflächennaher Kolloiddynamik ist. Andererseits steht uns mit der Virialnäherung eine zuverlässige und schnelle Methode zur Verfügung, den Kurzzeit-Selbstdiffusionskoeffizienten D_S der Partikel in der Nähe der Wand zu bestimmen. Es zeigte

sich, dass dieser sich mit zunehmender Partikelkonzentration dem Volumenwert annähert, wie das in den früheren Arbeiten schon gefunden worden war. Allerdings erscheint dieser Effekt wenige ausgeprägt als früher beobachtet, und außerdem fanden wir dass er unterschiedlich stark ausgeprägt ist, für Bewegungen parallel und senkrecht zur Wand.
Dieser erfolgreiche Vergleich zwischen experimentellen Daten und theoretischen Voraussagen für HS Suspensionen, hat nun den Weg für Untersuchungen an komplexeren Systemen geebnet.
Im nächsten Schritt habe ich mich einem wässrigen Modellsystem zugewandt, indem die Kolloide durch elektrostatische Abstoßung wechselwirken. Dazu wurden Polyethylenglycol - beschichtete Fluoracrylat-Partikel (PEG-FBMA) mittels Emulsionspolymerisation synthetisiert und mit verschiedenen Methoden charakterisiert. Die Partikel sind monodispers, zeigen eine hohe kolloidale Stabilität und ihr Brechungsindex ist so niedrig, dass derjenige von wässrigen Lösungsmittelmischungen daran angepasst werden können. Letzteres erlaubt Lichtstreumessungen (LS) bei beliebiger Partikelkonzentration. Statische und dynamische LS-Messungen zeigten in Kombination mit Cryo-Transmissionselektronenmikroskopieaufnahmen, dass die Partikel eine sphärische Kern-Schale Struktur haben, wobei eine deutliche Anreicherung des PEG in der Schale auftritt. In einer DMSO/Wasser Mischung, deren Brechungsindex an den der Partikel angepasst ist, ordnen sich die Partikel zu einer kristallinen Phase, bei Volumenbrüchen über 7%, wenn kein zusätzlicher Elektrolyt zugesetzt wird. Die grenzflächennahe Dynamik dieser Partikel bei hoher Verdünnung und unterschiedlichen Salzkonzentrationen kann quantitative durch eine Kombination aus elektrostatischer Abstoßung und hydrodynamischer Wechselwirkung zwischen Wand und Partikeln beschrieben werden. Bei Partikelkonzentrationen, nahe am Übergang zur geordneten Phase ist die Dynamik komplexer und qualitativ ähnlich zu dem Verhalten, das in HS Systemen bei hohen Konzentrationen beobachtet wurde.
Abschließend untersuchte ich die Eigenschaften im Volumen und die grenzflächennahe Dynamik eines industriellen Kolloidsystems - kolloidale Polyurethanaggregate die für die Anwendung in wasserbasierten Beschichtungen entwickelt worden waren. Die Polyurethan Präpolymere (PU-PP) sind aus geladenen und hydrophoben Monomeren zusammengesetzt. Aufgrund ihres amphiphilen Charakters aggregieren PU-PP zu kolloidalen Partikeln mit einer Größe von etwa 10 Nanometern. Außerdem können solche amphiphilen Präpolymere hydrophobe (nicht geladene) Analoga einschließen und so solubilisieren, was zu Partikeln mit Radien in der Größenordnung von hundert Nanometern führt. In Volumenexperimenten habe ich die Solubilisierungseigenschaften von zwei Arten amphiphiler Präpolymere untersucht. Zum einen ein Polymer mit einer zufälligen Abfolge von Monomeren und zum anderen ein Polymer dessen Monomerzusammensetzung und -abfolge maßgeschneidert war, um seine Solubilisierungef-

fektivität zu optimieren. Meine Ergebnisse geben einen ersten experimentellen Hinweis, dass das maßgeschneiderte Polymer tatsächlich bessere Solubilisierungseigenschaften hat als das mit der zufälligen Monomerabfolge.

Um die grenzflächennahe Dynamik dieser Aggregate zu untersuchen wurden EWDLS-Experimente an Partikeln durchgeführt, die aus einem hydrophoben PP und einem amphiphilen PP mit zufälliger Zusammensetzung bestehen. Die Experimente wurden bei verschiedenen Konzentrationen zusätzlicher Elektrolyte durchgeführt, um die elektrostatische Abstoßung zwischen der Wand und den Aggregaten zu variieren. Allerdings konnte ich keinen eindeutigen Trend der dynamischen Eigenschaften mit der Variation der Salzkonzentration feststellen. Stattdessen beobachtete ich in allen Fällen, dass die grenzflächennahe Dynamik der PU-PP Aggregate sehr viel langsamer war, als es für harte Kugel Systeme vorausgesagt wird. Dies weist darauf hin, dass es attraktive Wechselwirkungen zwischen Partikeln und Wand gibt, die die elektrostatische Abstoßung überkompensieren, was für die Anwendung dieser Partikel in Beschichtungsprozessen vorteilhaft ist.

Contents

1 Introduction

I would like to start this thesis by presenting an actual problem in coating industry. Water-borne coating has become increasingly popular as an eco-friendly alternative to the traditional counterpart. Such water-borne coating in essence is an aqueous colloidal dispersion, the volume fraction and interaction range of which change with application stages. As coating is a highly interface related process, the dynamics of the colloids at interface, in particular at a solid planar substrate, is worth investigation. In order to understand the problem, first of all, a sensitive and reliable experimental method for the study of interface dynamics that can provide good statistics is needed; second, a supporting theory to describe and predict the experiments has to be found; third, a well defined model system to mimic the industrial sample is required, that we can tune the volume fraction and interaction range in a controlled manner; finally, we can test the method on the real industrial sample, based on what we've learned from the model system, if necessary, with modification and approximation.
And this is what the thesis – Near-wall dynamics of colloidal particles studied by evanescent wave dynamic light scattering – is going to inquest and discuss. However, before starting, a general introduction is necessary, to give a broader perspective on the topic.

1.1 Background

Soft matter at interfaces has acquired a growing attention from scientific community and industry during recent years. [1–3] The spectrum of topics spans fundamental scientific subjects like particle stabilized emulsions [4], protein stability and adsorption [5] or self-assembly at water-oil interface [6] for the fabrication of functional nano-films, with industrial applications such as corrosion protection [7] or water-borne 'green' coatings [8], to name a few.

Dynamics of colloidal particles at interfaces is an important feature throughout this spectrum of topics, especially when the dimension of confining geometries is approaching that of the particles. Some examples are: microfluidics and 'lab-in-chip' applications, where the Brownian motion of particles is largely influenced by the surrounding microstructure [9]; emulsion stabilization, where colloidal particles bind to the liquid interface dynamically [10, 11]; and many biological processes, as in the case of bacteria biofilm: knowing how free-swimming bacteria adapt their mobility mechanism near surfaces is crucial for understanding the transition between planktonic and biofilm phenotypes [12, 13]. While there is a plethora of publications considering static properties as interaction forces, structure and phase behavior of particles at interfaces. e. g. [14–17] and references cited therein, there are comparatively few contributions reporting on experimental investigations of particle dynamics in the ultimate vicinity of interfaces [18–29].

Interfaces between a solid and a liquid phase are of particular technological importance e. g. in coating processes or bio-film formation. In these cases the motion of the particles close to the wall is slowed down due to hydrodynamic interaction and this hindrance (wall drag effect) differs for particles moving parallel and perpendicular to the wall [30, 31]. The interplay between static particle-wall interaction and the dynamic wall drag effect has significant implications on potential applications. For example, geometrical constraints were used to quench Brownian rotational motion of spherical Janus particles providing a means to steer their trajectory [32]. Also the trajectories of active swimmers, which are driven by flagellar motion can be directed by tuning their interaction with a surface and spatial confinements can be used to accumulate active swimmers [33]. For a targeted exploitation of the combined effects of static interaction, the wall drag effect and particle concentration, the fundamental understanding of their mutual interplay is much needed.

Microscopy based technique is one important experimental method to observe this quenched Brownian motion at interface. Direct measurements of constrained diffusion of an isolated uncharged PMMA sphere in a density-matched fluid confined between two parallel flat walls have been conducted using video microscopy in combination with optical tweezers. [34] The three-dimensional anisotropic hindered diffusion of freely suspended micron-sized fluorescent particles has been observed by applying the three-dimensional total internal reflection velocimetry (3D-TIRV) technique. [35] Anisotropic diffusion of colloidal particle at wall has been measured and compared to the prediction. [36] However, three major problems remain. First, it is difficult if not impossible to study particles with sub 100 nm radius, even with the most advanced microscopy technique; second, it is hard to resolve motion of one particle within a high number density system, where particles start to 'feel' each other. Moreover, it

is time-consuming to obtain good statistics by microscopy, which is especially important for industrial applications.

Facing these challenges, light scattering appears as a complementary method for the study of near-wall dynamics of colloids. In this case, a surface-sensitive non-homogeneous evanescent wave is used as illumination source, hence the name 'evanescent wave dynamic light scattering'. The technique was first devised by Lan *et al.* in 1986 [37], and has been advanced constantly and rapidly since then. The principle is as follows: an evanescent wave is created when a laser beam is totally reflected off at interface (glass-liquid, or liquid-liquid); particles within the illumination profile will scatter light, which is then collected by a detecting unit; the signal is processed by a correlator to generate the intensity correlation function. The penetration depth of evanescent wave can be tuned by varying incident angle of the laser beam. Being a scattering technique, EWDLS allows the measurement of particles within radius range from 50 nm to 100 nm, and at the same time provides good statistics. Modern instrumentation has made it possible to independently vary scattering vectors ($Q_{\parallel}$ and $Q_{\perp}$) and hence to distinguish between the anisotropic diffusivity of colloids parallel and perpendicular to the interface experimentally. EWDLS has also been employed to study the rotational diffusion of optically anisotropic particles [38], to probe the particle dynamics at liquid-liquid interfaces [39], and to measure the near-wall velocity profile with a resolution of tens of nanometer [40].

1.2 Scope of the thesis

In this thesis, the application of EWDLS to investigate colloidal near-wall dynamics in a variety of systems is discussed. The work goes beyond the current start of art in the following aspects:

1. Although the near-wall dynamics of hard sphere suspensions have been extensively studied, a systematic studies are lacking, and cases for high volume fraction are not yet conclusive. Hence, we present a thorough and systematic study of near-wall dynamics for hard sphere system, combining EWDLS experiment, theory and simulations.
2. We conduct the first EWDLS measurements on an aqueous system with long ranging interaction at and exceeding the concentration of order–disorder transition.
3. We perform EWDLS measurements on a colloidal system which is relevant for industrial applications.

The thesis is structured as follows:

In Chapter 2, some fundamental concepts and principles are introduced. First, the fundamen-

tals of bulk light scattering, i.e. dynamic light scattering (DLS) and static light scattering (SLS) are introduced. Secondly, Brownian motion of colloidal particles close to at planar wall is discussed. Finally, the principles of evanescent wave dynamic light scattering for the study of near-wall dynamics are introduced.

Chapter 3 illustrates the main experimental method to be used in this thesis: evanescent wave dynamic light scattering (EWDLS). The instrumentation, data analysis, and experimental error are discussed in detail.

In Chapter 4, EWDLS studies on the simple hard sphere model system are presented. Volume fractions are systematically varied, from very diluted regime, up till as high as 30%. Experimental results are compared with both theoretical prediction and simulation. We are trying to, first, prove that EWDLS is a reliable and sensitive technique for the study of near-wall dynamics; then build up a framework of understanding, which will help us comprehend more complicated systems.

In Chapter 5, bulk light scattering and EWDLS studies on a novel aqueous model system are presented. To meet the light scattering criteria, we have synthesized mono-disperse latex particles with low refractive index, tunable electrostatic interaction and extra stability. Systematic bulk scattering measurements have been conducted in order to obtain information on the structure and bulk dynamics of the system. Finally, the near-wall dynamics of the aqueous system are investigated by EWDLS, varying both volume fraction and ionic strength.

In Chapter 6, bulk light scattering and EWDLS studies on an industrial aqueous system – polyurethane (PU) pre-polymer particles – are presented. To start with, the self-organization behavior of amphiphilic polyurethane pre-polymers is studied by SLS, DLS and small angle X-ray scattering. In the next step, the encapsulation efficiency of amphiphilic pre-polymers (over the hydrophobic pre-polymers) and the properties of the encapsulated particles are investigated by SLS and DLS. Finally, the near-wall dynamics of the encapsulated PU particles are studied by EWDLS. The measurements are conducted on diluted particle suspensions, at different ionic strength.

2 Fundamentals

This chapter will line out the fundamental theoretical concept of bulk light scattering, Brownian motion at planar interface, and the light scattering with evanescent illumination for the study of near-wall Brownian motion.

2.1 Light scattering in bulk

Light scattering is a widely applied technique for the investigation of bulk dynamics (dynamic light scattering) and bulk structure (static light scattering) of particles in liquid suspension.

2.1.1 Static light scattering

Static light scattering (SLS) measures the mean scattering intensity as a function of scattering angles θ, which at fixed wavelength λ, sets the magnitude of scattering vector Q.

$$I(\mathbf{Q}) = \langle i(\mathbf{Q},t)\rangle \tag{2.1}$$

The brackets denote ensemble averaging over the orientations and positions of Brownian particles. In an experiment, the ensemble average is attained through time average, with a time interval much larger than the time required for the Brownian particles to probe all accessible configuration. For ergodic systems the time average may be replaced by the number average. for solution of identical colloidal particles, the scattered intensity can be written as

$$I(\mathbf{Q}) \propto \mathbf{E}_S^2 = \left| \int_{V_j^0} f(\mathbf{r}') \exp\{i\mathbf{Q}\mathbf{r}'\} \mathrm{d}\mathbf{r}' \right|^2 \left| \sum_{j=1}^{N} \exp\{i\mathbf{Q}\mathbf{r}_j\} \right|^2 \tag{2.2}$$

where the scattering vector is defined as the difference between the wave vector of the scattered and the illuminating beam $\mathbf{Q} = \mathbf{k}_s - \mathbf{k}_I$, $\mathbf{r}_j$ is the vector pointing from an arbitrarily chose origin to the center position of the j^{th} particle and $\mathbf{r}'$ points from the center position to any arbitrary point within the particle. V_j^0 is the actual volume of j^{th} particle. $f(\mathbf{r}')$ is the scattering power. We can see that 2.2 contains one factor which depends on the position of particle, and another factor which depends on the scattering power and the distances within a particle. The former term is related to the solution structure factor

$$S(Q) \equiv \frac{1}{N}\left\langle \left| \sum_{j=1}^{N} \exp\{i\mathbf{Q}\mathbf{r}_j\} \right|^2 \right\rangle \tag{2.3}$$

is called the structure factor of a solution, while the latter is equal to the particle form factor, apart from a normalization constant.

$$P(Q) \equiv \left\langle \left| \frac{\int_{V_j^0} f(\mathbf{r}') \exp\{i\mathbf{Q}\mathbf{r}'\} \mathrm{d}\mathbf{r}'}{\int_{V_j^0} f(\mathbf{r}') \mathrm{d}\mathbf{r}'} \right|^2 \right\rangle \tag{2.4}$$

The angular brackets indicates that the experiments measure the time-averaged quantities. eq.2.2 can be written as

$$I(Q,N) \propto \left(\int_{V_j^0} f(\mathbf{r}') \mathrm{d}\mathbf{r}' \right)^2 P(Q) N S(Q) \tag{2.5}$$

where Q is the magnitude of the scattering vector. The magnitude of the scattering vector as the function of the scattering angle θ reads,

$$Q = \frac{4\pi}{\lambda} sin\frac{\theta}{2} \tag{2.6}$$

From the above definition 2.3 and 2.4, one can see that in the limit of the particle number N approaching 0, as in the case of infinite dilution, structure factor $S(Q)$ approaches unity; and in the limit of Q approaching 0, the particle form factor $P(Q)$ approaches unity. Therefore, the following approximation can be made to experimental data

$$\begin{gathered} \lim_{N\to 0} I(Q,N) \propto P(Q) \\ and \\ \lim_{Q\to 0} I(Q,N) \propto S(Q=0) \end{gathered} \tag{2.7}$$

The scattered intensity in absolute units is often expressed in terms of the so called Rayleigh ratio

$$R(Q) \equiv \frac{I(Q)}{I_I}\frac{d_{SD}}{V_s} = f_o \phi V_p P(Q) S(Q) \tag{2.8}$$

in honor of Lord Rayleigh who first wrote down the scattering equation for an ideal gas in 1871. Here I_I is the primary beam intensity, d_{SD} the sample to detector distance, V_s the observed scattering volume, ϕ the solute volume fraction and V_p is the volume of single solute particle. The factor $V_s I_I / d_{SD}$ in the expression is an apparatus constant, which makes Rayleigh ratio solely dependent on properties of the system.
In the field of colloid physics, as we are discussing here, f_0 is represented as,

$$f_o = \frac{k_I^4}{16\pi^2}\left|\frac{\varepsilon_p - \varepsilon_S}{\varepsilon_S}\right|^2 \tag{2.9}$$

Here $k_I = 2\pi n_{sol}/\lambda_0$ is the wave vector of the incident beam in the sample solution with λ_0 the vacuum wavelength of the illuminating laser and n_{sol} the refractive index of the solution. The dielectric constants of the solute particles and of the solvent are ε_p and ε_S respectively. The factor,

$$C = \left|\frac{\varepsilon_p - \varepsilon_S}{\varepsilon_S}\right| \tag{2.10}$$

is usually called optical contrast of Brownian particles.
For optically homogeneous spherical particles, which have a dielectric constant independent of the position within the particle, the form factor can be calculated as:

$$P(Q) = \left[3\frac{Qacos\{Qa\} - sin\{Qa\}}{(Qa)^3}\right]^2 \tag{2.11}$$

where a denotes the radius of colloidal particle.
To obtain $S(Q, \phi = x)$ of a particle dispersion X at volume fraction ϕ_x from static light scattering experiment, we need the Rayleigh ratio $R(Q, \phi = x)$ of sample at ϕ_x and the Rayleigh ration $R(Q, \phi = 0)$ of sample at very low density where phi_0 approaches 0. If we divide the $R(Q, \phi = x)$ with $R(Q, \phi = 0)$,

$$\frac{R(Q, \phi = x)}{R(Q, \phi = 0)} \approx \frac{\phi_x}{\phi_0} \cdot \frac{P(Q, \phi = x)}{P(Q, \phi = 0)} \cdot \frac{S(Q, \phi = x)}{S(Q, \phi = 0)} \tag{2.12}$$

Both Rayleigh ratios can be obtained from SLS experiments. At low density ϕ_0, the structure factor $S(Q, \phi = 0)$ of particle dispersion is approaching unity. Particles' form factor doesn't depend on the volume fraction, $P(Q, \phi = 0) = P(Q, \phi = x)$. Hence, structure factor of sample

X $S(Q,\phi = x)$ can be written as,

$$S(Q,\phi = x) \approx \frac{R(Q,\phi = x)}{R(Q,\phi = 0)} \cdot \frac{\phi_0}{\phi_x} \tag{2.13}$$

2.1.1.1 Application in polymer science

Up so far, static light scattering has been discussed from the point of view of colloidal physics, with an according representation. Static light scattering is also widely applied in the field of polymer sciences, where the same principles are applied, but different representation is required. Here, the contrast factor f_0 is more popularly written as,

$$f_o = \frac{k_0^4 4 n_S^2}{16\pi^2 N_A} \left(\frac{\partial n}{\partial c}\right)^2 M_r c \tag{2.14}$$

where $k_0 = 2\pi/\lambda_0$ is the wave vector of the incident beam in vacuum, n_S the refractive index of the solvent, N_A is Avogadro's constant, M_r the polymer molar mass, c the polymer concentration in units of mass/volume and $\partial n/\partial c$ is the incremental change of the solution's refractive index with increasing concentration. Using $n = \sqrt{\varepsilon}$, $k_I = k_0 n$ and $\partial n/\partial c \approx (\varepsilon_p - \varepsilon_S)^2/\rho_m^2$ with the solute particle mass density, ρ_m, the two representations can be transformed into each other easily. Further, it is a widely used procedure in polymer science to analyze scattering data, applying the low scattering vector and low concentration limit of the structure factor and the form factor. The limit

$$\lim_{Q\to\infty, c\to 0} \frac{1}{S(Q)} = \frac{\partial \Pi}{\partial \aleph} \frac{1}{k_B T} \approx 1 + 2A_2 c M_r \tag{2.15}$$

connects $S(Q=0)$ to the osmotic pressure of the system, Π at a given number density, $\aleph$ and the second osmotic virial coefficient, A_2, while the limit

$$\lim_{Q\to 0} \frac{1}{P(Q)} = 1 + \frac{Q^2 R_g^2}{3} \tag{2.16}$$

relates the angular dependence of the scattered intensity to the particles' radius of gyration. R_g. The combination of these limiting expressions with eqs. 2.8 and 2.14 leads to the Zimm equation

$$\frac{Kc}{R(Q,c)} = \frac{1}{M_r}\left(1 + \frac{Q^2 R_g^2}{3}\right) + 2A_2 c \tag{2.17}$$

where $K = f_o/M_r c$.

2.1.2 Dynamic light scattering

Dynamic light scattering is a standard technique to study Brownian motion of particles in bulk, where the effect of geometrical constraints is negligible. When a laser beam shines through a suspension, particles within the illuminated volume will scatter light. The observed intensity of this scattered light fluctuates since particles are undergoing Brownian motion constantly. This intensity trace is recorded and the autocorrelation function is generated as follows:

$$g_2\langle \mathbf{Q},t\rangle = \frac{\langle I(t)I(t+\tau)\rangle}{\langle I(t)\rangle^2} \tag{2.18}$$

Where $g_2(\mathbf{Q},t)$ is the intensity autocorrelation function, the pointed bracket indicate an average over particle ensembles, and Q is the scattering vector. The intensity auto-correlation function $g_2(\mathbf{Q},t)$ can be related to the field auto-correlation function $g_1(\mathbf{Q},t)$ through the Siegert relation:

$$g_2(\mathbf{Q},t) = 1 + Ag_1(\mathbf{Q},\tau)^2 \tag{2.19}$$

where A is a factor of order unity, which accounts for the temporal and spatial integrations which are inevitable in real experiments. [41] For a detailed derivation of the relation between particles' dynamic properties with the experimentally observable correlation function, the reader is referred to standard textbooks [42]

In the case of diluted suspensions of monodisperse particles, the field correlation function can be written as:

$$g_1(\mathbf{Q},t) = \exp\{-Q^2D_0t\} \tag{2.20}$$

Therefore, the field auto-correlation function can be seen as an exponential decay with a decay rate $\Gamma = -Q^2D_0$, modulated by the free diffusion coefficient D_0 and the square of scattering vector. To obtain information on particles' Brownian motion, in practice, the decay rates are determined by fitting the correlation function with an appropriate model function and plotted versus Q^2. This yields a linear relation with zero intersect and a slope which is equal to D_0. Further more, the hydrodynamic radius of the particles can be calculated through the Stokes-Einstein relation, for a given temperature T and a solvent viscosity η:

$$R_H = \frac{k_BT}{6\pi\eta D_0} \tag{2.21}$$

As the particle number density increases, particles' motion starts to be affected by other particles, through hydrodynamic interaction mediated by surrounding solvent. In this case the correlation function may still exhibit a single exponential decay, but the relaxation rates will

not anymore depend linearly on Q^2 and the diffusion can no longer be described by a constant value D_0, rather a function $D(Q)$, which can be described as

$$D(Q) = Q^2 \cdot \frac{H(Q)}{S(Q)} \tag{2.22}$$

where $H(Q)$ is the so called 'hydrodynamic function' and $S(q)$ is the static structure factor. [43] The hydrodynamic function is related to hydrodynamic mobility μ_{ij} as,

$$H(Q) = \frac{1}{\mu_0 N} \sum_{ij}^{N} < \hat{\mathbf{Q}} \cdot \mu_{ij} \cdot \hat{\mathbf{Q}} \cdot exp\{i\mathbf{Q} \cdot (r_i - r_j)\} > \tag{2.23}$$

where N is the total number of particles within the scattering volume, $\hat{Q}$ is the unit vector in the direction of Q, the brackets <...> refers to the ensemble average, and r_k is the position of the center of particle k. The hydrodynamic mobility coefficient μ_{ij} may be interpreted as inverse friction coefficients relating the velocity a particle obtains due to a force which is exerted on another particle ,

$$U_i = \mu_{ij} \cdot F_j \tag{2.24}$$

where U_i is the velocity of particle i due to the force F_j applied to particle j. The static structure factor which is defined in eq. 2.3, can be independently obtained from static light scattering measurements, as discussed in the previous section.

2.1.2.1 Polydispersity

For particle suspensions with polydispersity, $g_1(\mathbf{Q},t)$ can no longer be represented as a single exponential, but rather as a sum or an integral over a distribution of relaxation rates $G(\Gamma)$,

$$g_1(\mathbf{Q},t) = \int_0^\infty G(\Gamma) \exp(-\Gamma t)\, \mathrm{d}\Gamma \tag{2.25}$$

where $G(\Gamma)$ is normalized such that

$$\int_0^\infty G(\Gamma)\, \mathrm{d}\Gamma = 1 \tag{2.26}$$

One common way to characterize $G(\Gamma)$ from DLS data is the cumulant analysis, first proposed by Kopple. [44] The cumulant expansion re-writes a sum of exponential decay functions as a

power series expansion. First of all, the average relaxation rate $< \Gamma >$ is defined as

$$\langle \Gamma \rangle = \int_0^\infty G(\Gamma)\Gamma \, \mathrm{d}\Gamma \tag{2.27}$$

Then, $g_1(\mathbf{Q},t)$ (Eqa. 2.25) can be rewritten as

$$g_1(\mathbf{Q},t) = \int_0^\infty G(\Gamma)\exp(-\langle\Gamma\rangle)\cdot\exp\{-(\Gamma-\langle\Gamma\rangle)\}\,\mathrm{d}\Gamma \tag{2.28}$$

If we replace the difference term $\exp\{-(\Gamma-\langle\Gamma\rangle)t\}$ with a power series, $g_1(\mathbf{Q}.t)$ can be further written as

$$g_1(\mathbf{Q},t) = \int_0^\infty G(\Gamma)\exp(-\langle\Gamma\rangle t)\left[1-(\Gamma-\langle\Gamma\rangle)t+\frac{(\Gamma-\langle\Gamma\rangle)^2}{2!}t^2-...\right]\mathrm{d}\Gamma \tag{2.29}$$

Working through the integrals, we will get

$$g_1(\mathbf{Q},t) = \exp(-\langle\Gamma\rangle t)(1+\frac{\mu_2}{2!}t^2-\frac{\mu_3}{3!}t^3+...) \tag{2.30}$$

where

$$\mu_2 = \int_0^\infty G(\Gamma)(\Gamma-\langle\Gamma\rangle)^2\,\mathrm{d}\Gamma \tag{2.31}$$

and

$$\mu_3 = \int_0^\infty G(\Gamma)(\Gamma-\langle\Gamma\rangle)^3\,\mathrm{d}\Gamma \tag{2.32}$$

The first cumulant $\bar{\Gamma}$ describes the average relaxation rate of the distribution. The second μ_2 correspond to the variance of the mean, and the third cumulant μ_3 provides a measure of asymmetry of the distribution [45]. The averaged translational diffusion coefficient $\langle D\rangle$ may be derived at a single angle or at a range of angles depending on the wave vector $\mathbf{Q}$.

$$\langle\Gamma\rangle = \langle D\rangle\cdot Q^2 \tag{2.33}$$

The averaged hydrodynamic radius can be obtained through Stoke-Einstein equation. The polydispersity of the system is described by the polydispersity index PDI $= \mu_2/\langle\Gamma\rangle^2$.

2.2 Brownian motion at a planar interface

The Brownian motion of particles, which are in close proximity to a planar wall, is slowed down as compared to the unbounded motion in bulk and it becomes anisotropic. Due to

hydrodynamic interaction with the wall, the particles experiences a drag force which increases with decreasing distance from the wall and which is different for the direction parallel to the wall and normal to the wall. First attempts to describe this effect for the motion perpendicular to the wall theoretically date back to the early twentieth century [46, 47], in which distance dependent correction factors for the viscous force $\mathbf{F}(z) = \lambda(z)\mathbf{F}_0$ were introduced, where $\mathbf{F}_0$ is the Stokes force in the bulk and z is the shortest distance between the wall and the particle center. The coordinate system is chosen such that the $x-$ and $y-$direction are parallel to the wall. The nowadays commonly accepted expression for the correction factor for the force normal to the wall was given by Brenner and coworkers [30, 31].

$$\begin{aligned}\lambda_\perp(z) &= \frac{4\sinh\alpha}{3}\sum_{n=1}^{\infty}\frac{n(n+1)}{(2n-1)(2n+3)} \\ &\times \left[\frac{2\sinh[(2n+1)\alpha]+(2n+1)\sinh[2\alpha]}{(2\sinh[(n+1/2)\alpha])^2-((2n+1)\sinh\alpha)^2}-1\right],\end{aligned} \tag{2.34}$$

where $\alpha = \cosh^{-1}(z/R)$. This expression holds strictly only for a single particle in the limiting case of low Reynolds numbers, i. e. friction forces dominate inertial forces, and stick boundary conditions. For large z the sum of eq. 2.34 may be truncated after the first term which yields

$$\lambda_\perp(z) = \left(1-\frac{9}{4}\exp(-\alpha)\right)^{-1} \tag{2.35}$$

if $\sinh\alpha \approx \exp(\alpha)/2$ is used. With the definition of α we may further use $\exp\{-\alpha\} \approx R/2z$ which yields an approximate expression for the correction factor

$$\lambda_\perp(z) = \left(1-\frac{9}{8}\frac{R}{z}\right)^{-1}. \tag{2.36}$$

This approximation coincides with the original expression by Lorentz [46] deviates by 20% from the exact expression at $z/R = 1.5$, 10% at $z/R = 2$, and by less than 1% at $z/R \geq 3$ [23].

For the correction factor applying to the motion parallel to the wall, $\lambda_\parallel(z)$, there is no analytical expression available. However, the approximate expression by Faxén [47]

$$\lambda_\parallel(z) = \left[1-\frac{9}{16}\frac{R}{z}+\frac{1}{8}\left(\frac{R}{z}\right)^3-\frac{45}{256}\left(\frac{R}{z}\right)^4-\frac{1}{16}\left(\frac{R}{z}\right)^5\right]^{-1}, \tag{2.37}$$

deviates from simulation results by less than 10% for $z/R > 1.04$ and is basically perfect for $z/R > 1.4$ [23]. As the condition of low Reynolds numbers applies to the Brownian motion

of colloidal particles, eqs. 2.37 and 2.34 can be used to calculate position dependent diffusion coefficients as $D_{\parallel\perp}(z) = D_0/\lambda_{\parallel\perp}(z)$.

2.3 Evanescent wave dynamic light scattering for near-wall Brownian motion

The Brownian dynamics of particles near a wall can be studied by evanescent wave dynamic light scattering (EWDLS). In this technique, a laser beam is reflected from the flat surface of a semi–spherical lens with refractive index n_1 which is in contact with the sample solution with refractive index n_2, as sketched in Fig. 2.1. If $n_2 < n_1$, total internal reflection occurs at angles of incidence which are smaller than the critical angle $\alpha_i < \alpha_c$ and on the solution side an evanescent wave is formed. The evanescent wave is propagating along the interface and

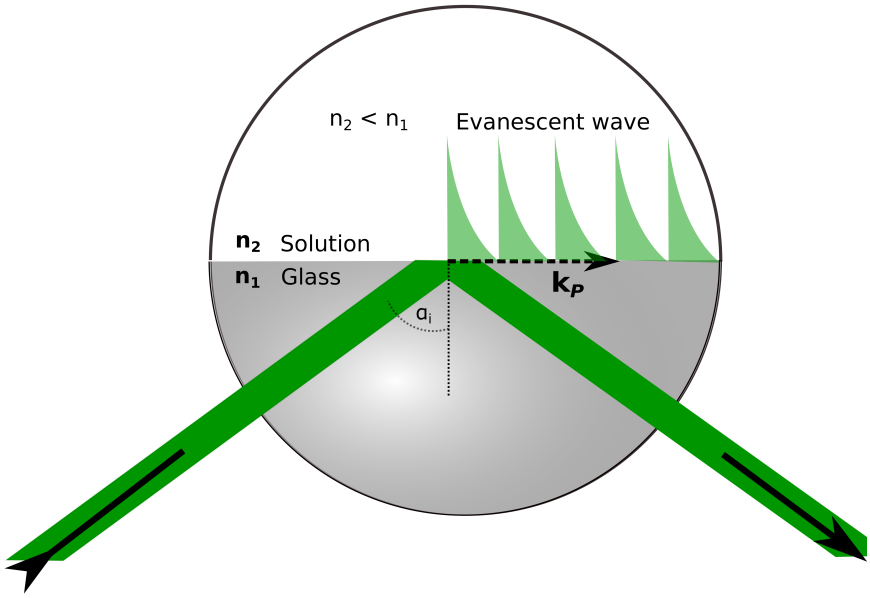

Figure 2.1: *Illustration of an evanescent wave. The lower part shows a semi-spherical lens with higher refractive index; the upper part shows a semi-spherical sample cell with particle solution inside. Note: This is an artistic drawing, which doesn't represent the real physical picture. Evanescent wave is only present at the very vicinity where the incident laser beam hits the interface.*

has a field strength which decays exponentially with distance from the interface as

$$\mathbf{E} = \mathbf{E}_0 \exp\{-\frac{\kappa}{2}z)\} \tag{2.38}$$

where the inverse decay length of the evanescent field is $\kappa/2 = 2\pi\sqrt{(n_1 \sin\alpha_i)^2 - n_2^2}/\lambda_0$. Using typical numbers and for wavelength ($\lambda_0 = 532$nm), refractive indexes ($n_1 = 1.73$; $n_2 = 1.33$) and angle of incidence ($\alpha_i = 65^\circ$) yields a penetration depth of the field $PD = 2/\kappa \approx 100$ nm. Thus, only particles which are in the ultimate vicinity to the interface, will significantly contribute to the signal, if an evanescent wave is used as the illumination source for a dynamic light scattering experiment.

There are two major differences between standard dynamic light scattering and evanescent-wave light scattering. First, as just described, the illumination profile in EWDLS is not homogeneous. Second, the hydrodynamic mobilities $\mu_{i,j}$ are influenced by the presence of wall. The hydrodynamic interaction between two particles close to wall is different from that in the bulk, as the shear waves generated by one particles are affected by the wall before reaching the other particles. Nonetheless, light which is scattered from particles located in the the evanescent wave can be correlated (like in conventional DLS) to study particle dynamics. With an evanescent illumination which is homogeneous in in the directions parallel to the interface at constant z, the field scattered by an ensemble of N identical particles at a given time t is,

$$\mathbf{E}_S \propto \sum_j^N \exp(-\frac{\kappa}{2}z_j)\exp(\imath\mathbf{Q}\cdot\mathbf{r}_j). \tag{2.39}$$

Different from Bulk DLS, here the scattering vector is $\mathbf{Q} = \mathbf{k}_S - \mathbf{k}_e$ where $\mathbf{k}_e$ is the wave vector of the evanescent wave and $\mathbf{r}_j$ is again pointing from an arbitrarily chosen origin to the position of the j^{th} particle.

As in conventional DLS, to extract dynamic information from an experiment is the time-auto correlation function of the scattered field, $g_1(t) = \langle E(0)E(t)\rangle$, has to be determined, where $E(0)$ and $E(t)$ are the scattered field strengths at times $t = 0$ and t, respectively . This field-correlation function is determined by the probability density function (PDF) $P(\mathbf{r}_0)$ of the particles' position coordinate at $t = 0$ and the conditional PDF $P(\mathbf{r},t \mid \mathbf{r}_0)$ of finding a particle at $\mathbf{r}$ at time t given a particle was at $\mathbf{r}_0$ at $t = 0$

$$g_1(t) = \int_{z>R} d\mathbf{r}_0 \int_{z>R} d\mathbf{r} P(\mathbf{r},t \mid \mathbf{r}_0)P(\mathbf{r}_0)\exp\{-\frac{\kappa}{2}(z_0+z)\}\exp\{\imath\mathbf{Q}\cdot(\mathbf{r}_0-\mathbf{r})\}. \tag{2.40}$$

Since the probability to find a particle at $z < R$ is zero, the integrations range from R to infinity. In a dilute bulk solution of particles without long ranging interactions $P(\mathbf{r},t \mid \mathbf{r}_0)$ is a solution of Fick's second law.

$$\frac{\partial P(\mathbf{r},t \mid \mathbf{r}_0)}{\partial t} = D_0 \nabla^2 P(\mathbf{r},t \mid \mathbf{r}_0), \tag{2.41}$$

where ∇^2 is the square of the gradient operator. With this differential equation, eq. 2.40 can be solved analytically and lead to the expression for the bulk correlation function of eq. 2.20 in the limiting case of $\kappa \to 0$.

In the vicinity of a wall the position dependence and the anisotropy of the particle mobility has to be taken into account, thus the Smoluchowski equation of motion becomes

$$\frac{\partial P(\mathbf{r},t \mid \mathbf{r}_0)}{\partial t} = \frac{\partial}{\partial z}\left(D_\perp(z) \frac{P(\mathbf{r},t \mid \mathbf{r}_0)}{\partial z} \right) + D_\parallel(z) \left(\frac{\partial^2}{\partial x^2} + \frac{\partial^2}{\partial y^2} \right) P(\mathbf{r},t \mid \mathbf{r}_0). \tag{2.42}$$

So far there is no analytical solution available for this equation. An expression for the short time limit of the field correlation function

$$g_1(t) = \exp\{-\Gamma t + \mathscr{O}(t^2)\}\,, \tag{2.43}$$

has been provided by Holmqvist *et al.* [22, 23]. For dilute suspensions of particles which interact among themselves and with the wall only by hard core repulsion, the initial relaxation rate of the field correlation function is given by,

$$\Gamma = Q_\parallel^2 \langle D_\parallel \rangle(\kappa) + \left(Q_\perp^2 + \frac{\kappa^2}{4} \right) \langle D_\perp \rangle(\kappa)\,, \tag{2.44}$$

where the pointed brackets represent the average of the position dependent diffusion coefficients over the penetration depth of the evanescent wave,

$$\langle D_{\parallel,\perp} \rangle(\kappa) = D_0 \kappa \int_R^\infty dz \exp\{-\kappa(z-R)\} / \lambda_{\parallel,\perp}(z). \tag{2.45}$$

This expression for the short time decay rate allows for the determination of $\langle D_\parallel \rangle$ and $\langle D_\perp \rangle$ independently of each other, if in an experiment $Q_\perp$ and $Q_\parallel$ can be varied independently.

2.3.1 Spheres interacting with a wall

In deriving eq. 2.44 long ranging interactions between particles and between particles and the wall were disregarded and consequently the probability density function $P(\mathbf{r})$ was treated as a constant. In a situation where particles interact with the wall and the concentration is

small enough to neglect the inter-particle interactions, the PDF may still be considered to independent of the $x-$ and $y-$coordinate at constant z. In the direction normal to the wall $P(\mathbf{r})$ is equal to the Boltzmann–factor of the interaction potential between the particle and the wall $V(z)$, i. e.

$$P(\mathbf{r}) = \exp\{-\beta V(z)\} \tag{2.46}$$

where $\beta = 1/k_B T$ with k_B Boltzmann's constant and T the absolute temperature. For this problem, the Smoluchowski equation of motion takes the form

$$\begin{aligned} \frac{\partial P(\mathbf{r},t \mid \mathbf{r}_0)}{\partial t} &= \frac{\partial}{\partial z}\left(D_\perp(z)\left\{\frac{\partial}{\partial z}P(\mathbf{r},t \mid \mathbf{r}_0) + \beta P(\mathbf{r},t \mid \mathbf{r}_0)\frac{d}{dz}V(z)\right\}\right) \\ &+ D_\parallel(z)\left(\frac{\partial^2}{\partial x^2} + \partial y^2\right)P(\mathbf{r},t \mid \mathbf{r}_0) \end{aligned} \tag{2.47}$$

Based on this differential equation, Holmqvist *et al.* devised a short time a expansion for the initial decay rate of the field correlation function, which has the same form as eq.2.44. However, the averaged diffusion coefficients are given by

$$\langle D_{\parallel,\perp}\rangle(\kappa) = D_0 \frac{\int_R^\infty dz \exp\{-\beta V(z)\}\exp\{-\kappa(z)\}/\lambda_{\parallel,\perp}(z)}{\int_R^\infty dz \exp\{-\beta V(z)\}\exp\{-\kappa(z)\}} \tag{2.48}$$

3 Method - EWDLS

3.1 EWDLS instrumentation

The EWDLS set up is a home-built instrument based on a triple axis diffractometer by Huber Diffraktionstechnik, Rimsting, Germany, as shown in Fig 3.1. The setup is equipped with a frequency doubled Nd/Yag Laser (Excelsior; Spectra Physics) with a vacuum wavelength of $\lambda_0 = 532$ nm and a nominal power output of 300 mW as a light source. Scattered light is collected with an optical enhancer system by ALV Lasververtriebsgesellschaft, Langen, Germany, which is connected to two avalanche photo diodes by Perkin Elmer via an ALV fiber splitter. The TTL signals of the diode were cross-correlated using an ALV-6000 multiple tau correlator. The scattering geometry and the definition of the scattering vector and its component parallel and normal to the interface are sketched in Fig. 3.2. The sample cell (custom-made by Hellma GmbH, Muellheim, Germany) consists of a hemispherical lens as the bottom part, made of SF10 glass, with an index of refraction $n_1 = 1.736$ at $\lambda_0 = 532$ nm. The particle suspension is contained in a hemispherical dome sitting on top of the lens. The primary beam is reflected off the interface between the glass and the solution, which is considered to be a flat wall, by that creating an evanescent wave in the the solution which is used as the illumination for the scattering experiment. The evanescent wave has a wave vector $\mathbf{k}_e$ pointing in the direction of the reflected beam's projection onto the reflecting interface. The scattering vector is given by $\mathbf{Q} = \mathbf{k}_s - \mathbf{k}_e$, where the scattered light wave vector, $\mathbf{k}_s$, is defined by the two angles θ and α_r which describe the position of the detecting unit.
The inverse penetration depth of the evanescent wave depends on the angle of incidence α_i as $\kappa/2 = 2\pi\sqrt{(n_1 \sin\alpha_i)^2 - n_2^2}/\lambda_0$. The magnitudes of the scattering vector components parallel $Q_{\parallel} = 2\pi n_2 \sqrt{1 + \cos^2\alpha_r - 2\cos\theta\cos\alpha_r}/\lambda_0$ and normal $Q_{\perp} = 2\pi n_2 \sin\alpha_r/\lambda_0$ to the interface can be varied by changing θ and α_r. In a typical EWDLS experiment, series of correlation

functions are recorded at fixed $Q_\perp$ varying $Q_\parallel$ ($Q_\parallel$-scan) or vice versa ($Q_\perp$-scan).

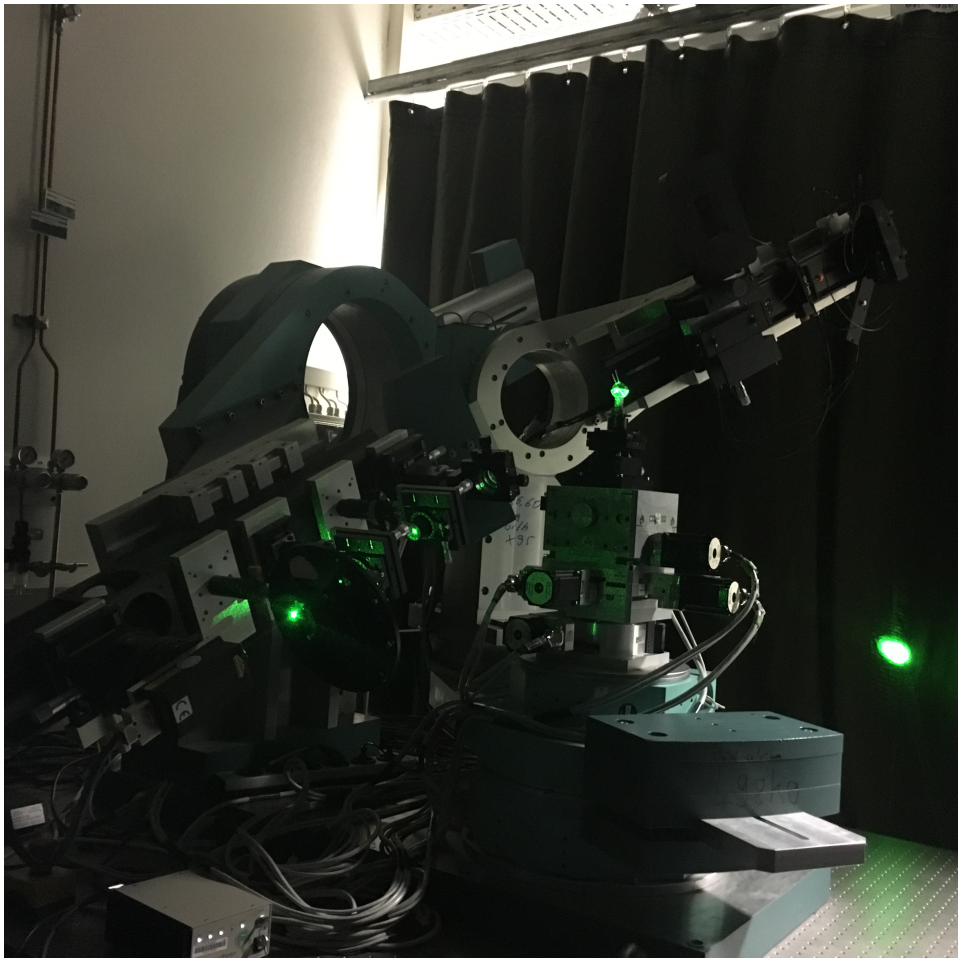

Figure 3.1: *Photo of EWDLS instrument.*

3.2 Instrument alignment

The basic mechanical element of the EWDLS-instrument are sketched in Fig. 3.3 together with a definition of the coordinate system and all degrees of freedom, which are available to align the instrument. The sample cell is mounted on a tower consisting of a lift table to move the sample vertically (z-direction), two horizontal linear stages for the motion in x- and y-direction and two circle segment cradles which rotating the sample cell around the x-axis (χ_1) and the y-axis (χ_2) and tilting. The sample tower sits a goniometer, which allows to rotate is around the z-axis by the angle ω. The sample laser is mounted on a goniometer arm which rotates around

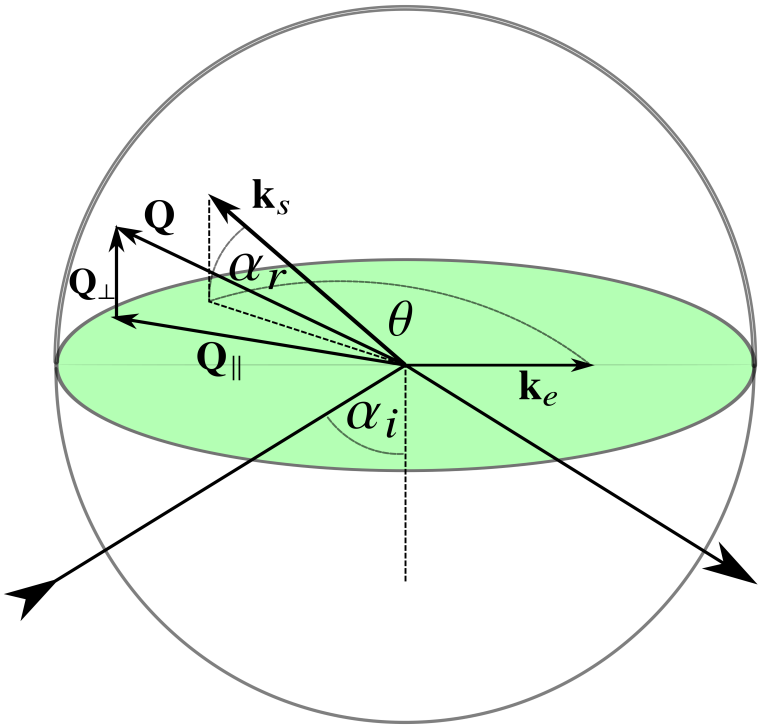

Figure 3.2: *Scattering geometry in EWDLS setup with spherical geometry.*

the x-axis by the angle α_i (laser arm) and the detecting unit is fitted to two goniometers which rotate around the z-axis by the angle θ and around the x-axis by the angle α_r (detector arm). The axis of the ω- and thew θ-goniometer are identical and intersect with the axes of the α_i- and α_r-goniometers (which are again identical) at the origin of the coordinate system, which is also the pivot point of the circle segment cradles. All the linear stages cradles and goniometers can be moved by software driven stepper motors equipped with gear boxes, which allow for a repeatability $< 0.001^\circ$ for all circular motions, $< 10\mu$m for the x- and y stages and $< 1\mu$ for the vertical lift table. Furthermore, all the laser, the optical enhancer system (OES) and all optical elements are mounted on X-95 rails (Linos) and adjustment stages (labeled (a) in Fig. 3.3)which allow for linear displacement in the x- and z-direction, as well as tilts around theses axes. These stages are manually driven with a typical repeatability of 5μm.
To conduct a reliable measurement, the instrument needs to be adjusted such that:

(1). The primary beam is parallel to the y-coordinate and hits the origin of the system;

(2). The center of sample cell coincides with the intersection point of goniometer axes;

(3). The reflecting interface needs to be normal to the plane which is defined by primary and reflected beam.

While the basic alignment of the primary beam (point (1)) has to be done only very rarely, for example when the laser is replaced to allow for a different illumination wave length, the alignment of the sample cell (points (2) and (3)) is required every time a new sample is introduced.

3.2.1 Primary beam and optical elements alignment

As the first step of the alignment procedure, all goniometers, stages and cradles are moved to their nominal zero–positions, which are defined by a machine internal opto-mechanical switches. The further procedure relies on the zero position of the goniometer of theα_i circle, which is carrying the laser. Note that this nominal zero-position, corresponds to $\alpha = 90^\circ$ in the experiment, for the purpose of describing the alignment procedure we will call this position $\alpha_i = 0$. All other positions will be defined with respect to this one.
In the next step the primary beam has to be directed parallel to the X-95 rail which caries the laser. For this purpose all optical elements, the OES, the splitter and the diodes have to be removed and a 100μm pinhole which can be slid up and down the rail is mounted. First the pinhole is fixed close to the laser, which is then adjusted in the x- and z- directions (using the linear stages of the positioning unit (a) indicated in Fig. 3.3), such that the beam passes

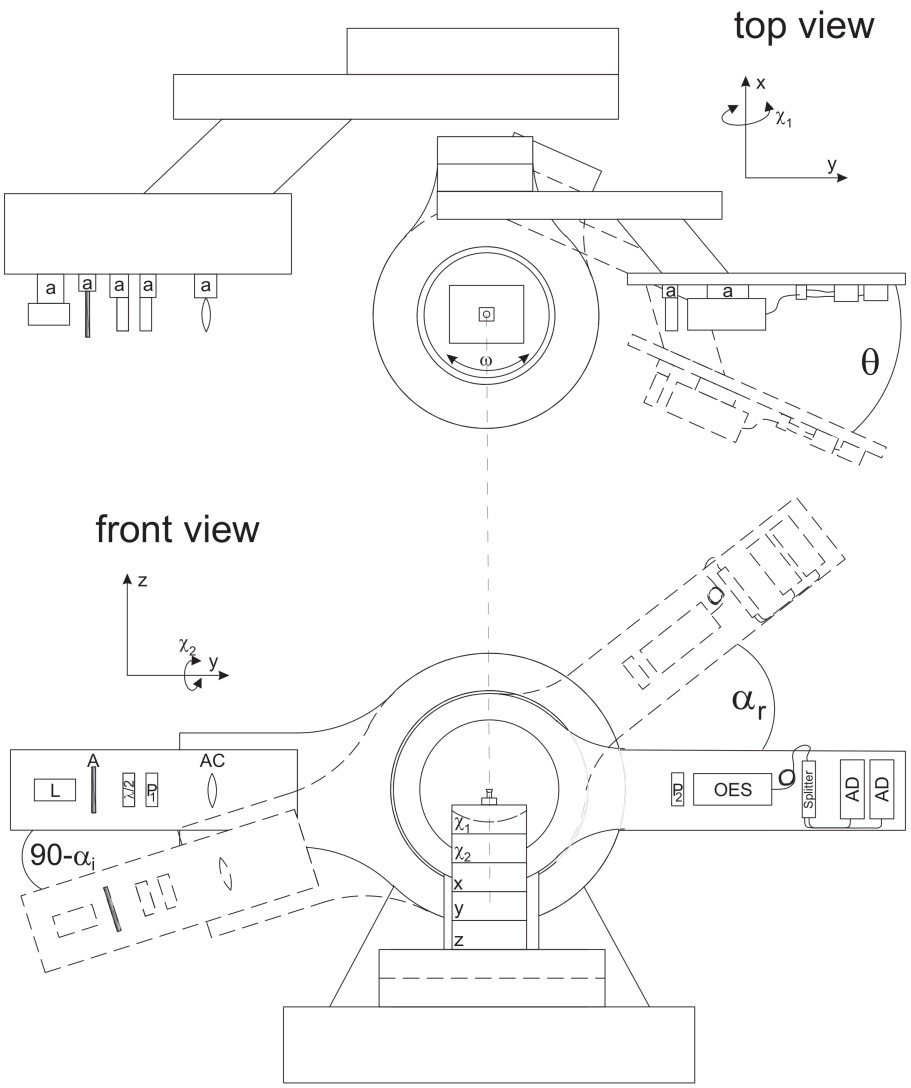

Figure 3.3: *Sketch of the scattering geometry in EWDLS setup. The labels in in the sketch identify the laser (L), a grey density filter wheel (A), a $\lambda/2$-plate, polarizers (P_i), the optical enhancement system (OES), a fiber splitter, the avalanche diodes (AD) and various positioning units(a)*

through the pinhole. Then the pinhole is moved as far as possible in the beam down direction and the laser is now adjusted by tilting it around the x- and z-axes for maximum transmission. This procedure of aligning the laser position and tilt is repeated until the diffraction pattern of the pinhole, which can be observed on an approximately three meters distant wall, is symmetric, and does not change upon moving the pinhole along the rail.

A similar procedure is now applied to define the zero-position of the α_r-circle. For this purpose the pinhole is mounted on the rail which is usually carrying the detection unit. When the pinhole is fixed close to the sample stage, its position in the x- and z-directions is adjusted such that the laser beam passes, while maximum transmission is achieve by adjusting α_r and θ when the pinhole is positioned far from the sample stage. Again this two step procedure is repeated until the diffraction pattern is symmetric, and does not change upon moving the pinhole along the rail.

By this procedure, so far it is assured that the laser beam is parallel to the instruments nominal$y$-direction, which does not necessarily mean that it comes to lie in x- and z-axes. This has to be achieved in the next steps, which basically requires a controlled shift of the laser beam position along the x-axis to hit the z-axis and vice versa. To meet the first requirement, the pinhole is positioned at the far end of the detector arm, which is then moved to $\theta = 180^\circ$ keeping $\alpha_r = 0^\circ$ and then the laser is moved to $\alpha_i = -180^\circ$. If the laser beam was not already hitting the z-axis it will now not pass through the pinhole. Now the laser and the pinhole are moved towards each other along the x-direction iteratively by the same distance increments until the laser beam hits the pinhole again. Subsequently the α_i- and θ-circle are moved back to their nominal zero positions. In general the beam will not pass through the pinhole perfectly. Therefore the optimum value of θ has to be searched where the beam transmitting the pinhole produces a symmetric diffraction pattern. This new position is now assigned to $\theta = 0^\circ$ in the software, driving the stepper motors. The described procedure should be repeated at least once more be repeated to improve accuracy.

To finally adjust the beam in the z-direction, with the aim to hit the x-axis, the laser is again moved to $\alpha_i = -180^\circ$, but this time the detector are is moved to $\alpha_r = 180^\circ$ keeping $\theta = 0^\circ$. In this situation the laser and the pinhole have to be moved towards each other along the z-direction iteratively by the same distance increments until the laser beam passes through the pinhole. After moving back the α_i- and α_r-circle to their nominal zero positions the optimum value of α_r has to be searched at which the beam passes through the pinhole creating a symmetric diffraction pattern. Also theses these steps have to be repeated at least once more to improve the quality of the alignment.

Now the laser beam is in its final position and the optical elements have to be mounted in their

beam down succession, starting with the attenuator. Each individual element is aligned by iteratively adjusting their position and tilt such that the transmitted beam is passing through the pinhole at the far end of the detector arm producing a symmetric diffraction pattern and that the reflected beam is directed into the front aperture of the laser. At this stage it is important to keep the back reflected beam slightly off the center of the aperture, because a perfect alignment would couple the reflected beam into the laser cavity, which will cause instabilities of the power output. At this stage, the polarization direction is only coarsely aligned, by manually adjusting the transmission direction of the $\lambda/2$-plate and the two polarizers parallel to the x-axis.

In the next step, the OES has to be adjusted. For this purpose the primary laser beam is attenuated by a factor 4×10^4 such that it is barely visible. Then the pinhole is removed and the OES is mounted on the detector arm, with its front aperture between 16 and 18 cm away from the sample position. The OES is coarsely aligned with linear translation stages along the x- and the z direction such that the laser beam passes centrally through the its front aperture, which has a diameter of about 2 mm. The the attenuator is set to its minimum transmission of 5×10^{-9} and the OES is connected to the avalanche diodes. Using the built in linear portioners for the OES pinhole and lens alternatingly with the tilt adjustment screws of the OES fiber coupler the system is aligned for maximum transmission. A count rate of the avalanche diodes $> 1.2 \times 10^7 \mathrm{s}^{-1}$ should be achieved at the nominal laser power output of 300mW and an attenuator transmission of 5×10^{-9}.

As the last step of the basic alignment the polarization direction of the primary beam has to be adjusted parallel to the reflecting plane of the sample cell. This can be achieved only if the sample cell was adjusted beforehand, as will be described in the next section. Once the sample cell is aligned, the the angle of incidence is set to the Brewster angle, at which only light is reflected that is polarized normal to the plane of incidence. In the present case this identical with the light which is polarized parallel to the reflecting surface, as this surface was aligned to be normal to the plane of incidence. For the refractive index of the semi-spherical lens, $n_1 = 1.736$ at $\lambda_0 = 532$nm the Brewster angle is $\alpha_B = 60.056^\circ$, which corresponds to $\alpha_i = -29.944^\circ$ in the notation we use for the description of the alignment procedure. Now the detector arm is moved $\alpha_r = 29.944^\circ$ and the polarizer on the detector arm P_2 is adjusted for minimum transmission. Hereafter the polarizer on the laser arm P_1 is turned in small steps to increase the detected intensity to a local maximum. This procedure is repeated until turning P_1 will not anymore cause an increase of the transmitted intensity. In this situation the transmission direction of P_1 is parallel and that of P_2 in normal to the reflecting surface. Therefore P_2 is turned by 90° and finally the $\lambda/2$-plate is turned to achieve maximum detected

intensity.
It is important to note that changing the the scattering angles θ and α_r will inevitably change the polarization direction of P_2 with respect to that of P_1, which with the current setup has to be corrected manually. Therefore, P_2 is removed from the instrument after alignment for experiments on samples which are not birefringent. Only for the measurement of orientational dynamics of optically anisotropic particles [38, 48], P_2 is kept in place.

3.2.2 Sample cell alignment

The sample cell has to be aligned such that its center coincides with the instruments origin and that the reflecting interface is lying in t the *xy*-plane, i.e. it has to be normal to the plane which is defined by primary and reflected beam. For this purpose the semi-spherical lens, is glued with the flat side on top to a post which is mounted onto the circle segment cradle on top of the sample tower, the detector arm is moved to a shallow angle in the range between $-10^\circ > \alpha_i > -15^\circ$ such that the laser beam is reflected off the plain side of the semi-spherical lens. The detecting unit is moved out of the direction of the reflected beam, which can thus hit a target at the opposite wall of the room, which is about 3.5 meters away from the sample cell position. The point where the beam hits the target is marked, before the sample tower is turned to $\omega = 180^\circ$. In general the beam will hit the target now at a different height.Therefore, the tilt of the top cradle, χ_1, is changed until the beam's point of incidence is back at its original height, to determine the displacement $\Delta\chi_1$. Subsequently the cradle is moved to $\chi_1 = \Delta\chi_1/2$ and this position is defined as the new zero position of the top cradle in the software, driving the stepper motors. Hereafter the sample tower is rotated to $\omega = 270^\circ$ and again the incident point is marked on the target, before the sample stage is turned to $\omega = 90^\circ$. Now the bottom cradle is is used to return the incident point to its original height and the he new zero position of the bottom cradle is assigned to $\Delta\chi_2/2$ which is determined in analogy to the $\Delta\chi_1/2$. This procedure of turning the sample tower and tilting the cradles is repeated until the displacement of the incidence point upon a full rotation is smaller than the reading off accuracy, which is approximately 1mm. If this is achieved, the reflecting interface is parallel to the *xy*-plane within an accuracy $< 0.02^\circ$, but not yet necessarily at the correct position.
To adjust the position in the *z*-direction, the laser ant the detector arm are brought back to their zero-position, the front aperture of the OES is blocked and a pinhole is mounted between sample position and OES, which is adjusted such that the beam passes it centrally. After that the laser- and the detector goniometer are moved to specular conditions, i. e. $\alpha_i = -\alpha_r$, where the absolute values of the angles in the range $15 < |\alpha| < 35$. Any deviation of the laser incidence

point from the pinhole center is now correcting by adjusting the z-stage of the sample tower.IN general, one iteration of this procedure yields sufficient accuracy. A slight improvement may be achieved by using different values of $|\alpha|$ and average the values of the displacements in the z-direction, which are necessary to make the reflected beam hit the pinhole centrally.
Finally the x- and y-position of the sample cell have to be adjusted, which is done by a procedure similar to that used to adjust the tilt of the cell. The laser arm is turned to $\alpha_i = 25^\circ$, and the position of the reflected beam on the target at the wall is marked. After turning the sample tower to $\omega = 180^\circ$ the position of the incidence point has to be brought back to its original height, by shifting the sample position along the x-direction with the top linear stage. The required replacement $\Delta x/2$ is defined as the new zero position of the x-stage. Similarly the y-position has to be adjusted by determining $\Delta y/2$from the incidence positions of the reflected beam at $\omega = 90^\circ$ and $\omega = 270^\circ$. Again repeating the procedure of turning the sample tower and shifting the sample by the linear stages will improve the accuracy of the alignment, which is by far not as good as for the tilt alignment. Due to refraction the becomes divergent upon passing through the semi spherical lens resulting in a read off accuracy of the incidence position in the range of $\pm$5mm only. Nevertheless, the center position of the center position of the sample cell can be made to coincide with the system's origin within less than $\sim 500\mu$m, which is good enough for dynamic EWDLS measurements, however, reliable static measurements would not be possible. To validate the alignment and to obtain a measure for the reproducibility the experimental data, test measurements with a standard sample performed and the results are compared to theoretical predictions, as it is described in detail in section 3.3.

3.3 Details of data analysis

The analysis of the scattered intensity time auto-correlation function $g_2(t)$ from EWDLS is much less straightforward than in conventional bulk dynamic light scattering (DLS), mainly for two reasons. The first major complication occurs from the fact that a simple quadratic relation between $g_2(t)$ and the correlation function of the scattered field $g_1(t)$ which is usually assumed in DLS does not apply in most cases in EWDLS. As described in the previous section, the incident laser beam is totally reflected from the glass/solution interface in EWDLS. As this interface is always corrugated, it acts as a static scatterer which in general contributes significantly to the observed signal. Therefore a mixed homodyne/heterodyne detection scheme has to be taken into account, and the generalized Siegert relation [42]

$$g_2(t) = 1 + 2C_1 g_1(t) + (C_2 g_1(t))^2 \tag{3.1}$$

for the conversion from $g_2(t)$ to $g_1(t)$ has to be applied. Here, $C_2 = 1 - \sqrt{1-A}$ and $C_1 = C_2 - C_2^2$, with A the experimental intercept of $g_2(t)$. Fig.3.1 shows an example of field correlation function $g_1(t)$ and intensity correlation function $g_2(t)$. Further, in many cases

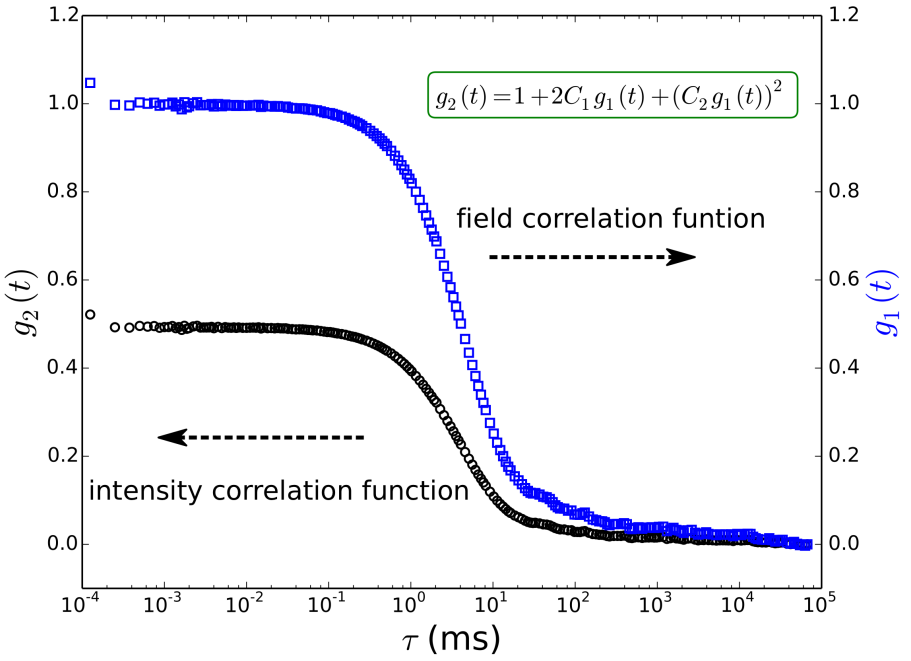

Figure 3.4: *An example of field correlation function $g_1(t)$ and intensity correlation function $g_2(t)$.$g_2(t)$ was measured on a diluted suspension of hard sphere system ASM470 and $g_1(t)$ was calculated from $g_2(t)$ through a generalized Sigert relation.*

EWDLS intensity-auto correlation functions exhibit a very slow decay at large times. The physical origin of this slow relaxation is not clear yet. While Garnier *et al.* conjecture that it is due to a slow reversible adsorption of the particles to the wall due to van der Waals attraction [19], Lisicki *et al.* [49] argue that it is also caused by the unavoidable stray-light from surface defects, which is scattered by colloids in the bulk of the suspension into the detector. Since these slow modes are in general well separated from the relaxation rates of interest, we approximate their contribution by an additional baseline B_1 to $g_1(t)$.
Thus, to determine the initial slope Γ of $g_1(t)$, which is related to the dynamic properties of interest, we chose to non–linear least squares fit the experimental correlation functions to Eq. (3.1), where $g_1(t)$ is modeled as a decaying single exponential function in time.

$$g_1(t) = (1 - B_1)\exp\{-\Gamma t\} + B_1. \tag{3.2}$$

According to Eqs. (3.1) and (3.2), B_1 is related to B_2, the baseline of $g_2(t)$, by $B_1 = \sqrt{(C_1/C_2^2)^2 + B_2/C_2^2} - C_1/C_2^2$. Consequently there are three fit parameters A, Γ and B_2. Since an erroneous baseline value will lead to a deviation of Γ from its true value, due to a normalization error, we fitted $g_2(t)$ repeatedly, starting with a number of data points, N_p. After a single fit had converged, two data points at the long time end of $g_2(t)$ were removed, reducing N_p by two, and the remaining data points were fitted again. This procedure was repeated until $N_p < 20$. With this technique it is possible to identify a limited range of N_p's where the values of B_2 and Γ are essentially independent of N_p. The Γ–values determined in this range are considered to be the initial slope or the first cumulant of $g_1(t)$. Fig 3.5 shows an example of the fitting procedure: as the number of fitted data points N approaches 80, we start to observe a plateau for Γ independent of N; the average Γ value, $\approx 0.1174 ms^{-1}$ within this range is determined to be the first cumulant of $g_1(t)$. Fig 3.6 presents the experimental intensity correlation function and the fitted curve based on the above-mentioned fitting routine.

In a typical $Q_{\|}$ scan, θ is varied from -30°to -130°in a angular resolution of 5°, while α_r is

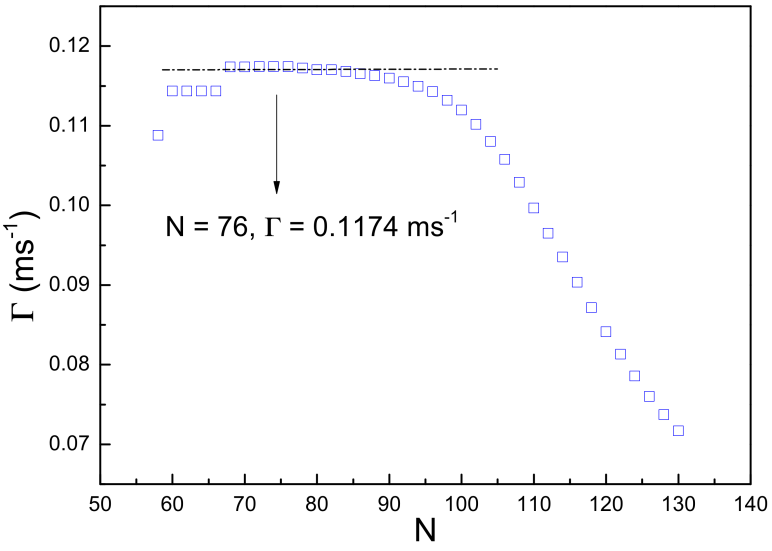

Figure 3.5: Γ *value versus number of data points fitted (N) in a typical fitting routine.*

kept constant; in this way, the value of $Q_{\|}$ can be changed, independent of the value of $Q_{\perp}$; Γ values are obtained at each $Q_{\|}$. In a typical $Q_{\perp}$ scan, a set of $\alpha_r - \theta$ values is numerically generated first; during the scan, α_r and θ are simultaneously varied according to the set, to keep the value of $Q_{\|}$ constant; the value of $Q_{\perp}$ depends on α_r; Γ is obtained at each $Q_{\perp}$ value.

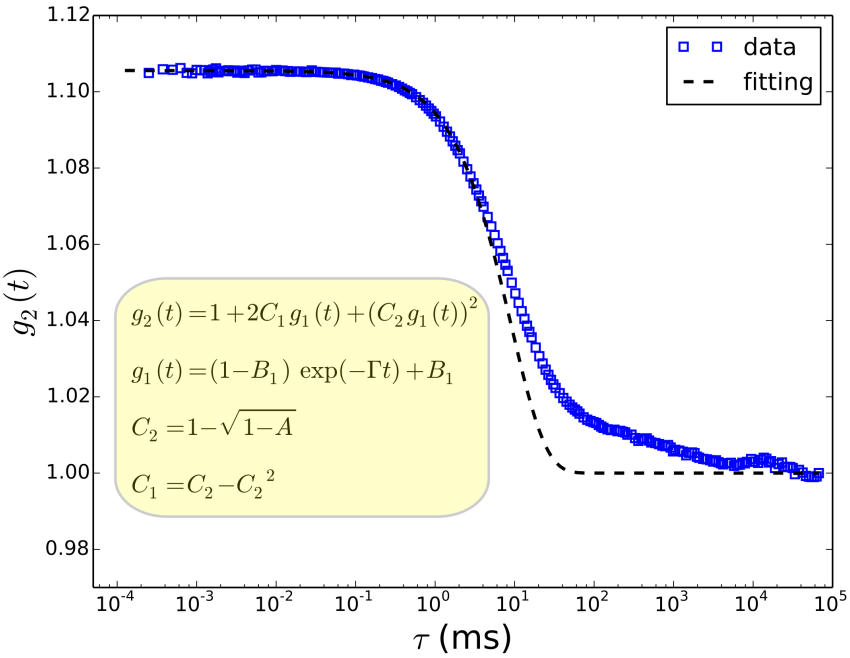

Figure 3.6: *Intensity correlation function measured on a diluted suspension of latex particles. Blue symbol represents the experimental data while the line represents the fitting. Equations used for fitting is shown in the box.*

To estimate the error, three repetitive measurements are conducted for each experimental setting. Standard deviation of Γ at each scattering vector is calculated from the repetitive measurements, and error is subsequently determined. Fig 3.7 and Fig 3.8 show the repetitive measurements conducted on a well defined colloidal system: Polystyrene particles (from Thermo Fischer) at ϕ=0.1%, in a density matched D_2O/H_2O solvent mixture to prevent sedimentation, with addition of 10 mM NaCl to sufficiently screen out the charges. We can consider the sample as homogeneous hard spheres in infinite dilution, and the error obtained from these measurements will represent the error of machine and alignment, rather than that of sample. $Q_{\parallel}$ scans, as shown in Fig 3.7, have an excellent reproducibility, while the data from $Q_{\perp}$, shown in Fig 3.8 are more scattered. In general, the EWDLS instrumentation and alignment routine have led to reliable and reproducible measurements of near-wall dynamics. In the following chapters, a dimensionless graphic representation of Γ versus Q^2 is more often used, where $\Gamma d^2/D_0$ replaces Γ for the y-axis and Q^2d^2 replaces Q^2 for the x-axis. This representation helps to make data from particles of different sizes comparable, and facilitates the comparison between experimental data and theoretical prediction. The latter point is illustrated in Fig 3.9. Experimental data, as represented by open symbols, fit very well into the hard sphere prediction, as shown by the dashed line. It needs to be pointed out that, although $Q_{\perp}$ data are more scattered, they can be well described by the prediction. This further confirms the reliability of the EWDLS method.

3.4 Effect of back reflection

An additional difficulty in EWDLS occurs from the fact that, different from bulk DLS, so far it was not possible to apply a refractive index matching batch around the sample cell. Therefore the the primary beam will be back reflected at exit from the semi-spherical lens with a reflectance, R. In the present case the semi-spherical lens has a refractive index of $n_1 = 1.736$, which leads to a reflectance of $R = 0.072$ according to Fresnell's equations. The back reflected beam will also be reflected off the glass sample interface, thereby causing a second evanescent wave with wave vector $\mathbf{k}_R = -\mathbf{k}_P$ where $\mathbf{k}_P$ is the wave vector of the evanescent wave caused by the original primary beam. In what follows the subscript $_P$ will refer to the evanescent wave caused by the primary beam, while $_R$ is associated with the evanescent wave due to the back reflected beam. The latter gives rise to a second scattering process, for which the in plane scattering angle $\theta_R = 180 - \theta_P$. Consequently the scattering vector components parallel to the

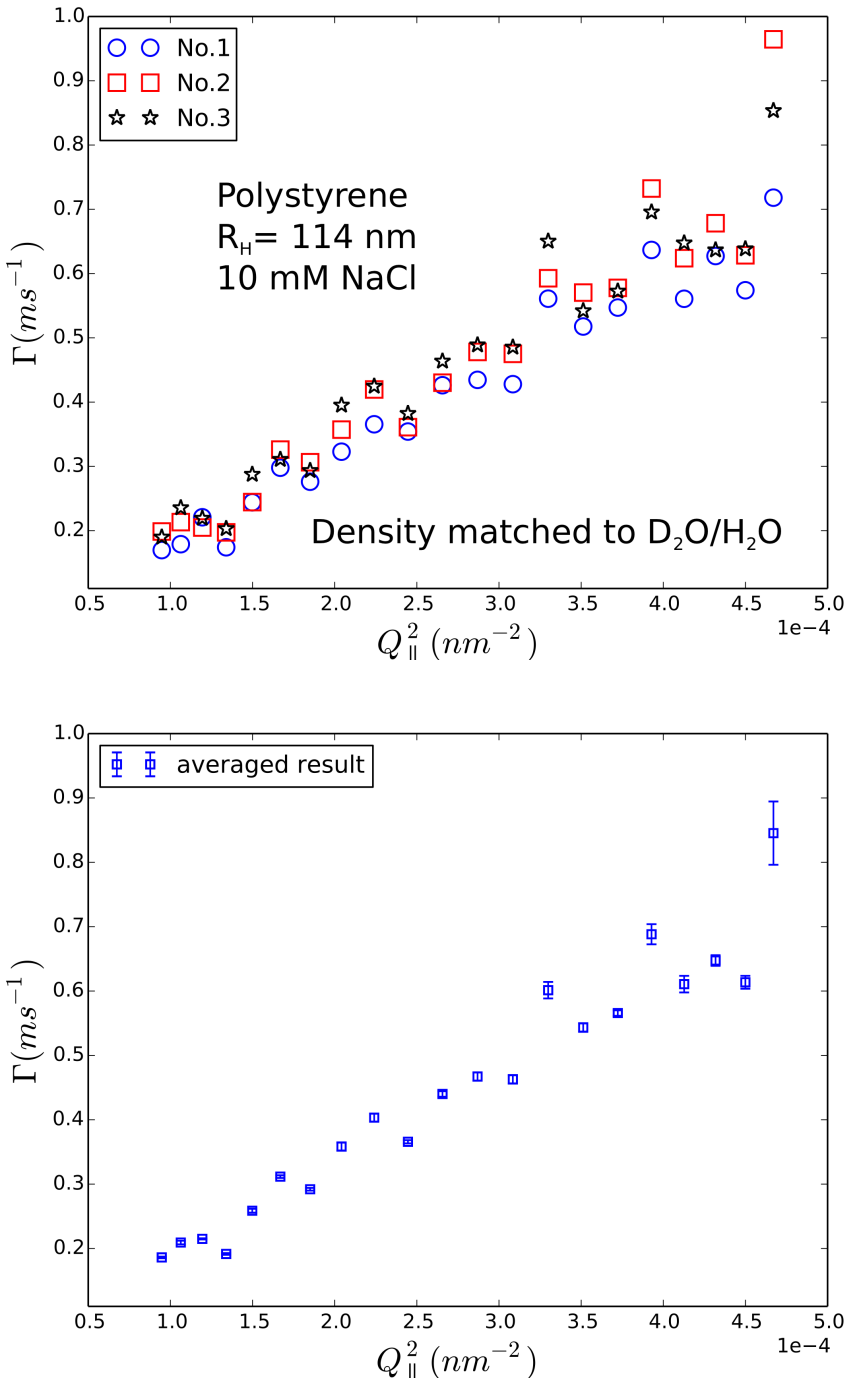

Figure 3.7: *Experimental results of relaxation rates* Γ *versus parallel component of scattering vector* $Q_{\|}$ *for Polystyrene suspension at low volume fraction. Top graph: three repetitive measurements; Bottom graph: averaged result with error bars.*

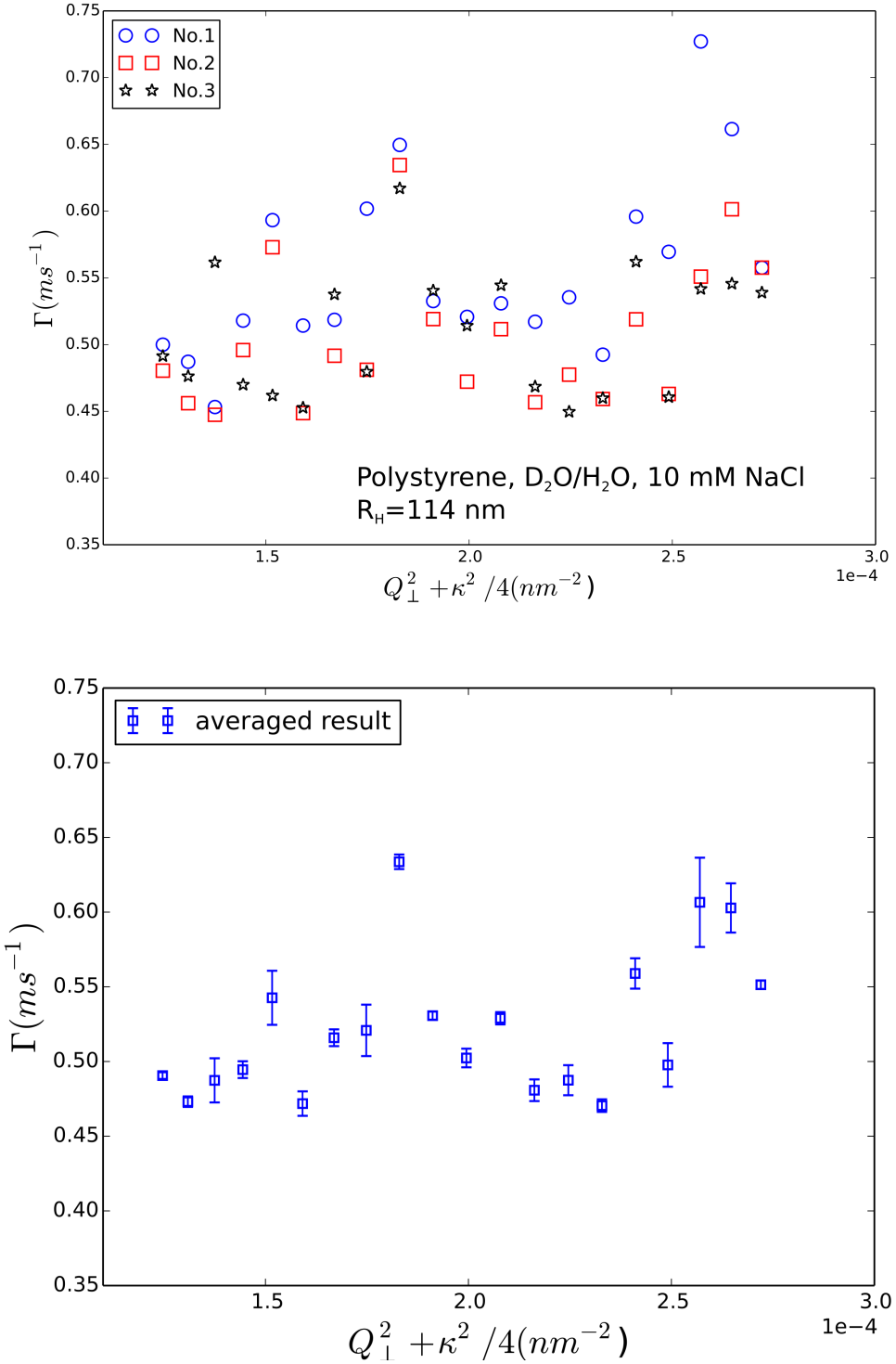

Figure 3.8: *Experimental results of relaxation rates Γ versus perpendicular component of scattering vector $Q_\perp$ for Polystyrene suspension at low volume fraction. Top graph: three repetitive measurements; Bottom graph: averaged result with error bars.*

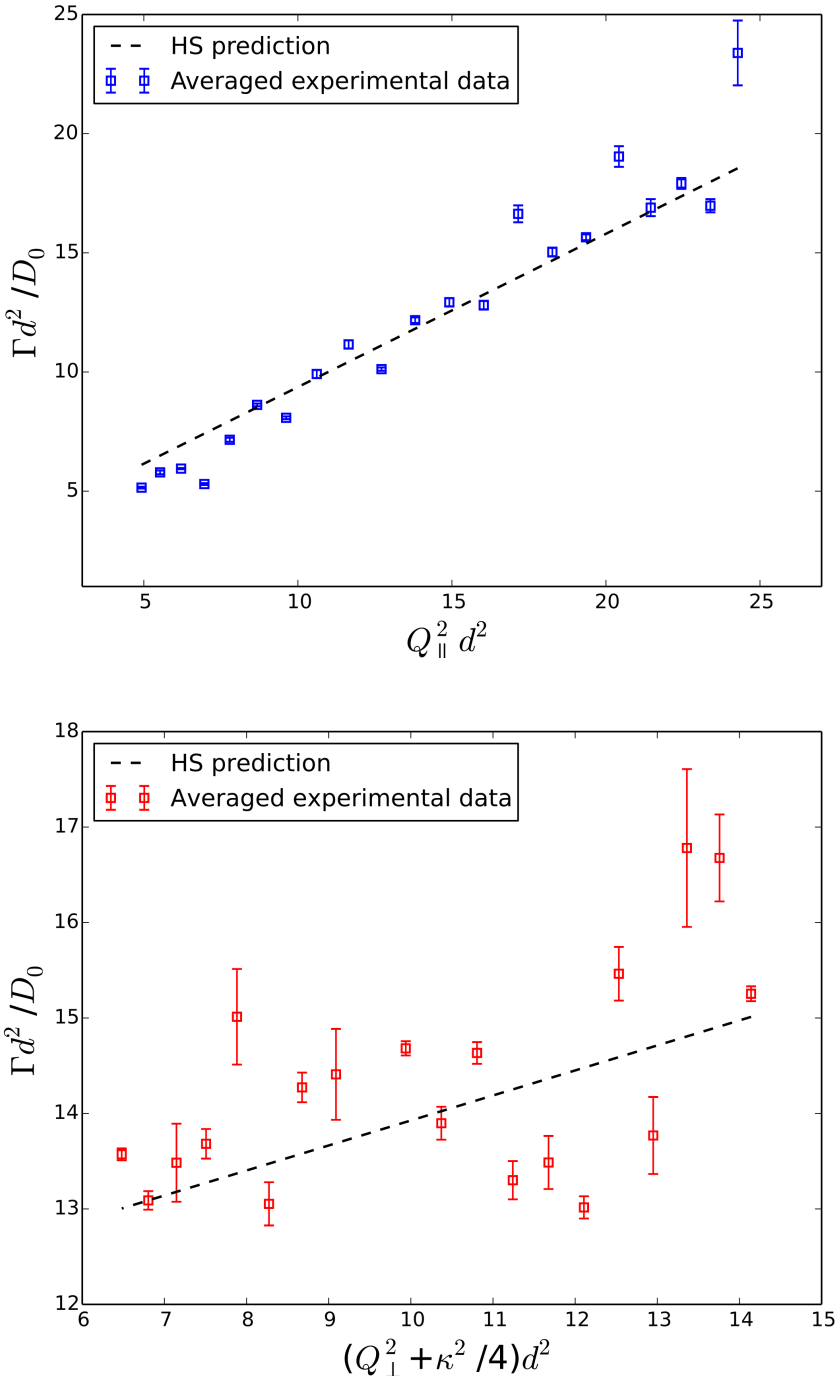

Figure 3.9: *Normalized relaxation rate Γ versus scattering vector squared for Polystyrene suspension at low volume fraction. Symbols represent the averaged result over three repetitive measurement. Line shows the hard sphere prediction. Top graph: Q-parallel scan; Bottom graph: Q-normal scan.*

interface are given by

$$Q_{\parallel,i} = \frac{2\pi}{\lambda_0} n \sqrt{1 + \cos^2 \alpha_r - 2\cos\alpha_r \cos\theta_i} \tag{3.3}$$

where $i \in \{R,P\}$, λ_0 is the laser vacuum wavelength, n the sample refractive index and α_r is the observation angle with respect to the interface. Differently, for the component normal to the interface

$$Q_{\perp,R} = Q_{\perp,P} \doteq Q_\perp = \frac{2\pi}{\lambda_0} n \sin\alpha_r \tag{3.4}$$

The normalized field correlation functions, in such a situation should now be considered as a weighted sum of two individual correlation functions from two scattering experiments

$$\widehat{g}_1(t) = \frac{P(Q_P) g_1^P(t) + RP(Q_R) g_1^R(t)}{P(Q_P) + RP(Q_R)} \tag{3.5}$$

where $Q_P = \sqrt{Q_{\parallel,P}^2 + Q_\perp^2}$, $Q_R = \sqrt{Q_{\parallel,R}^2 + Q_\perp^2}$ and $P(Q_i)$ is the particle scattering factor of a sphere.

In the evanescent illumination, the scattering factor is affected by the non-uniform character of the electric field and becomes penetration depth dependent. For a uniform particle, the scattering amplitude in the evanescent field reads $B(\mathbf{Q},\kappa) = \frac{1}{V}\int_V \exp\left[(i\mathbf{q} + \frac{\kappa}{2}\hat{\mathbf{e}}_z)\cdot\mathbf{r}\right] \mathrm{d}\mathbf{r}$. Thanks to the high symmetry, for a spherical particle of radius a, $B(\mathbf{Q},\kappa)$ can be explicitly calculated as

$$B(\mathbf{Q},\kappa) = 3\left[\frac{ca\cosh(ca) - \sinh(ca)}{(ca)^3}\right], \tag{3.6}$$

with $c = \sqrt{-Q^2 - iQ_\perp\kappa + \frac{\kappa^2}{4}}$. The scattering strength is then found as $P(Q) = |B(\mathbf{Q},\kappa)|^2$.

Furthermore, the individual correlation functions have to be constructed as follows. The corresponding field correlation functions are given by

$$g_1^i(t) \approx \exp\left(-\Gamma_i t + \frac{1}{2}\Gamma_{2,i} t^2\right), \tag{3.7}$$

with the first cumulant Γ_i given in the dilute regime by Eq. (2.44), and the second cumulant can be calculated as

$$\Gamma_{2,i} = \gamma_i - \Gamma_i^2, \tag{3.8}$$

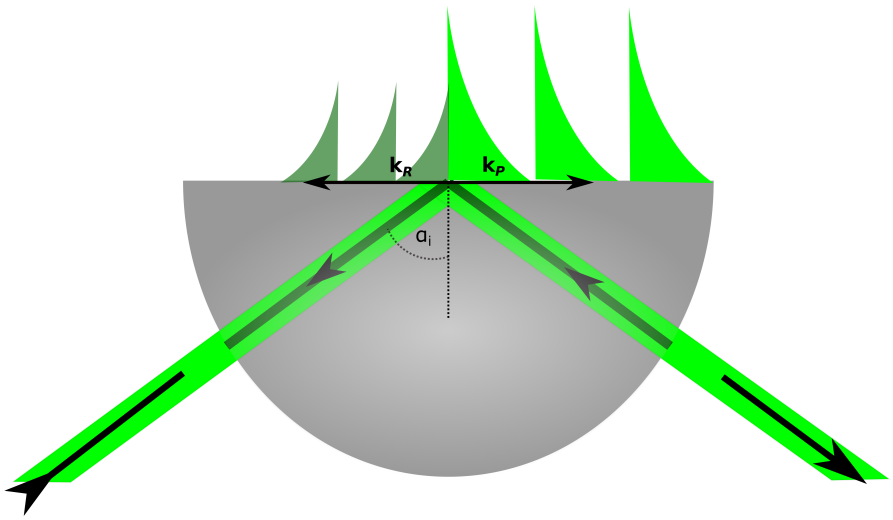

Figure 3.10: *For the illustration of the primary beam being back reflected at exit of the hemispherical lens to air, thereby creating a second evanescent wave.*

where the second moment γ_i is defined as [49]

$$\begin{aligned}\gamma_i &= Q_{\parallel,i}^4 \left\langle D_\parallel^2 \right\rangle_\kappa + \left(Q_\perp^4 - \frac{\kappa^4}{16} \right) \left\langle D_\perp^2 \right\rangle_\kappa \\ &+ 2Q_{\parallel,i}^2 \left(Q_\perp^2 - \frac{\kappa^2}{4} \right) \left\langle D_\parallel D_\perp \right\rangle_\kappa \\ &+ \kappa Q_{\parallel,i}^2 \left\langle D'_\perp D_\parallel \right\rangle_\kappa + \left(Q_\perp^2 + \frac{\kappa^2}{4} \right) \left\langle \left(D'_\perp\right)^2 \right\rangle_\kappa .\end{aligned} \tag{3.9}$$

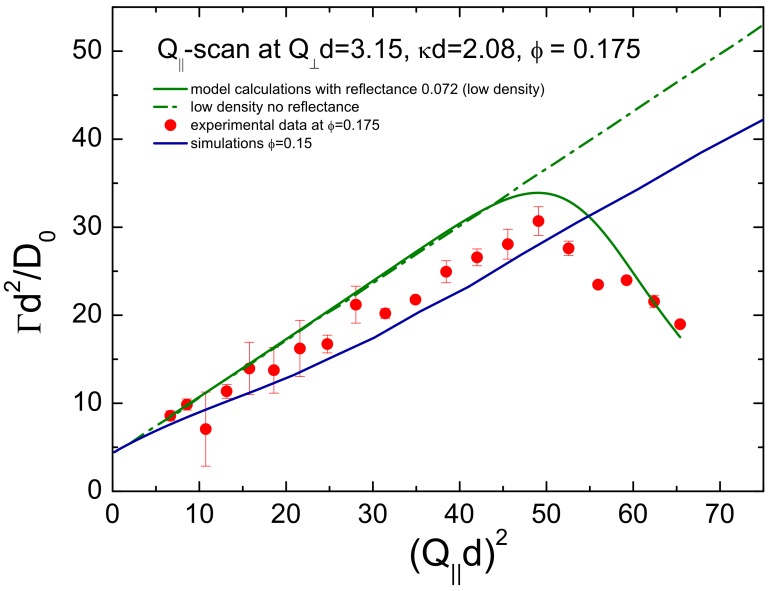

Figure 3.11: *Initial relaxation rates versus in-plan scattering angle θ. Comparison of the results from parameter free model calculations taking into account the effect of back reflection with experimental data obtained from a $Q_\parallel$-scan on a ASM470 ($R_H = 98$ nm) sample with a sphere volume fraction of $\phi = 0.04$ and with the low density predictions, where no back reflection is considered*

The experimentally measurable intensity correlation function has to be calculated from $\widehat{g}_1(t)$using the generalized Siegert relation, Eq. (3.1)

The averaged diffusion coefficients, which are required for the calculations of Γ and Γ_2 at a given value of κa were taken from Reference [49].

The calculated model functions are now evaluated by the same analysis procedure as the experimental data to obtain initial slopes Γ as a function of $Q_\parallel$. In Fig. 3.11 we compare initial relaxation rates, which were calculated this way without any free parameter, to the experi-

mental data obtained from a $Q_{\|}$-scan with a ASM470 (hard sphere model system) suspension containing a sphere volume fraction of $\phi = 0.04$, and to the low density predictions, where no back reflection is considered. The model calculations coincide perfectly at low scattering vectors and the experimental data deviate less than five percent from the predictions. However, those data, which were calculated taking into account the effect of back reflection, strongly decrease at larger scattering vectors, which is exactly the same trend, that is observed for the experimental data. We are therefore led to conclude that the first cumulants obtained at high in-plane angles, i. e. $\theta > \pi/2$ should be considered with extreme care and potentially discarded when comparing experimental data to theoretical predictions and simulations.

4

Near–wall dynamics of hard sphere suspensions

This chapter will present the study of the near-wall dynamics of colloidal hard spheres over a broad range of volume fractions. A short introduction of the model system and the prediction methods is given in the first section. Experimental results are then thoroughly compared with the predictions based on a virial approximation and simulation.

4.1 Introduction

About thirty years ago, poly(methyl-methacrylate) particles, stabilized by a thin poly-12-hydroxystearic acid layer in solutions of index matching organic solvent mixtures were introduced by Pusey and van Megen as a model system for spherical colloids interacting only by excluded volume to a very good approximation [50]. The bulk dynamics of this system has been studied extensively following their ground breaking work [51, 52]. Only comparatively recently EWDLS experiments on the same system have been conducted to study the near-wall dynamics at volume fraction up till 42 percent, [24, 27] and corresponding theories have been developed [53]. Based on a heuristic approximation for the near-wall self-diffusivity, these studies suggest that for a concentrated hard sphere suspension, many-particle hydrodynamic interactions are diminished due to the presence of wall, which is referred to as 'screening out'. In this chapter, a more quantitative method is provided to determine the near-wall self-diffusion coefficients, and it is shown that the parallel and perpendicular self-diffusivity are affected differently. To describe and confirm the EWDLS experiments, we resort to two predictive methods: the virial expansion and precise multipole simulations, which will be briefly introduced in the following sections. First cumulant can be calculated by these two methods, and compared to experimental results. While simulation can be used for high accuracy calculations at any volume fraction, the virial expansion is expected to correctly reproduce the

experimental results up to moderate concentrations. The aim of this chapter is to systematically present the result on the near-wall dynamics in a hard sphere model system. For the first time a thorough analysis of the first cumulant over scattering vector is provided, which allows us to assess the range of volume fractions where virial approximation can be used to describe experimental data. By tuning the suspension volume fraction and the penetration depth, we are able to investigate the effect of hydrodynamic interaction diminishment for high concentrations and its anisotropic nature, in a more convincing way than proposed earlier.

4.2 Theoretical description

Using the Smoluchowski equation formalism, Cichocki *et al.* [54] derived an analytical expression for the first cumulant measured in an EWDLS experiment for a suspension of spherical particles,

$$\Gamma = D_0 \left[\frac{\kappa}{2}\hat{\mathbf{e}}_z - i\mathbf{Q}\right] \cdot \frac{\mathbf{H}_w(\kappa,\mathbf{Q})}{S_w(\kappa,\mathbf{Q})} \cdot \left[\frac{\kappa}{2}\hat{\mathbf{e}}_z + i\mathbf{Q}\right], \tag{4.1}$$

where the hydrodynamic function reads

$$\mathbf{H}_w(\kappa,\mathbf{Q}) = \frac{\kappa}{\mu_0 nA}\sum_{i,j}^{N}\left\langle \exp\left[-\frac{\kappa}{2}(z_i+z_j)\right]\boldsymbol{\mu}_{ij}^{w}\exp\left[i\mathbf{Q}\cdot(\mathbf{r}_i-\mathbf{r}_j)\right]\right\rangle, \tag{4.2}$$

and the wall-structure factor is given by

$$S_w(\kappa,\mathbf{Q}) = \frac{\kappa}{nA}\sum_{i,j}^{N}\left\langle \exp\left[-\frac{\kappa}{2}(z_i+z_j)\right]\exp\left[i\mathbf{Q}\cdot(\mathbf{r}_i-\mathbf{r}_j)\right]\right\rangle. \tag{4.3}$$

Here, nA/κ is the number of particles within the illuminated scattering volume, with n being the bulk particle number density, and A is the illuminated wall area. $\boldsymbol{\mu}_{ij}^{w}$ is the hydrodynamic mobility tensor. The brackets $\langle\ldots\rangle$ denote ensemble averaging. Eq. (4.1) is a generalization of the bulk result for concentrated suspensions [43]

$$\Gamma = D_0 \cdot Q^2 \cdot \frac{H(Q)}{S(Q)}, \tag{4.4}$$

which corresponds to the limit of infinite penetration depth or $\kappa \to 0$.
Decomposing the scattering vector into components parallel and perpendicular to the wall,

$$\mathbf{Q} = \mathbf{Q}_{\parallel} + \mathbf{Q}_{\perp} = Q_{\parallel}\hat{\mathbf{e}}_{\parallel} + Q_{\perp}\hat{\mathbf{e}}_z, \tag{4.5}$$

where $\hat{\mathbf{e}}_{\parallel}$ is a unit vector in the direction of $\mathbf{Q}_{\parallel}$ and using the invariant properties of the system, we arrive at the following structure of the first cumulant

$$\Gamma = \frac{D_0}{S_w}\left[\left(\frac{\kappa^2}{4}+Q_{\perp}^2\right)H_{\perp}+Q_{\parallel}^2 H_{\parallel}+\frac{\kappa}{2}Q_{\parallel}H_I+Q_{\parallel}Q_{\perp}H_R\right], \tag{4.6}$$

where

$$H_{\perp} = \hat{\mathbf{e}}_z \cdot \mathbf{H}_w(\kappa,\mathbf{Q})\cdot\hat{\mathbf{e}}_z, \tag{4.7}$$

$$H_{\parallel} = \hat{\mathbf{e}}_{\parallel} \cdot \mathbf{H}_w(\kappa,\mathbf{Q})\cdot\hat{\mathbf{e}}_{\parallel}, \tag{4.8}$$

$$H_I = \hat{\mathbf{e}}_z \cdot 2\mathrm{Im}[\mathbf{H}_w(\kappa,\mathbf{Q})]\cdot\hat{\mathbf{e}}_{\parallel}, \tag{4.9}$$

$$H_R = \hat{\mathbf{e}}_{\parallel} \cdot 2\mathrm{Re}[\mathbf{H}_w(\kappa,\mathbf{Q})]\cdot\hat{\mathbf{e}}_z, \tag{4.10}$$

with Im and Re standing for the imaginary and real part, respectively. The coefficients H as well as S_w may be either evaluated numerically using the virial expansion approach, or by extracted from numerical simulations. Both techniques are briefly described in the course of this work. The expressions given above are valid for an arbitrary wall-particle interaction potential. In this chapter, we restrict to hard-core interactions.

4.2.1 Virial expansion

For moderately concentrated systems, calculations of the wall structure factor S_w and the components of the wall-hydrodynamic tensor $\mathbf{H}_w$ may be performed by expanding them in terms of powers of bulk-particle concentration n far from the wall. The procedure has already been elaborated in great detail in Ref. [54]. Thus, we refrain here from the technical aspects, focusing on the resulting expressions.

The small dimensionless parameter in the density expansion is the bulk volume fraction,

$$\phi = \frac{4\pi}{3}a^3 n, \tag{4.11}$$

instead of the concentration n. The virial expansion of the wall-structure factor S_w reads

$$S_w(\kappa,\mathbf{q}) = S^{(1)}(\kappa)+\phi S^{(2)}(\kappa,\mathbf{q})+\mathscr{O}(\phi^2). \tag{4.12}$$

The analogous virial expansion of the wall hydrodynamic tensor requires a cluster decomposition of the mobility matrix [55], and has a similar form

$$\mathbf{H}_w(\kappa,\mathbf{Q}) = \mathbf{H}^{(1)}(\kappa) + \phi\mathbf{H}^{(2)}(\kappa,\mathbf{Q}) + \mathscr{O}(\phi^2). \tag{4.13}$$

Inserting the expansions (4.12) and (4.13) into Eq. (4.1), we find the following virial expansion for the first cumulant

$$\Gamma = \Gamma^{(1)}(\kappa,\mathbf{Q}) + \phi\Gamma^{(2)}(\kappa,\mathbf{Q}) + \mathscr{O}(\phi^2), \tag{4.14}$$

where the factor

$$\Gamma^{(1)}(\kappa,\mathbf{Q}) = D_0\left[\frac{\kappa}{2}\hat{\mathbf{e}}_z - i\mathbf{Q}\right]\cdot\frac{\mathbf{H}^{(1)}}{S^{(1)}}\cdot\left[\frac{\kappa}{2}\hat{\mathbf{e}}_z + i\mathbf{Q}\right], \tag{4.15}$$

is the infinite dilution prediction, given explicitly by Eq. (2.44), while the second term reads

$$\Gamma^{(2)}(\kappa,\mathbf{Q}) = D_0\left[\frac{\kappa}{2}\hat{\mathbf{e}}_z - i\mathbf{Q}\right]\cdot\frac{\mathbf{H}^{(2)}S^{(1)} - \mathbf{H}^{(1)}S^{(2)}}{(S^{(1)})^2}\cdot\left[\frac{\kappa}{2}\hat{\mathbf{e}}_z + i\mathbf{Q}\right]. \tag{4.16}$$

These virial expansion results, together with simulations that are also valid at high concentrations, will be compared to experiments in section 4.4. The relations above may be transformed using Eqs. (4.7)–(4.10) and expressed in terms of the tensorial components of the hydrodynamic function $\mathbf{H}_w$.

4.2.2 Numerical calculation

To determine the equilibrium wall-structure factor (4.3), the hydrodynamic functions (4.7)–(4.10), and the first cumulant (4.1), A series of numerical simulations for a wall-bounded hard-sphere system with particle volume fractions in the range $0 < \phi \leq 0.3$ have been carried out. Key elements of the numerical techniques and detailed description is provided in ref. [28, 54].

4.3 Experimental methods

4.3.1 Sample preparation

As model systems for the EWDLS experiments, we used two batches of poly (methyl methacrylate) (PMMA) particles, named ASM470 and ASM540 in the following, which were purchased from Andrew Schofield, University of Edinburgh. The spherical particles are covered with a thin poly-12-hydroxystearic acid layer to stabilize them against aggregation in organic solvents. To allow scattering experiments at high volume fractions the particles were

transferred from a cis-decaline suspension (as received) to a refractive index matching cis-decaline/tetraline mixture by spinning and re-dispersing them. The solvent used had a cis-decaline mass fraction of $w = 0.2$, a refractive index of $n_2 = 1.498$ and a viscosity of $\eta = 2.658$ mPas at temperature of $T = 298$ K as measured using an Abbemat RXA156 and an Automated Microviscometer AMVη from Anton Paar, Graz, Austria.

To determine the particle radius, we employed standard Dynamic Light Scattering (DLS) measurements. The recorded time auto-correlation functions of the scattered intensity $g_2(t)$ (IACF) were analyzed by three different methods, namely cumulant analysis, stretched exponential fitting and inverse Laplace transformation. The three methods resulted hydrodynamic radii of $R_H = 98$ nm (ASM470) and $R_H = 144$ nm (ASM540) with a variation of less than 1 nm in both cases. The relaxation rates, Γ, resulting from the stretched exponential fitting are plotted versus the squared scattering vector Q^2 as an example in Fig. 4.1. The resulting hydrodynamic radii are assumed to be identical with the hard sphere particle radii a in the following. Further, the size distributions obtained from inverse Laplace transformation showed a full width at half maximum of less than five percent. The negligible size polydispersity is confirmed by the observation that the suspensions crystallize at sufficiently large particle volume fractions.

Prior to the scattering experiments, the suspensions were filtered through PTFE syringe filters

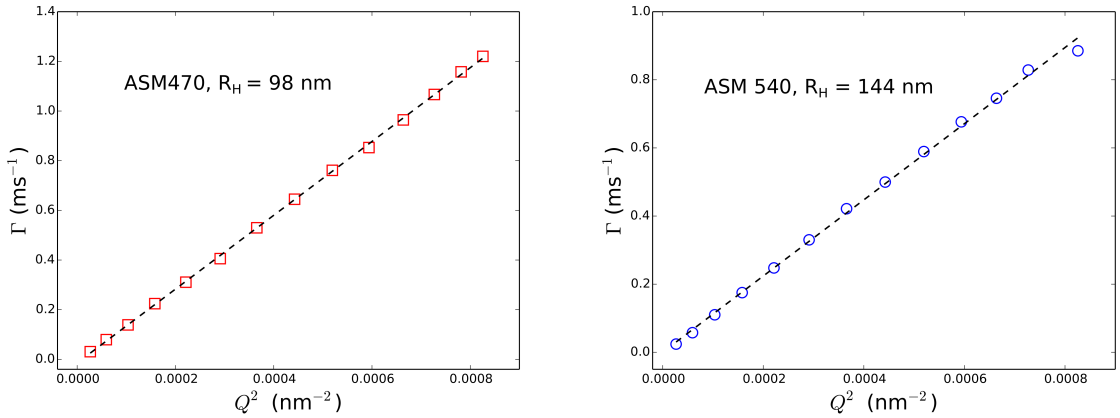

Figure 4.1: *Relaxation rates Γ versus Q^2 for hard sphere system ASM 470(left) and ASM540 (right) respectively measured in bulk. The experiments were conducted on very dilute particle suspension. Symbols represent experimental data obtained from particle suspensions with $\phi = 0.01$. Full lines linear fitting*

with a nominal pore size of 1 μm directly into the measurement cells to minimize the parasitic scattering from dust particles. To reduce the number of necessary alignment processes of the

EWDLS measuring cell, this was filled with the hard sphere suspension of highest volume fraction, and further dilution was achieved by removing a part of the sample and replacing it by pure solvent. The exact volume fraction was determined a posteriori by drying a 250 μl aliquot and determining the mass of the remaining particles. Further, the EWDLS sample cell was equipped with a small magnetic stirrer bar with which the samples were homogenized before each angular scan to minimize the influence of particle sedimentation.

4.3.2 Static and dynamic light scattering

The light-scattering measurements were performed on a commercial instrument by ALV-Laservertriebsgesellschaft (Langen, Germany) which is equipped with a HeNe Laser as a light source, an automated attenuator device, a Perkin Elmer avalanche diode and an ALV-6000 multiple tau digital correlator. Time averaged static scattering intensities were obtained by measuring count rates of the diode and correcting them for attenuator transmission, scattering volume and solvent background. Further, the scattering curves were normalized, using Toluene as a reference and dividing out the particle concentration. Static intensities were recorded in an angular range between 30° and 120° degree with an increment of two degree, Time auto-correlation functions of the scattered intensity $g_2(Q,t)$ were recorded in a range of scattering angles $30^\circ \leq \theta \leq 120^\circ$ in steps of ten degree. Here $Q = 4\pi n_S \sin(\theta/2)/\lambda_0$ is the scattering vector with n_S the refractive index of the solution and λ_0 the vacuum wave length of the laser. To determine the diffusion constant of the particles, D_0, and their polydispersity index, PDI, a cumulant analysis of the correlation functions was performed. The particles' hydrodynamic radius, R_H, is calculated via the Stokes-Einstein relation, using the appropriate solvent viscosity.

4.4 Results and discussion

To illustrate the influence of volume fraction on near-wall dynamics of hard spheres, we display experimental data of Γ obtained from EWDLS parallel scans versus scattering vector from $Q_{\|}$ scans on ASM470 suspension with different sphere volume fraction in Fig.4.2. Here and in the following, we will present dimensionless quantities, i. e. relaxation rates are displayed in units of D_0/d^2 and scattering vectors in units of $1/d$ where $d = 2a$ is the particles' diameter and D_0 is their bulk diffusion coefficient at infinite dilution. It is obvious that the experimental data at large scattering vectors deviate from the virial approximation displayed as full lines in Fig. 4.2 for all concentrations, which is fully explained by the the effect of back

reflections, discussed in section 3.4. Apart from this high-$Q_{\parallel}$ deviation, the virial approximation predicts the experimentally observed at data intriguingly correct, even at a sphere volume fraction of almost 25%.

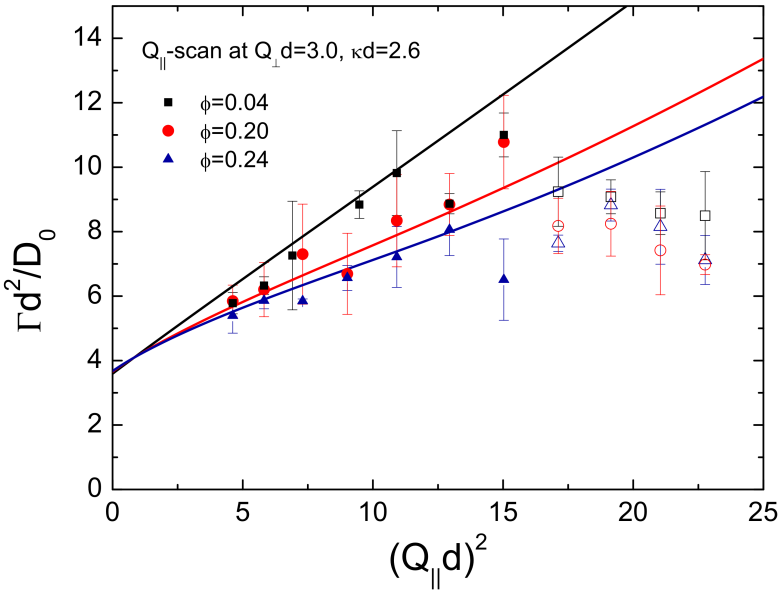

Figure 4.2: *Relaxation rates versus parallel component of the scattering vector. Symbols represent experimental data obtained at different volume fractions with $Q_{\perp}d = 3.0$ and $\kappa d = 2.6$, lines are prediction by the virial approximation and open symbols refer to data points which are obscured by the back reflection effect, discussed in section 3.4*

The same degree of agreement between virial approximation and experimental data is observe in $Q_{\perp}$-scans, which is shown in Fig. 4.3. Here we display experimental data obtained from ASM540 suspension with $\phi = 0.175$ performed at the same penetration depth $\kappa d = 2.08$ but extremely different values of parallel scattering vector component, i. e. $Q_{\parallel} = 1.83$ and $Q_{\parallel} = 5.7$. Together with these data we also present the results of computer simulations which where obtained for for a set of similar parameters, i. e. $Q_{\perp}d = 1.83$, $\kappa d = 2.08$ and $\phi = 01.5$. At low $Q_{\parallel}$ the results from all three methods agree very well, and at large $Q_{\parallel}$, where no simulation data are available, the agreement between experiment and virial approximation is also within experimental error.

Only at the highest volume fraction for which experimental data and simulations are available there is a significantly better agreement between simulation data and experiments than

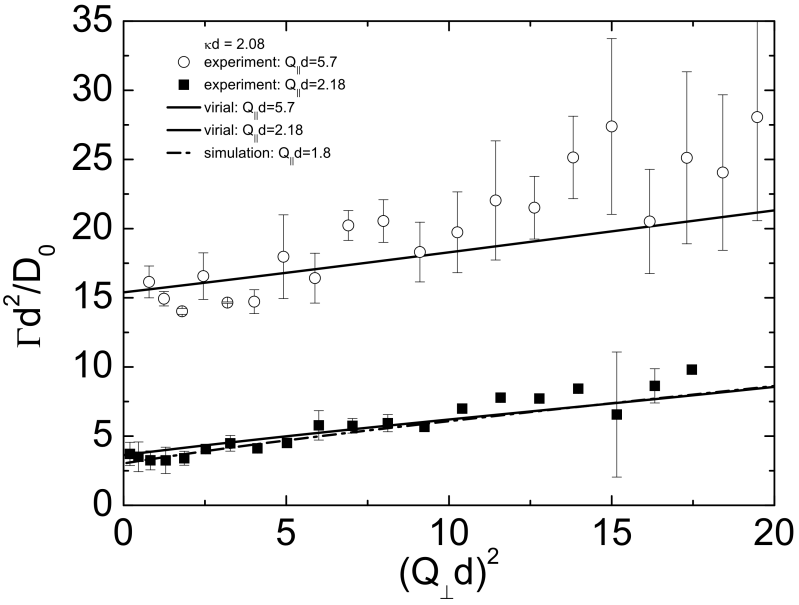

Figure 4.3: *Relaxation rates versus normal component of the scattering vector. Symbols represent experimental data obtained from a ASM540 suspension with* $\phi = 0.175$ *at different values of the parallel scattering vector component as indicated in the legend. Full lines are prediction by the virial approximation and the dashed dotted line refers to simulation results obtained for similar parameters, as indicated in the legend.*

between viral approximation and measured data. This is shown in Fig. 4.4 where we display data from a $Q_{\parallel}$ scan, obtained from an ASM540 suspension with $\phi = 0.3$ at $Q_{\perp}d = 2.36$ and $\kappa d = 2.08$ together with the corresponding predictions. Only at this high volume fraction the deviation between virial approximation and simulations is comparable or even larger than experimental error bars.

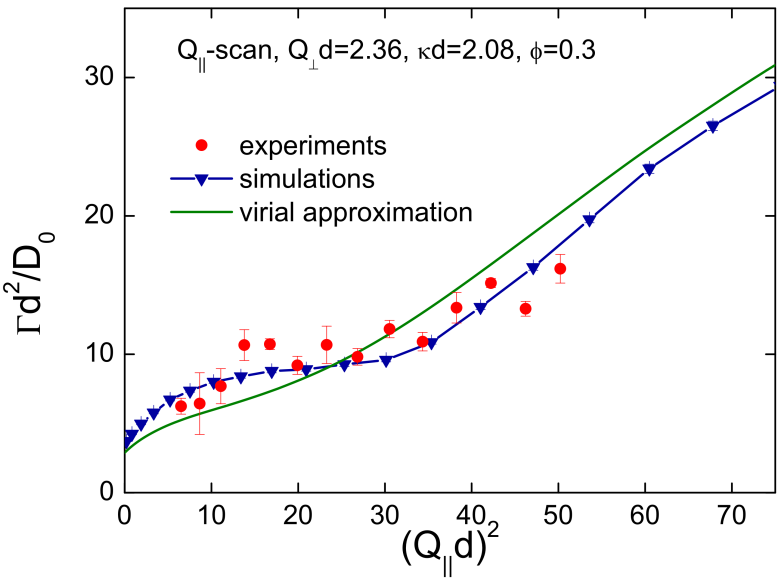

Figure 4.4: *Relaxation rates versus parallel component of the scattering vector. Symbols represent experimental data obtained from a ASM540 suspension with $\phi = 0.30$.Experimental parameters are indicated in the legend. The full lines are prediction by the virial approximation and the while the line with symbols refers to simulation results. Open symbols refer to data points, which are obscured by the back reflection effect discussed in section 3.4*

4.4.1 Comparison with bulk behavior

4.4.1.1 Self diffusion

It is interesting to investigate the limit of large scattering vectors, where self-diffusion is probed. As discussed in Section 3.4, the relaxation rates determined at the largest scattering vectors (and thus the largest angle θ) are not reliable. As first suggested by Pusey [56], self-diffusion can be probed approximately at a wave vector Q^* such that $S(Q^*) \approx S(Q \to \infty)$.

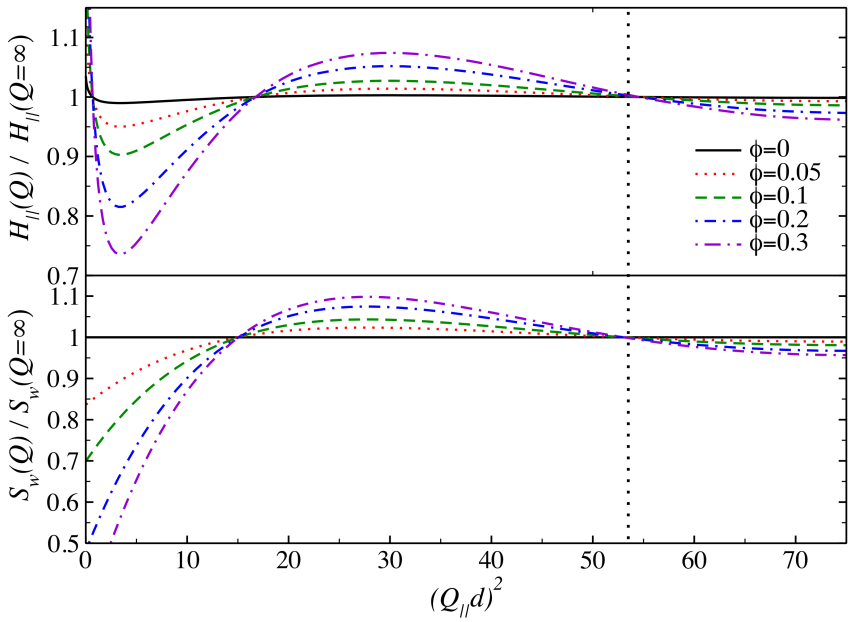

Figure 4.5: *The wall structure factor $S_w(Q)$ and the hydrodynamic function $H_{\|}(Q)$ in a $Q_{\|}$-scan at fixed $Q_{\perp}d = 2.36$ and $\kappa d = 2.08$ for a selection of volume fractions. Both functions are normalized by their self values at $Q \to \infty$. At $(Q_{\|}d)^2 \approx 53$ we find an isosbestic point for both functions (marked by a grey line), suggesting that the self diffusion coefficients may be determined from the data collected in the vicinity of this point. The statement also holds sway for other components of H.*

It is expected that at this point the distinct structure factor vanishes, and likewise does the distinct hydrodynamic function, so that only the self parts contribute to the dynamic properties at this point. In the bulk case, this statement was later corroborated by extensive numerical simulations [57] [58]. Segré et al. [57] stated that in a bulk suspension of hard spheres, this point is found for $Q^*a \sim 4.0$, where $S(Q^*a) = 1$, to the right of the main peak of $S(Q)$. As shown by Banchio *et al* [58], bulk structure factors of hard sphere suspensions with different volume fractions show an isosbestic point at $S(Qa = 4.02) = 1$ and at the same value of Qa the corresponding hydrodynamic functions attain their high-Q limit. Michailidou *et al.* [24] used the EWDLS experimental data at $Qa = 4.58$ arguing that this should not be too far from Q^*a, thus providing a good estimate of the near-wall self-diffusion coefficient. Here, we propose a more thorough way to determine the particles' near-wall self-diffusion properties which follows the same line of arguments as discussed for bulk systems above. We note here that in EWDLS both the structure factor and the hydrodynamic function become penetration-depth dependent [54]. However, upon re-scaling by their asymptotic values, both $S_w(\mathbf{Q})$ and the components of $\mathbf{H}_w(\mathbf{Q})$ exhibit an isosbestic point at which they attain their asymptotic values. We compute them using the virial expansion, and plot the results in Fig. 4.5. Like for bulk experiments, first cumulants obtained at the $Q_{\parallel,\perp}a$ values of the isosbestic point provide a good approximation for the near-wall self-diffusion coefficients.

However, as the first isosbestic point right of the structure factor main maximum is found approximately at $Q^*_{\parallel}d = 7.3$, we could determine experimental data of the first cumulant at this scattering vector mainly from the ASM540 suspensions. For the smaller ASM470 particles the data at $Q^*_{\parallel}d$ is distorted by the back-reflection effect (except for $\phi = 0.1$), and thus it may not be used to experimentally determine the self-diffusion coefficient parallel to the wall $\langle D^s_{\parallel}\rangle_\kappa$. Further, the experimentally accessible range of $Q_\perp d$ is in all cases much smaller than $Q^*_\perp d$ such that we can not get reliable experimental information on the self-diffusion properties normal to the wall.

In Fig. 4.6, we present the normalized ratios of $\langle D^s_{\parallel}\rangle$ over the bulk self-diffusion constant. The latter was calculated according to the semi-empirical formula [59]

$$\frac{D^s_b(\phi)}{D_0} = 1 - 1.8315\phi(1 + 0.12\phi - 0.65\phi^2), \tag{4.17}$$

which includes two virial coefficients due to Batchelor [60] and Cichocki *et al.* [55], and is expected to be accurate up to $\phi \sim 0.45$. Its validity has been extended by Riest *et al.* [61] up to $\phi = 0.5$ by modifying the coefficient of the last term to -0.70. We compare experimental data to predictions by virial approximation and simulations. The theoretical values for

$\langle D^s_{\parallel}\rangle_\kappa$ were determined by linearly extrapolating the high-Q range of the Γ vs $Q^2_{\parallel}$ dependence, making use of Eq.(18) in the paper [28]. Our experimental data confirm the trend predicted by both methods and show that the near-wall dynamics approach the bulk behavior at high particle volume fractions. With this observation we qualitatively confirm the earlier results by Michailidou *et al.* [24, 27]. Since the virial approach allows quick calculation of Γ vs $Q^2_{\parallel}$

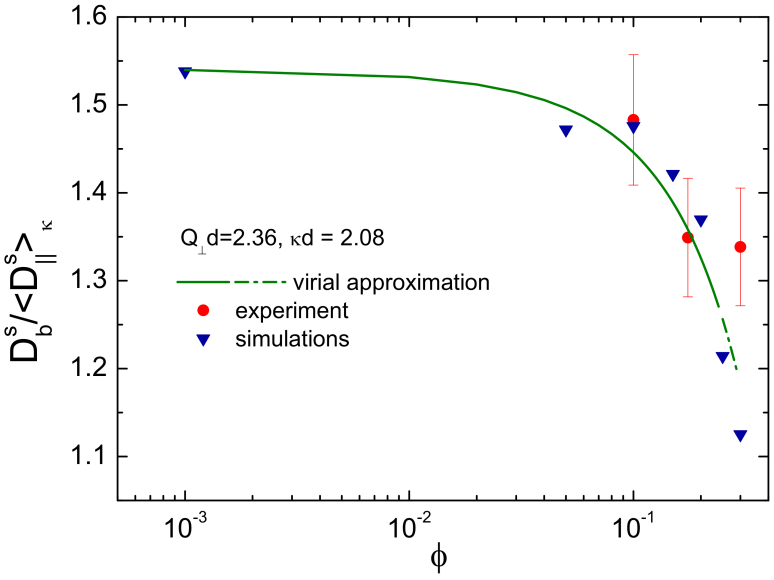

Figure 4.6: *Comparison of experimental data (full circles) obtained from ASM470 (R_H = 98 nm, $\phi = 0.1$) and ASM540 (R_H = 144 nm) suspensions, virial calculations (full line, the dashed dotted line represents virial calculations in a range of volume fractions where the approximation is not considered valid) and simulation results (triangles) for the self-diffusion coefficient parallel to the wall. Experimental parameters are at $Q_\perp d = 2.36$ and $\kappa d = 2.08$ for all cases.*

data, we can easily predict near-wall self-diffusion coefficients for a variety of parameters, by using the slope in the high Q-range. We use this possibility to quantitatively compare self-diffusion properties predicted by the virial approximation to the data by Michailidou. For this purpose we calculate $\langle D^s_{\parallel}\rangle_\kappa$ and $\langle D^s_{\perp}\rangle_\kappa$ for a series of volume fractions and average them as $\langle D^s_w\rangle_\kappa = (\langle D^s_{\parallel}\rangle_\kappa + \langle D^s_{\perp}\rangle_\kappa)/2$ according to their experimental procedure. Their choice of $Qa = 4.58$ is determined by the fact that they measured with a geometry which corresponds to $\theta = 0°$ and $\alpha_r = 90°$, thus at a scattering vector which makes an angle of 45° with the interface. In this configuration the parallel contribution and the normal contribution to self-diffusivity are weighted equally in the experiment. The comparison in Fig. 4.7 shows that

the prediction calculated by a 1 : 1 weighing of the normal and the parallel component are deviating systematically from the experimental data in the range of volume fractions, where the virial approach should hold. Only at very high volume fractions, where the virial approximation is certainly not valid the experimental data appear to agree with it. This is probably due to the effect that first cumulants obtained at $Qa = 4.58$ are not a good approximation for the self-diffusion properties. Actually simulations of bulk properties [58] show that even at moderate volume fractions, both the structure factor and the hydrodynamic function are significantly different from their value at $Q^*a = 4.02$. For the sake of completeness we also show predictions for the self-diffusion constants in Fig. 4.7, which are averaged according to $\langle D^s_w \rangle_\kappa = (2\langle D^s_\parallel \rangle_\kappa + \langle D^s_\perp \rangle_\kappa)/3$. These agree reasonably well with the earlier experimental data, which is probably a coincidence.

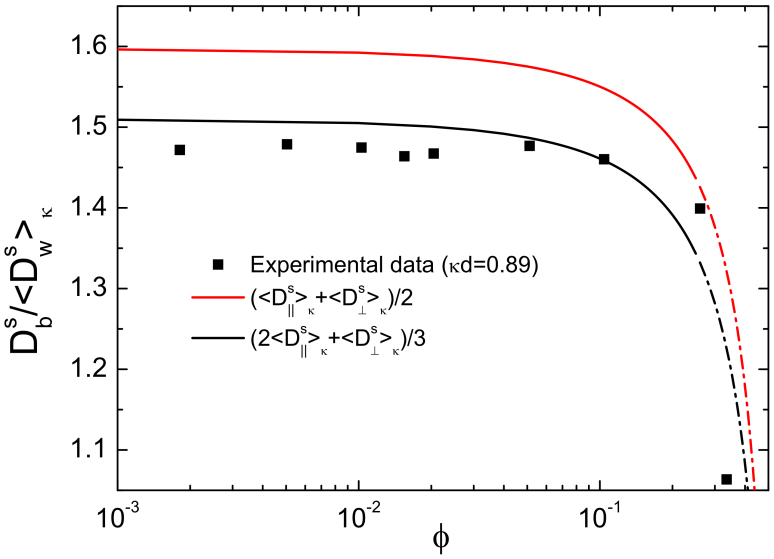

Figure 4.7: *Comparison of virial predictions for the self-diffusion coefficient with experimental data by Michailidou et al [24] measured at $\kappa d = 0.89$. The predicted data for normal and parallel contribution were averaged as indicated in the legend.*

Nevertheless, we confirm the earlier conjecture that particle-particle hydrodynamic interactions in the presence of a wall are diminished at high volume fractions as compared to bulk dynamics. However, here we can show that effect influences the diffusion parallel to the wall and normal to the wall differently. As discussed in Ref. [54], the anisotropic self-diffusion

coefficients have the following virial expansion

$$\frac{\left\langle D^s_{\parallel,\perp} \right\rangle_\kappa}{D_0} = G^{(1)}_{\parallel,\perp}(\kappa d) + \phi G^{(2)}_{\parallel,\perp}(\kappa d) + \mathscr{O}(\phi^2). \tag{4.18}$$

The coefficients of this expansion have been presented graphically in Fig. 3 of Ref. [54]. Here

Table 4.1: *The coefficients of the virial expansion of anisotropic self-diffusivity, defined in Eq. (4.18). The decay of the $\perp$ elements is faster with increasing penetration depth, indicating that both single- and two-particle mobilities are hindered more for motion in the direction normal to the interface.*

κd	$G^{(1)}_{\perp}(\kappa d)$	$G^{(2)}_{\perp}(\kappa d)$	$G^{(1)}_{\parallel}(\kappa d)$	$G^{(2)}_{\parallel}(\kappa d)$
0	1.0	-1.832	1.0	-1.832
0.2	0.781	-1.371	0.884	-1.535
0.5	0.644	-1.117	0.810	-1.357
1.0	0.516	-0.871	0.736	-1.160
2.0	0.383	-0.588	0.654	-0.903
5.0	0.227	-0.250	0.547	-0.550

we have tabulated them for a selection of penetration depths in Table 4.1. The coefficients have a clear interpretation: $G^{(1)}_{\parallel,\perp}$ refers to single-particle dynamics at infinite dilution, while $G^{(2)}_{\parallel,\perp}$ bears information on the effect of the wall on two-particle interactions. All coefficients decrease with increasing κd, but the effect is stronger for the motion perpendicular to the wall. The behavior of $G^{(1)}_{\parallel,\perp}$ follows from the single-particle physical picture [49], in which motion normal to the interface is suppressed more than in the parallel direction. This is due to the fact that perpendicular motion generates 'squeezing' flows which lead to stronger hydrodynamic resistance as compared to 'shearing' flows induced by parallel motion [62]. The particle-particle HI are affected in the same way, which explains the faster decay of $G^{(2)}_{\perp}$ as compared to $G^{(2)}_{\parallel}$. Thus, the coefficients corresponding to the normal motion are affected more strongly. However, the near-wall self-diffusivity is frequently written in the form

$$\frac{\left\langle D^s_{\parallel,\perp} \right\rangle_\kappa}{\left\langle D_{\parallel,\perp} \right\rangle_\kappa} = 1 - \alpha_{\parallel,\perp}(\kappa d)\phi + \ldots, \tag{4.19}$$

with $\left\langle D_{\parallel,\perp} \right\rangle_\kappa = D_0 G^{(1)}_{\parallel,\perp}(\kappa d)$. The coefficient

$$\alpha_{\parallel,\perp}(\kappa d) = \frac{G^{(2)}_{\parallel,\perp}(\kappa d)}{G^{(1)}_{\parallel,\perp}(\kappa d)}, \tag{4.20}$$

becomes a result of an interplay between the single- and two-particle effects. In Fig. 4.8 we show normalized ratios of $\langle D^s_\parallel \rangle_\kappa$ and $\langle D^s_\perp \rangle_\kappa$ over the bulk self-diffusion as a function of volume fractions for two different penetration depths of the evanescent wave. The curves are calculated using the virial approach up to a volume fraction of 25%. First we observe that the self-diffusion coefficient (averaged over the illumination profile) normal to the wall is smaller than that parallel to the wall and that both components increase with penetration depth κ^{-1}, similarly to the components of the near-wall diffusion coefficients at infinite dilution. The variation of these ratios over the range of volume fractions covered is indicated by the numbers on the far right of Fig. 4.8, which are the ratios of the values obtained at $\phi = 10^{-3}$ and $\phi = 0.25$. It appears that $\left\langle D^s_\parallel \right\rangle_\kappa / D^s_b$ varies stronger with increasing ϕ as compared to $\left\langle D^s_\perp \right\rangle_\kappa / D^s_b$.

4.4.1.2 General dynamics

As shown above by the study of self-diffusion, at high volume fraction, the near-wall dynamics of hard spheres are approaching the bulk dynamics. It will be interesting , to compare the near-wall dynamics and the bulk dynamics through the whole Q-range, which can be probed experimentally. In this section we will extend the discussion to the general dynamics, which are observed at finite scattering vectors. As a starting point, we will we will briefly discuss the bulk dynamics of HS-particles at increased concentration.

Increasing the volume fraction of particles will lead to an increasing degree of ordering in particle suspensions, even if the particles interact by excluded volume only. This effect can be observed in static scattering experiments by measuring the static structure factor of the solution, which according to eqs. (2.7) and (2.8), can be very well approximated by

$$S(Q) = \frac{I(Q,\phi)}{I(Q,\phi_0)} \frac{\phi_0}{\phi}. \tag{4.21}$$

Here $I(Q,\phi_0)$ represents a scattering curve which was measured at a volume fraction ϕ_0 which is small enough to grant $S(Q) \approx 1$ throughout the entire observed range of scattering vectors. Structure factors measured by this method, from solutions of ASM470 are shown in the top part of Fig. 4.9 together with predictions for the structure factor by the Percus-Yevick

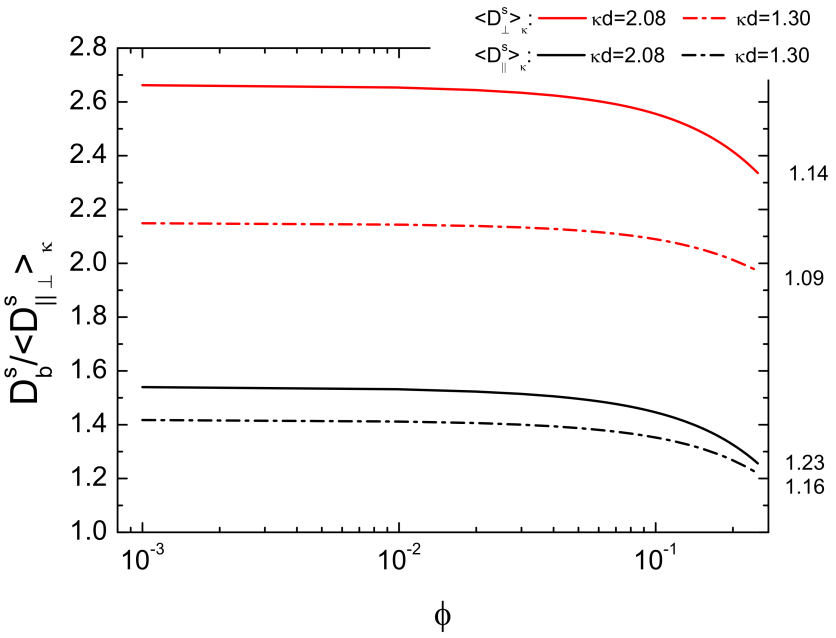

Figure 4.8: *Calculated data for the self-diffusion coefficients parallel and normal to the wall for different penetration depths:* $\kappa d = 2.08$ *full lines and* $\kappa d = 1.3$ *dashed dotted lines. The numbers on the far right represent the ratio of the values at* $\phi = 10^{-3}$ *over* $\phi = 0.25$*, which are an indication that the diminishing of hydrodynamic interaction is more pronounced for particle motion parallel to the wall than normal to the wall.*

approximation [63, 64]. The predictions are calculated without any adjustable parameter for spheres with a radius of $R = 98$ nm and the volume fractions indicated in the figure legend. It is obvious that the experimental data are very well described by the predictions in the entire observable Q-range, which however does not extend to the first maximum in the structure factor.

The influence of increased volume fraction on the particles short time dynamics can be investigated by analyzing the Q-dependence of the correlations functions' initial decay rate. While at low volume fraction $\Gamma(Q) = D_0 Q^2$, it is given by

$$\Gamma(Q) = D_0 Q^2 \frac{H(Q)}{S(Q)} \tag{4.22}$$

at volume fractions, which are large enough to make $S(Q)$ and $H(Q)$ deviating significantly from unity. Here $H(Q)$ is the the hydrodynamic function, reflecting the particles hydrodynamic interaction. Experimental data of the hydrodynamic function at different volume fractions are displayed in the bottom part of Fig. 4.9 together with theoretical predictions, which were calculated using the self-part corrected Beenakker Mazur scheme [65–67], as discussed in detail by Riest *et al.* for spherical colloidal particles with internal hydrodynamic structure [61].

Like the predictions for the structure factors, those for $H(Q)$ were calculated without using any adjustable parameters. The agreement between experimental and and theoretical data is not as good as in the case of the static data. This is probably due to the fact that the experimental hydrodynamic function is a product of three experimental data sets, which leads to a significant increase of the uncertainty of the $H(Q)$. Nevertheless, we will use the calculated hydrodynamic bulk functions to compare to the experimental EWDLS-data, where no experimental bulk data are available.

In Figs. 4.10 and 4.11 we show the near-wall dynamics data together with the corresponding data in bulk, obtained at the same volume fraction. Since there are no bulk data available for a sample with $\phi = 0.30$ we compare the EWDLS-data measured at this volume fraction to the theoretical prediction based on the corresponding bulk hydrodynamic function, and to bulk data obtained at $\phi = 0.36$ in Fig. 4.12. It is obvious from those graphs that the near-wall dynamics are significantly slower than the bulk dynamics in the range of accessible scattering vectors at all volume fractions probed. Although the general shape of the Q-dependence in bulk and near-wall are very similar at the highest volume fraction, the relaxation rated in EWDLS ares still by approximately a factor of two smaller than expected in bulk. Only the

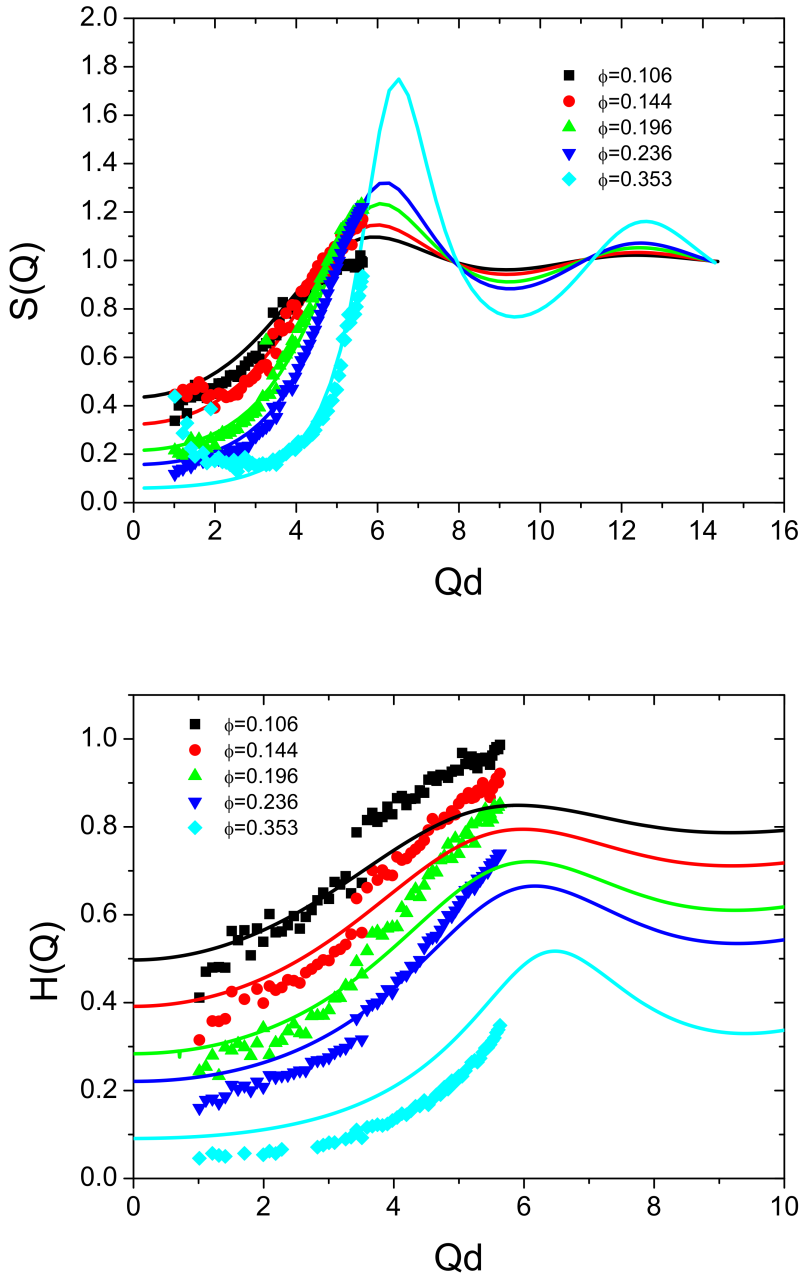

Figure 4.9: *Symbols: Structure factors $S(Q)$ (top) and hydrodynamic functions $H(Q)$ (bottom) measured in samples of ASM470 ($R_H = 98$nm) at different volume fractions as indicated in the legend. Full lines are theoretical predictions by the Percus-Yevick approximation for $S(Q)$ (top) and for $H(Q)$ (bottom), which were calculated using the self-part corrected Beenakker Mazur scheme.*

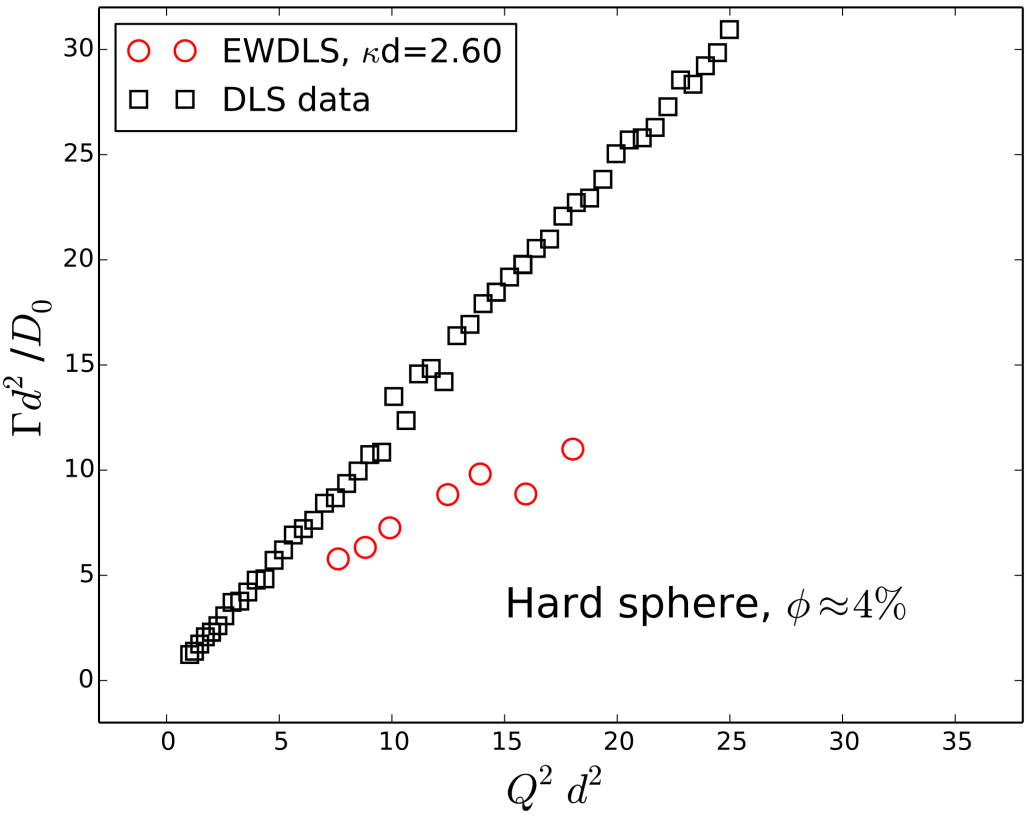

Figure 4.10: *Comparison of normalized experimental data on bulk- and near-wall dynamics of hard sphere suspension at $\phi \approx 4\%$. Bulk measurement is conducted on ASM490 (R_H=98 nm) at ϕ=3.6%; EWDLS measurement is conducted on ASM490 (R_H=98 nm) at ϕ=4%, κd=2.60, and $Q_\perp d$=3.0.*

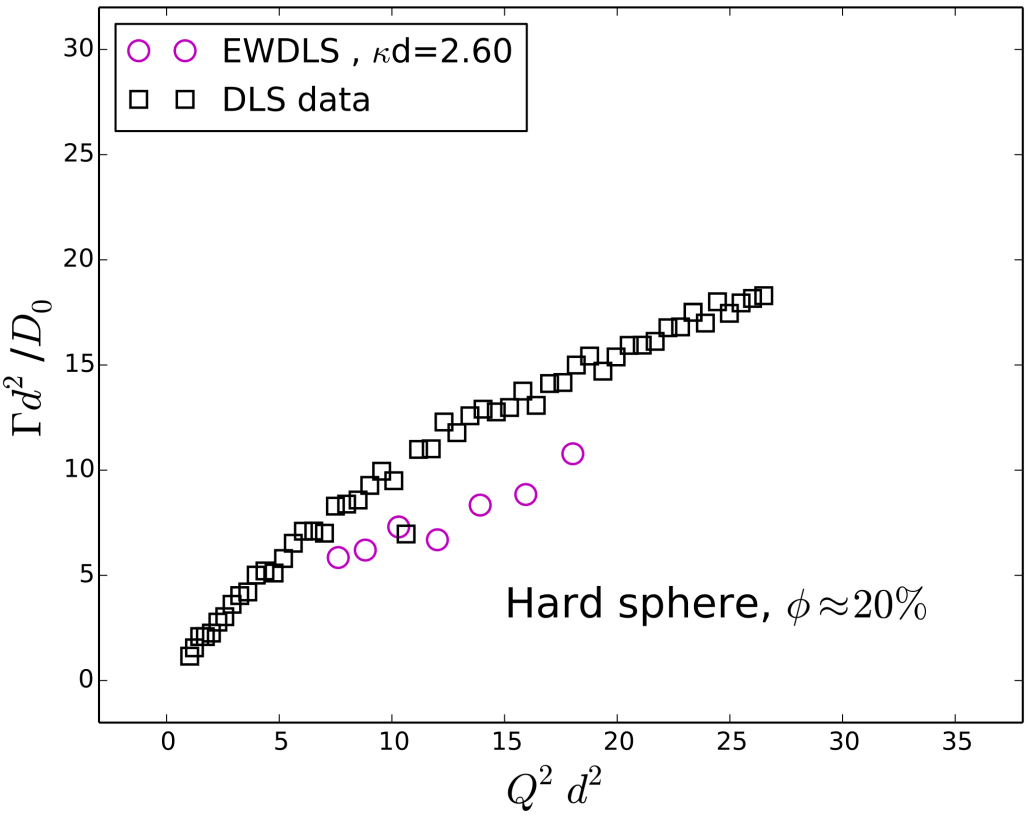

Figure 4.11: *Comparison of normalized experimental data on bulk- and near-wall dynamics of hard sphere suspension at $\phi \approx 20\%$. Bulk measurement is conducted on ASM490 (R_H=98 nm) at ϕ=19.6%; EWDLS measurement is conducted on ASM490 (R_H=98 nm) at ϕ=20%, κd=2.60, and $Q_\perp d$=3.0.*

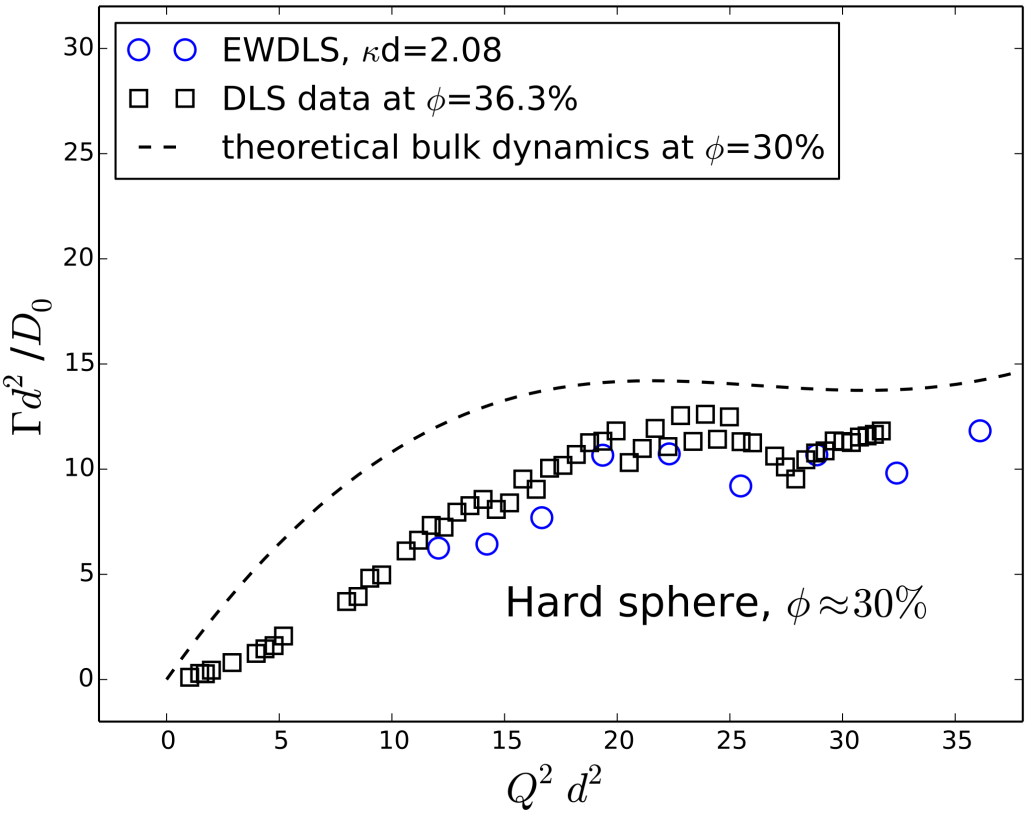

Figure 4.12: *Comparison of normalized experimental data on bulk- and near-wall dynamics of hard sphere suspension at $\phi \approx 30\%$. Bulk measurement is conducted on ASM490 (R_H=98 nm) at ϕ=36.3%; EWDLS measurement is conducted on ASM540 (R_H=144 nm) at ϕ=30%, κd=2.08, and $Q_\perp d$=2.36. Dashed line represents the theoretical prediction for bulk dynamics at ϕ=30%.*

experimental relaxation rates obtained in bulk at $\phi = 0.36$ appear to be as small as those observed with EWDLS in a sample with a volume fraction of 30%.

4.5 Conclusion

This chapter has described the EWDLS investigation on the near-wall dynamics of hard sphere system, with volume fraction up till $\phi = 30\%$. We thoroughly compare experimental data for the dependence of the first cumulant on the scattering vector components parallel and normal to the interface to corresponding predictions based on a second order virial approximation and to simulation results, where the full hydrodynamic interaction is taken into account. Up to volume fractions of about fifteen to twenty percent we find perfect agreement between the three methods. Above this range, the predictions by the virial approach deviate discernibly from the simulation data, however this deviation is still in the range of experimental error bars. Therefore we conclude that the virial approach provides a good approximation for the prediction and analysis of experimental data up to a volume fraction of about 25%, which is much less time consuming and elaborate than full scale simulations. Only at $\phi = 0.3$ the virial approximation is clearly not anymore able to capture the details of the dependence of the first cumulant on the scattering vector. Another major point is, we introduce a new method to assess the particles' near-wall self- diffusivity from experimental data. This method follows the same line of argument, which is used to assess bulk self- diffusivity in cases where the limit of sufficiently high scattering vector cannot be reached experimentally. We identify an isosbestic point of the near-wall structure factors right to the first maximum, where near-wall structure factor and hydrodynamic function attain their asymptotic values. Diffusion data measured at the scattering vector of the isosbestic point are a good approximation for the self-properties. Comparison of experimental data with predictions, based on the virial approach and on simulations, show that this method yields better estimates of the self-diffusivity as methods used earlier. Finally we confirm earlier data which show that the diminishment of particle-particle hydrodynamic interactions due to the presence of wall is less pronounced at high fraction compared to bulk dynamics. Beyond that, we show (see Table 4.1) that the observed effect is weaker for the mobility parallel to the wall as compared to motion in the normal direction. In conclusion, with the virial approximation, we have a method at hand, which qualitatively supports earlier data, but provides significant further insight into the near-wall dynamics of colloidal hard spheres. This is especially important since it should be possible to adopted this approach to systems with long ranging static interaction, providing a quick and non-costly method for the prediction and analysis of EWDLS results obtained from e.g. charged colloids.

Finally we compare not only the self diffusive coefficients near walls to bulk properties, but the also general dynamics which are observed throughout the accessible range of scattering vectors. We observe that for hard spheres the general near-wall dynamics are significantly slower than in the bulk at all volume fractions up to $\phi = 0.3$.

5

Bulk properties and near-wall dynamics of aqueous model system

This chapter will present the near-wall dynamics of a novel aqueous colloid system, with long range interactions. First, the synthesis and bulk characterization of the model colloidal system will be described. Then, bulk light scattering will be presented. Finally, the near-wall dynamics of this system studied by EWDLS will be discussed.

5.1 Introduction

Soft matter at aqueous interfaces has acquired a growing attention from scientific community and industry during recent years. Water-based system not only provides a green alternative to many industrial products, but also serves as a natural environment for biological processes. Despite its high potential, EWDLS has not been employed to study the near-wall dynamics of particles in aqueous solution, except for very dilute suspensions. The main challenge is to find a suitable aqueous model system, which is monodisperse and can be refractive index-matched to the aqueous solvent to avoid multiple scattering. To this end, the fluorinated monomer 2,2,3,3,4,4,4-heptafluorobutyl methacrylate (FBMA) has been successfully used to synthesize monodisperse particles with a low refractive index via emulsion polymerization and the system was shown to form well-ordered crystalline colloidal arrays [68]. Further effort has led to the production of FBMA particles with radii between 50 nm to 700 nm [69]. However, such particles are susceptible to irreversible aggregation upon salt addition or under compression by centrifugation, as they are solely stabilized through electrostatic repulsion (ER) in aqueous solution. This would bring great difficulty into volume variation and interaction tuning, which is essential for the study of near-wall dynamics in dense suspensions. This situation calls for a

more robust aqueous model system. The first attempt in this direction was made by Wiemann et al, who designed a core-shell system with a fluoroacrylate core and a poly(ethylene glycol) (PEG) surface layer, for the study of glass transition and re-entry behavior [70]. These so-called PEGylated particles are sterically stabilized in aqueous solution by the PEG layer, and were shown to be stable against compression up to a particle volume fraction of 69% and high salt concentrations. Continued effort has made it possible to synthesize particles with a single and well-defined PEG layer [71]. Moreover, this system bridges fundamental research to life science application, as PEG is a biocompatible material and e. g. PEGylation has already been widely used for drug delivery applications [72, 73].

In this paper we show that PEGylated FBMA particles are an interesting model system for the study of near-wall dynamics in aqueous solution for several reasons. First of all, they fulfill the requirements of being monodisperse, iso-refractive with aqueous solvents and stable, which ensures reliable EWDLS measurements; secondly, they are highly versatile, as their interactions can be tuned by varying the PEG chain length, the solvent composition, and salt concentrations where the PEG-layer should ensure colloidal stability even at high salt concentration. We describe the synthesis of the particles by emulsion polymerization and their bulk characterization, by cryo transmission electron microscopy (cryo-TEM) and light scattering. Finally we show that the near-wall dynamics of this model system is in very good agreement with current theoretical predictions for low particle volume fractions. However, due to the long range particle-particle interactions and those between the particles and the wall, the effect of increased concentration on the particles' near-wall dynamics is much more pronounced than for suspensions of colloidal hard spheres.

5.2 Experimental

5.2.1 Materials and synthesis

5.2.1.1 Materials

The fluorinated monomer 2,2,3,3,4,4,4-heptafluorobutyl methacrylate (HFBMA, 97%) was purchased from Alfa Aesar. Prior to use, the inhibitor hydroquinone was removed by washing the monomer three times with a 5% NaOH (w/v) solution. The macromonomer methoxy poly(ethylene glycol) acrylate with a molecular weight of M_n=950 g/mol was purchased from Sigma-Aldrich. To remove the inhibitor, the PEG macromonomer was dissolved in water and passed through a inhibitor remover packed column (CAS, Sigma-Aldrich). Dimethylsulfoxide

(DMSO) was purchased from Merck. The initiator, potassium peroxodisulfate ($K_2S_2O_8$), was obtained from Sigma-Aldrich.

5.2.1.2 Synthesis

The PEGylated fluorinated particles were prepared by surfactant free emulsion polymerization, following the procedure given in reference [71]. Fig 5.1 shows the synthesis scheme. In a typical synthesis, 1000 ml H_2O are deoxygenated three times in a 3L three-necked round bottom flask by firstly applying vacuum and afterwards flooding with nitrogen. After deoxygenation, 34.9091 g (130 mmol) HFBMA and 69.7 ml of an acryl-PEG solution (10 g dissolved in 100 ml water; 6.97 g; 7.34 mmol) are added under inert gas countercurrent. The emulsion is heated to 70°C under reflux cooling, and vigorous stirring (we used a magnetic stirrer bar which was driven by a motor with a nominal speed of 310 rpm). After 1 hour of homogenization the stirring speed is reduced to nominally 150 rpm and an adapter for a PTFE tube is added to the flask. A solution of 301 mg (1.1 mmol) $K_2S_2O_8$ in 10 ml H_2O and is added with a syringe pump through the PTFE tube to the reaction mixture within 20 min. After the injection is finished the reaction mixture turns turbid with a bluish color. The input adapter is removed and the reaction is allowed to proceed for twenty hours. After cooling, the mixture is filtered through a Büchner funnel. To remove unreacted educts, the dispersion is dialyzed for 7 days against deionized water from a Milli-Q water purification system with a resistivity of 18.2 $M\Omega/cm$, changing the water twice a day. The solid content of the dialyzed dispersion was determined gravimetrically by drying 1 mL solution at 100°C under reduced pressure, weighing the solid remains and calculating the average solid content.

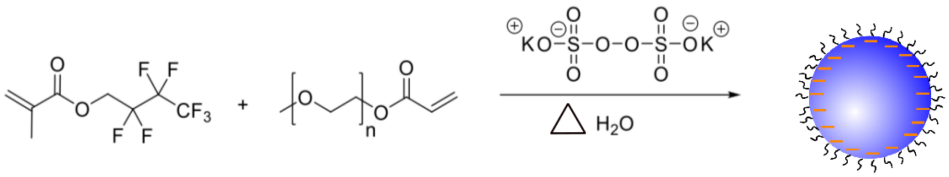

Figure 5.1: *Synthesis scheme for PEGylated FBMA particles.*

5.2.2 Bulk characterization methods

5.2.2.1 Static and dynamic light scattering

The light scattering setup and measurement procedure have been described in Chapter 4 section 4.3. Static intensities were recorded in an angular range between 30° and 120° degree with an increment of two degree. Time auto correlation functions of the scattered intensity $g_2(Q,t)$ were recorded in a range of scattering angles $30° \leq \theta \leq 120°$ in steps of ten degree. Here $Q = 4\pi n_S \sin(\theta/2)/\lambda_0$ is the scattering vector with n_S the refractive index of the solution and λ_0 the vacuum wave length of the laser. To determine the diffusion constant of the particles, D_0, and their polydispersity index, PDI, a cumulant analysis of the correlation functions was performed. The particles' hydrodynamic radius, R_H, is calculated via the Stokes-Einstein relation, using the appropriate solvent viscosity.

5.2.2.2 Cryo transmission electron microscopy: cryo-TEM

Transmission cryo electron microscopy (cryo-TEM) was used to evaluate the morphology and size of the colloidal particles. 3μL of a solution was applied on a hydrophilic Quantifoil TEM grid. In order to obtain a thin vitreous ice layer, the excess of solution was blotted for 2.5 seconds with a filter paper and the grid was plunged into liquid ethane in a FEI Vitrobot. The specimen was maintained at a temperature of approximately -196°C using a cryo holder. Bright field TEM images were acquired on a FEI Spirit TEM operated at 120 kV. Since conventional TEM images correspond to two-dimensional (2D) projections of three-dimensional (3D) objects, electron tomography was performed to investigate the morphology of the colloidal particles. A series of 2D projections was acquired while tilting the specimen around an axis perpendicular to the electron beam over the range from -65° to 60° with an increment of five degree. After alignment, the 2D images were reconstructed by the Simultaneous Iterative Reconstruction Technique (SIRT) algorithm in the Astra Toolbox [74].

5.2.2.3 EWDLS

The instrumentation and data analysis of evanescent wave dynamic light scattering are explained in detail in the fundamental Chapter 2 and method Chapter 3.

5.3 Results and discussion

5.3.1 Particle characterization

5.3.1.1 Synthesis and general properties

We prepared FBMA latex particles which are charge stabilized in aqueous media and which are additionally stabilized sterically by chemically attached PEG chains, according to a semi-batch emulsion polymerization procedure [71]. Electrophoresis measurements using a Malvern Zetasizer 2000, show that the particles behave as charged spheres at low ionic strengths with a zeta potential of -30mV. The density of particles was determined to be 1.5266 g/mol with a density meter (Anton Paar DMA 4500). Given a particle radius of $R \approx 130$nm (see section on cryo-TEM and bulk light scattering) this density results a sedimentation length $L_s \approx 300R$, indicating that sedimentation should not significantly influence the results of the EWDLS experiments which were performed to investigate particle near-wall dynamics. This is experimentally verified by the typical standard deviations of repeated EWDLS measurements, as shown by the error bars in Fig. 5.10.

The particles yield turbid suspensions, if dispersed in water at volume fractions above $\phi \gtrsim 0.01$, since the refractive index of the fluorinated polymer is higher than that of water. In order to conduct light scattering measurement at higher concentrations, the refractive index of the particles needs to be matched to the surrounding medium by adding a co-solvent. DMSO was chosen as co-solvent because of its miscibility with water in all proportions, and very its low toxicity. A series of DMSO/water solutions was prepared, with refractive index ranging from 1.33 to 1.40. To keep the particle concentration constant in all cases, 0.2 ml of a dialyzed stock suspension were added to 0.8 ml DMSO/water mixtures of various compositions. The scattering intensities of the resulting samples were measured at a scattering angle of $\theta = 90^o$, as the scattering intensity at constant volume fraction is approximately proportional to the square of the refractive index difference between the solvent and the particles. At a volume ratio of water to DMSO, $\phi(H_2O) : \phi(DMSO)$ of 69:31, the scattering intensity shows a minimum, which corresponds to the smallest obtainable refractive index difference between particles and solvent. The procedure is shown in Fig. 5.2 The refractive index at this solvent composition was determined to be $n_{sol} = 1.3847$, with an ABBEMAT RXA 156 refractometer from Anton Paar.

To obtain index-matched suspensions for further scattering experiments, the aqueous suspension was centrifuged at low speed and the sediments re-dispersed in the index-matching sol-

vent mixture, for three times. The resulting dispersion is completely transparent and used as stock solution, as shown Fig. 5.2

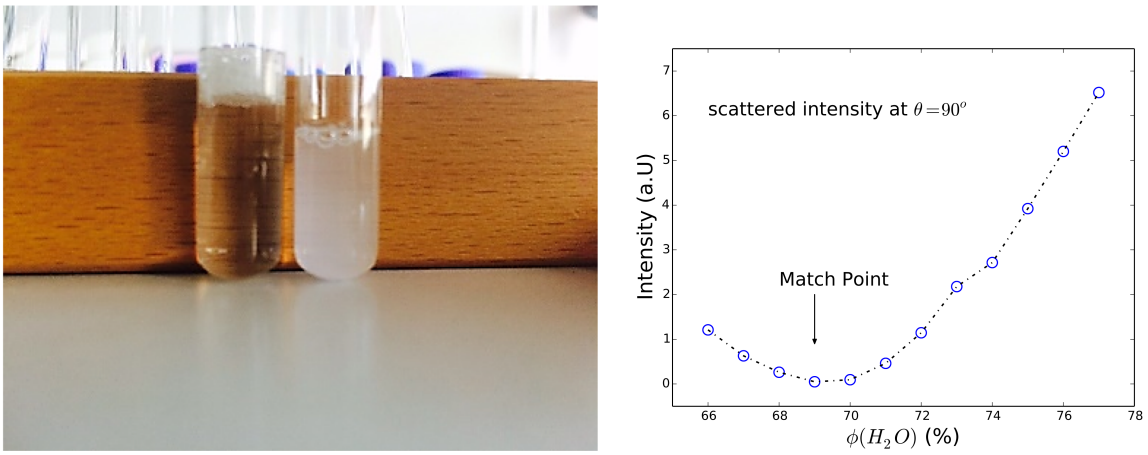

Figure 5.2: *Scattered intensity at θ=90 versus solvent composition, with fixed particle concentration(left), particle dispersion in index matched solvent mixture and in water*

5.3.1.2 Cryo-TEM

The shape and size of the particles were observed by cryo-TEM. In Fig. 5.3 we show representative images of single particles and some clusters which formed due to the blotting. The interfaces between the voids of the clusters and the spheres appear blurred, which we speculate might be due to the PEG chains. A total of 132 spheres were investigated to determine the mean particle radius and the relative standard deviation, which were found to be $R = 118$nm and $\sigma_r = 0.05$, respectively.

To confirm the spherical shape of the particles they were investigated by cryo-electron tomography. A series of 2D projections was acquired while tilting the specimen around an axis perpendicular to the electron beam (x-axis) over a range from -65° to +60° with a tilt increment of 5°. Example images from this series are shown in Fig. 5.4, where the perfectly circular shape of the 2D projection can be observed for all tilt angles. This observation is supported by the calculated 3D reconstruction which is displayed in Fig. 5.5

The elongation of the 3D-reconstruction, which is observed in the zx and xy planes, is an artifact, which is caused by the limited number of acquisitions and the so-called missing wedge problem. The missing wedge is caused by the inability to tilt the sample over $\pm 90°$ range. This is related to the limited gap between the pole pieces of the objective lens and shadowing effects of the TEM grid at high angles [75]. As the 3D reconstruction is mathematically speaking an

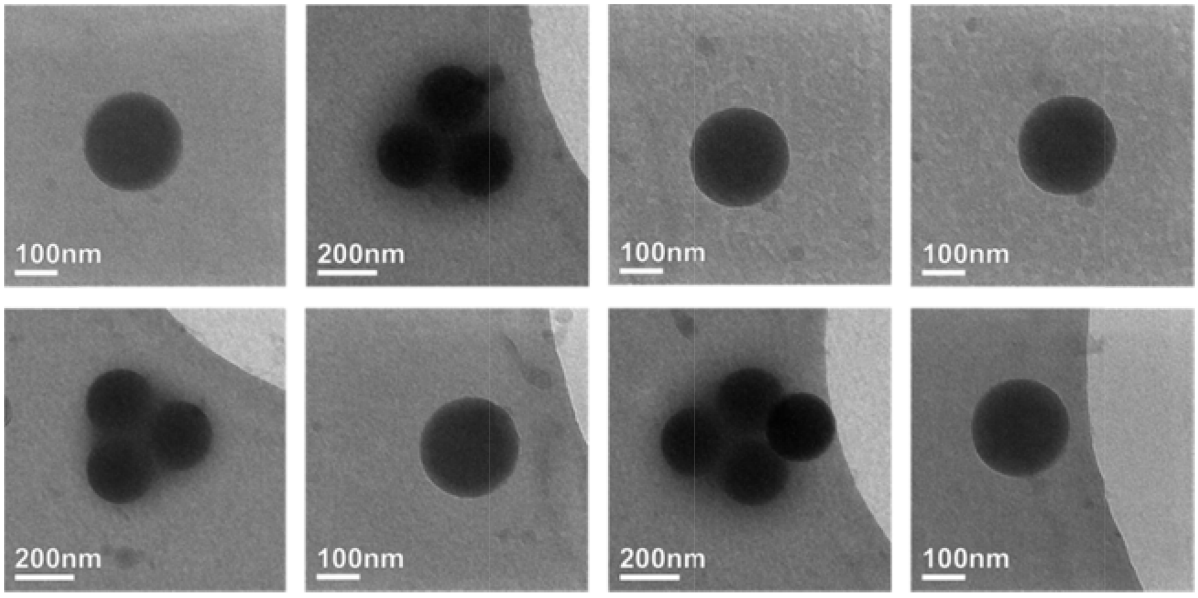

Figure 5.3: *Cryo-TEM images of single PEGylated FBMA particles and clusters*

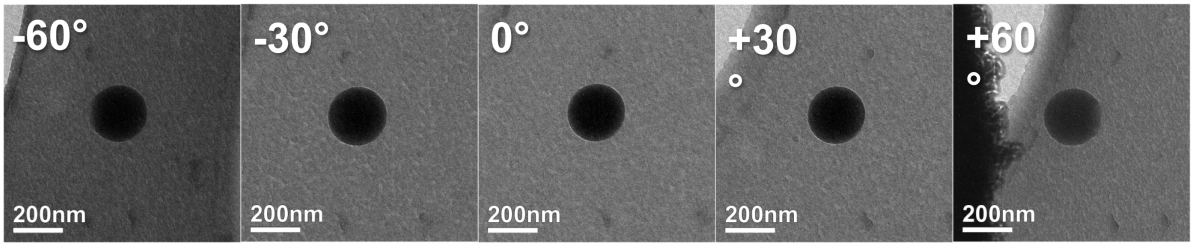

Figure 5.4: *2D projections of PEGylated FBMA particles as observed during a tomographic tilt series.*

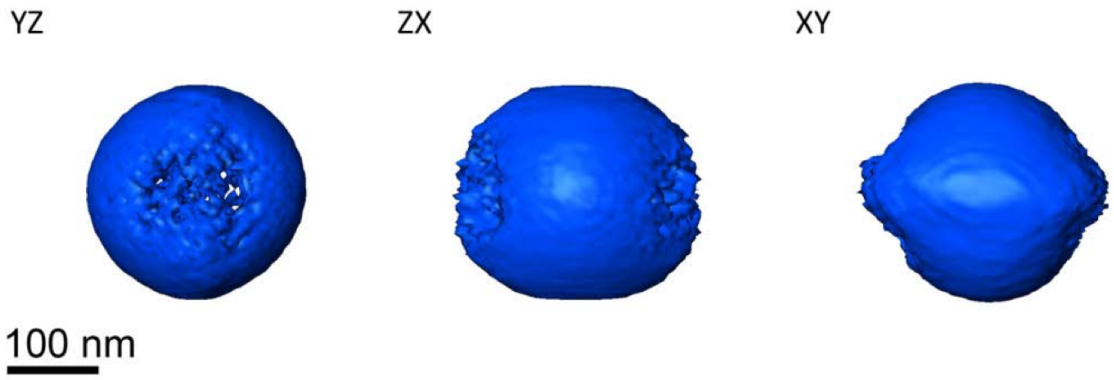

Figure 5.5: *Visualization of the 3D reconstruction. In the yz plane a spherical shape is observed, while in the zx and xy planes the reconstruction is elongated along the direction of the missing wedge*

ill-defined inverse problem, multiple solutions correspond to the incomplete data set that was collected. This eventually results in a blurring/elongation of the reconstruction in the direction of the missing wedge.

5.3.1.3 Static light scattering and phase behavior

For a characterization of the particles in solution, combined static and dynamic light scattering experiments were performed. All the scattering data from bulk samples which will be discussed later were obtained from suspensions without any added salt. Therefore the salinity is about 10^{-5}mol/L due to carbon dioxide adsorption, corresponding to a Debye screening length of $l_D \approx 95$ nm. The time-averaged static scattering intensity, expressed in absolute intensities as the Rayleigh ratios $R(Q)$, from three samples with low volume fractions is shown in Fig. 5.6. The data obtained from the samples with different volume fractions, ϕ, in DMSO/water could be superimposed perfectly by dividing out the particle concentration, which indicates that at least up to $\phi = 0.014$ there is no discernible effect of the solution structure factor on the scattering curve. Intriguingly the shape of the scattering curve from the suspension in pure water differs significantly from the curves obtained from samples which were dispersed in the index-matching solvent. The latter two curves show a distinct minimum which could be misinterpreted to indicate a particle radius of about 200 nm. For homogeneous spheres the position of the first minimum in the particle form factor is related to the particle radius by $RQ_{min} \approx 4.49$. Thus for particles with a radius of about 120nm, as indicated by cryo-TEM, the first minimum should occur at $Q_{min} \approx 0.037\text{nm}^{-1}$, while here we find $Q_{min} \approx 0.023\text{nm}^{-1}$

Table 5.1: *Best fitting parameter values obtained from fitting the static light scattering data to eq. 5.2*

solvent volume fraction	H_2O 0.0056	H_2O/DMSO 0.0056	H_2O/DMSO 0.014
$\langle R_c \rangle / nm$	115.3	115.3	115.3
$\langle R \rangle / nm$	121.2	121.2	121.2
σ_r	0.08	0.08	0.08
n_c	1.3838	1.3839	1.3839
ns	1.3549	1.400	1.3999

implying a particle radius significantly larger than observed in cryo-TEM. This is a strong indication that the particles are not optically homogeneous spheres but rather exhibit a variation of the scattering contrast with distance from the particle center [76, 77]. We therefore fitted the static scattering data obtained from the particles in the index-matching solvent using the form factor of a core-shell particle with a core radius R_c and an outer radius R which is given by

$$\begin{aligned} P(Q) &= \{\frac{4\pi}{Q^3 V_\varepsilon}[\Delta\varepsilon_{cs}(\sin(QR_c) - QR_c\cos(QR_c)) \\ &+ \Delta\varepsilon_{ss}(\sin(QR) - QR\cos(QR))]\}^2 \end{aligned} \tag{5.1}$$

where and $V_\varepsilon = 4\pi(\Delta\varepsilon_{cs}R_c^3 + \Delta\varepsilon_{ss}R^3)/3$ and $\Delta\varepsilon_{cs} = \varepsilon_c - \varepsilon_s$ is the difference between the dielectric constants of the core and the shell while $\Delta\varepsilon_{ss} = \varepsilon_s - \varepsilon_{sol}$ is the difference between the shell and the solvent with the corresponding refractive indexes $n_i = \sqrt{\varepsilon_i}$ of the core, the shell and the solvent respectively. To account for the particles' polydispersity we applied a logarithmic normal distribution $p(R_c)$ of the core radii assuming a constant shell thickness $d_{shell} = R - R_c$. With this the model function used for the fitting is

$$R(Q) = \frac{k_I^4}{16\pi^2}\phi \int_0^\infty p(R_c)V_p \left|\frac{\bar{\varepsilon} - \varepsilon_{sol}}{\varepsilon_{sol}}\right|^2 P(Q)dR_c \tag{5.2}$$

with the wave vector of the incident beam, $k_I = 2\pi n_S/\lambda_0$, and the particles' average dielectric constant $\bar{\varepsilon} = (R_c^3\Delta\varepsilon_{cs} - R^3\varepsilon_s)/R^3$. The lines in Fig. 5.6 were obtained by simultaneously fitting the three sets of data with eq. 5.2, where the global parameters R_c, R, σ_r were forced to be the same for all three sets of data, while the local parameters n_c and n_s were allowed to vary between the data sets. The resulting best fitting parameter values are collected in Table 5.1. The geometrical parameters are in very good agreement with the information deduced from

cryo-TEM. Further we find $n_c \approx 1.38$ which is qualitatively in agreement the reported refractive index values for pure FBMA particles $n_{FBMA} \approx 1.37$ [69]. The parameters associated with the particle shell are well in line with the picture of a thin PEG layer, which is swollen by the solvent. The molar mass of the PEG chain corresponds to an average degree of polymerization of $N \approx 22$, yielding an all-trans contour length of the chain $l_c \approx 8$ nm and a radius of gyration $R_g \approx 0.8$ nm if a length of about 0.13 nm per backbone atom [78, 79] is and a monomer segment length of approximately 0.38 nm is assumed . This implies that a shell consisting of PEG should have a thickness between approximately 1.5 nm and 8 nm in accordance with our findings from SLS $\langle R \rangle - \langle R_c \rangle = 5.9$ nm. Assuming an ideal mixture, we can obtain an estimate for PEG the volume fraction in the shell as $\phi_{PEG} = (n_s - n_{sol})/(n_{PEG} - n_{sol})$. Applying $n_{PEG} \approx 1.358$ [80] this yields a polymer volume fraction of about 20% in both solvents. These findings strongly indicate that our particles exhibit a pronounced core shell structure with a significant enrichment of the PEG chains at the surface of an FBMA core, which was not reported before.

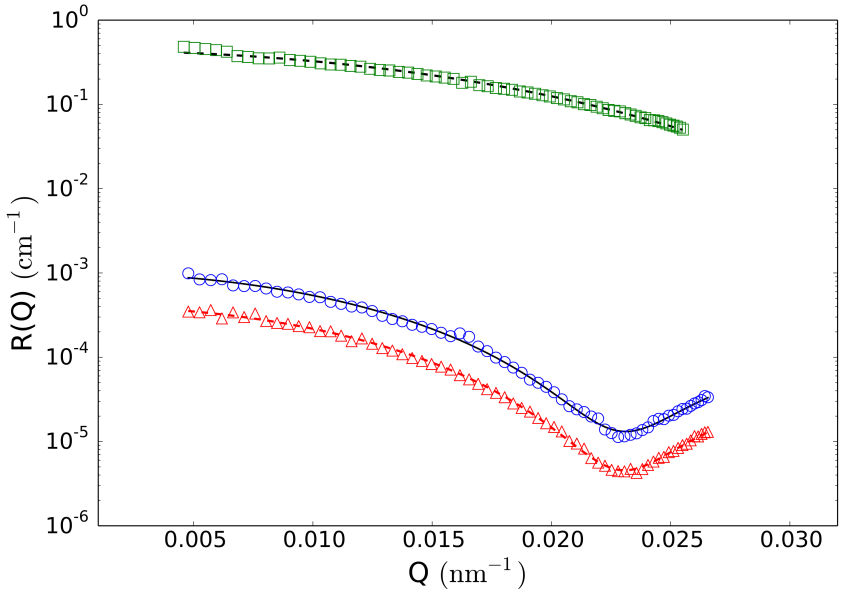

Figure 5.6: *Static light scattering data at low volume fractions. Open squares: $\phi = 5.6 \times 10^{-3}$ in water, open circles: $\phi = 1.4 \times 10^{-3}$ in DMSO/water, open triangles: $\phi = 5.6 \times 10^{-3}$ in DMSO/water, lines: best fits to data with eq. 5.2 resulting the parameters listed in Table 5.1.*

Generally, with increasing volume fraction of the particle suspension, a transition from an isotropic solution to a colloidal crystal is expected. Indeed, FBMA-particle suspensions with volume fractions $\phi > 10\%$ are opalescent, indicating the formation of an ordered structure.

With lower volume fractions this color full effect vanishes gradually and the determination of the transition volume fraction by optical inspection is rather ambiguous. Therefore we applied the Hansen-Verlet criterion to estimate the lowest volume fraction at which coexistence between an isotropic solution and an ordered structure occurs. According to this empirical rule, it is generally accepted that the maximum of the structure factor $S(Q_{max}) = 2.85$ at the freezing point of colloidal hard sphere suspensions [81], while it slightly increases for particles interacting by electrostatic repulsion (ER), depending weakly on their surface charge density and the solvent salinity. For charged particles at low salinity, as in our case the threshold value is $S(Q_{max}) \approx 3.0 - 3.1$ [82–85] In Fig. 5.7 we plotted the structure factors of suspensions with different volume fractions, obtained from the static scatting data according to

$$S(Q) \approx \frac{I(Q,\phi)}{I(Q,\phi_0)} \frac{\phi_0}{\phi} \tag{5.3}$$

where $I(Q,\phi_0)$ was measured at $\phi_0 = 1.4 \times 10^{-2}$ at which the structure factor is unity at all Q to a very good approximation.

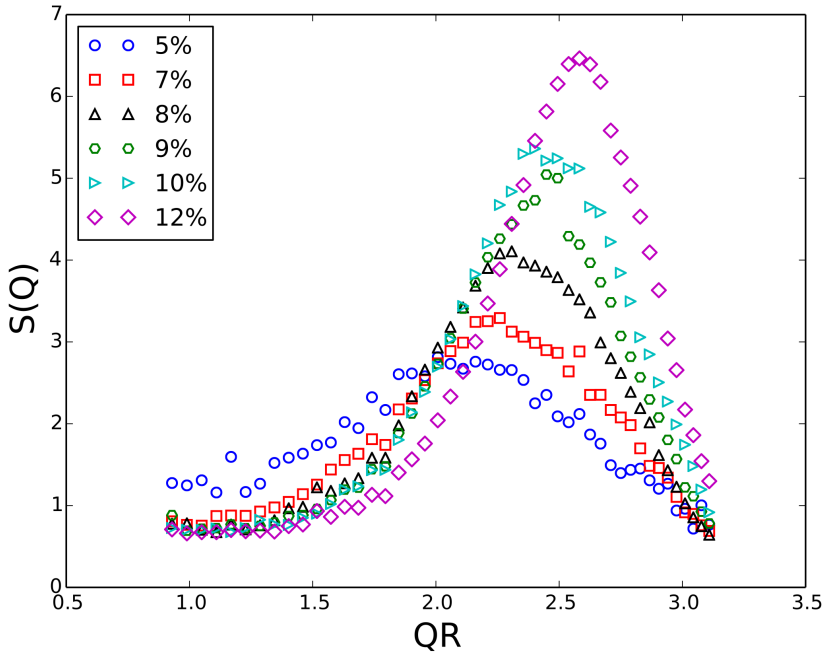

Figure 5.7: *Structure factors obtained from PEGylated FBMA particle suspensions in index-matching DMSO/water mixtures with different volume fractions as indicated in the legend and a screening length of $l_D \approx 95nm$.*

At the given salinity $S(Q_{max}) \lesssim 3$ for the sample with $\phi = 0.07$, while the structure factor maximum is significantly larger than the threshold value for the sample with 8% volume fraction. Thus, at $\phi = 0.08$ there is definitely a coexistence between an isotropic solution and an ordered structure.

5.3.1.4 Dynamic light scattering

Before conducting experiment on near-wall dynamics, it is important to check if and how the index-matching solvent influences the diffusion behavior of the system in bulk other than by viscous friction. For this purpose, we performed dynamic light scattering experiments on dilute particle dispersions both in water and in the index-matching DMSO/water mixture. Fig.5.8 shows a plot of the first cumulant Γ_1 vs Q^2 for particles dispersed in pure water and in the mixed solvent, respectively. The diffusion coefficient of the particles is the slope of the observed linear relations, $D_0 = 1630$ nm^2/ms in water and 746 nm^2/ms in the mixed solvent. The hydrodynamic radius, calculated through the Stokes-Einstein relation is $R_H = 131$ nm in both cases, when the correct values for the solvent viscosity are used, i. e. $\eta = 1$ mPas for water and 2.187 mPas for the mixed solvent. This shows that the solvent exchange has no effect on the particles' bulk dynamic except for the increased viscous friction.
Moreover, the linearity of Γ versus Q^2 plots in both cases is a first hint to a narrow particle size distribution indicating the absence of aggregates in the dispersions. A more thorough estimate of the particle size distribution can be obtained from a cumulant analysis of the correlation functions. The polydispersity index is given by

$$\mathrm{PDI} = \mu_2 / \langle \Gamma \rangle^2$$

where μ_2 is the second cumulant. We find PDI=0.03 for the particles in pure water and 0.09 in the solvent mixture. Assuming a logarithmic normal distribution of the particle radii these figures correspond to a relative standard deviation $\sigma_r \approx 0.05$ in the first case, which is in perfect agreement with the observed standard deviation from Cryo-TEM. The relative standard deviation measured in the index-matching solvent mixture is 0.1 again showing there is no significant aggregation of particles in this case.
The hydrodynamic radius obtained from DLS is larger than the geometric radius obtained from Cryo-TEM, which is $R = 120$ nm. This is explained by the fact that the two methods measure different moments of the size distribution. For a logarithmic normal distribution the ratio of both quantities is related to the standard deviation by $R_H/R = (1+\sigma^2)^5$ which for the present system implies a relative standard deviation of the order of ten percent in good

agreement with the values from the cumulant analysis of DLS data.

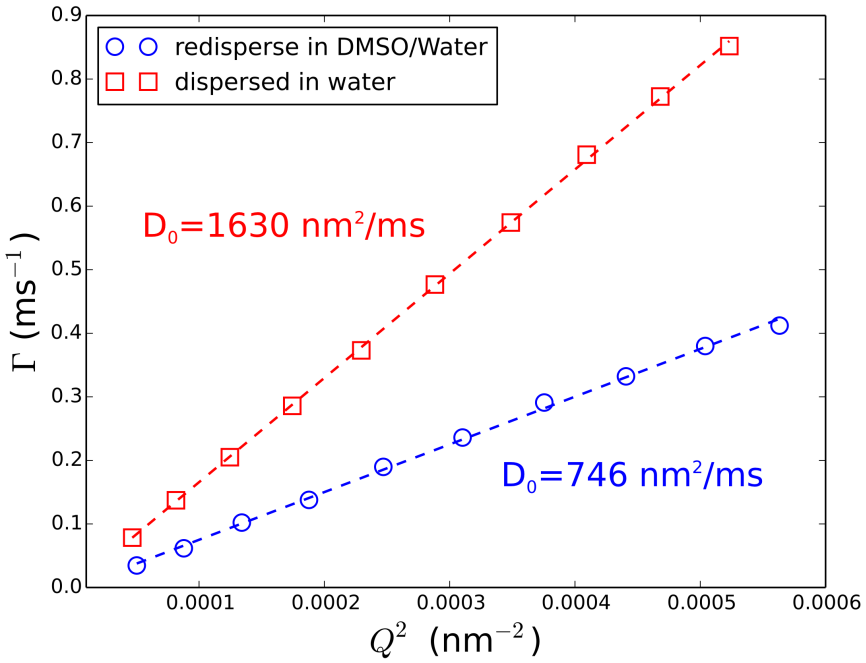

Figure 5.8: *Bulk DLS result of PEGylated FBMA particles dispersed in water(open red squares) and in DMSO/water mixture(open blue circles). Symbols represent experimental data and lines are linear least squares fits with slopes equal to the diffusion coefficients, D_0, as indicated.*

5.3.2 EWDLS measurements

5.3.2.1 Correlation function

To investigate the PEGylated FBMA particles near-wall dynamics at low volume fractions, we performed EWDLS measurements on suspensions with $\phi = 0.01$. Fig. 5.9 present the measured intensity correlation functions during a parallel scan (top graph), and the corresponding field correlation functions (bottom graph) normalized through generalized Sigert relation 3.1. The intensity correlation function shows a smooth base line, which indicates a good data quality. After normalization, we can clearly see that, as scattering vector increases, the relaxation time decreases and relaxation rate gets higher, which is similar to the case of bulk light scattering.

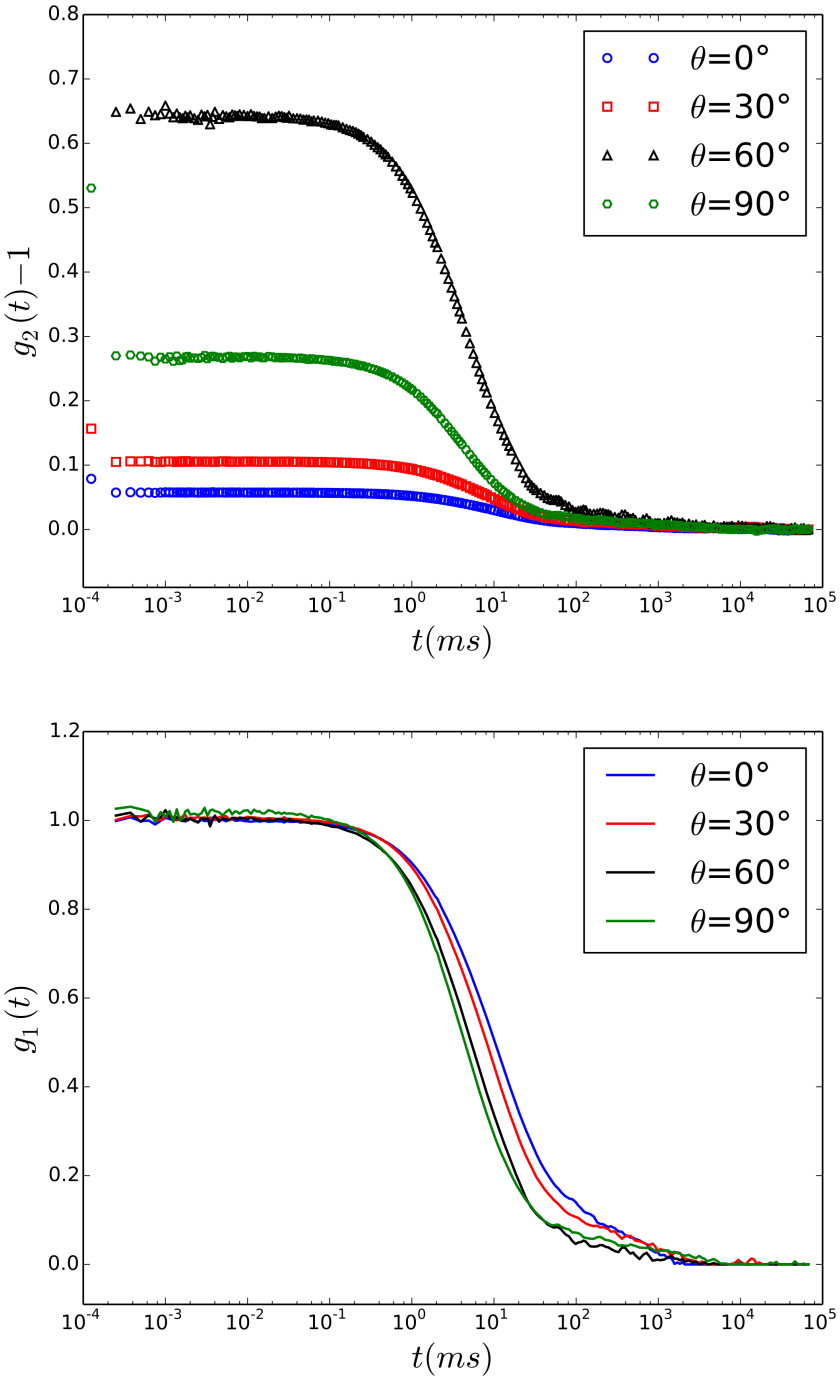

Figure 5.9: *Intensity correlation functions (top) and field correlation functions (bottom) obtained from parallel scan PEGylated FBMA particles.*

5.3.2.2 Influence of ionic strength

As the colloids and the glass surface are negatively charged, addition of electrolyte will make a difference to the particles' near-wall dynamics, by changing the range of the electrostatic repulsion (ER). To illustrate this influence, Fig.5.10 shows values of Γ plotted versus the square of scattering vector component at two different salt concentrations. The top graph shows the parallel scan and the bottom shows the normal scan. Here and in the following we show normalized quantities, where $d = 2R_H$ is the particle diameter, to facilitate comparison between the results obtained from different systems, in particular with a hard sphere system as shown in Fig. 5.13 The red symbols represent a sample with 10 mM NaCl, which corresponds to a Debye length of $l_D = 3$ nm. In this situation the electrostatic repulsion (ER) is almost completely screened and the measured Γ agree within experimental error with the prediction for a hard sphere with a hydrodynamic radius of $R_H = 130$nm, which is represented by the black line in Fig.5.10. The error bars assigned to these data, which represent the standard deviation of three repeated measurements, are representative for all EWDLS data discussed in the following. For the sake of clarity we will not display error bars in the following graphs.
The blue symbol were obtained from the sample without extra salt addition, which corresponds to an ionic strength $\sim 10^{-5}$M and a Debye length of l_D=95 nm. In this suspension, the particles move significantly faster than those dispersed at high salt concentration. This can be explained intuitively, since the long range electrostatic repulsion (ER) will effectively push the particles away from the interface thereby reducing the hydrodynamic wall drag effect. To quantitatively analyze these data, we calculated the Γ vs $Q_{\|}^2$ dependence, by numerically integrating eq. 2.48 into which we introduced the electrostatic interaction potential which may be approximated within the Debye-Hückel-Derjaguin limit by

$$V_{ER}(z) = B_{ER} \exp\{-(z-R)/l_D\} \tag{5.4}$$

The amplitude B_{ER} scales with particle radius and depends on the surface charge density of particles and the wall. In the model calculations, this amplitude is the only adjustable parameter and we could achieve good agreement between all experimental data discussed in this chapter and the predictions wit a fixed value of $B_{ER} = 2k_BT$. The experimental and calculation parameters are listed in the graphs.
The systematic deviation of the experimental data at high $Q_{\|}$, is due to the fact that the primary laser beam is back-reflected back upon exit of the semi-spherical lens, by that giving rise to a second scattering event with an in-plane angle $\theta_r = 180 - \theta$. This effect is frequently

observed, even in bulk experiments, with index matched particles. For the case of EWDLS on hard sphere samples it has been discussed in detail in chapter 4. As a consequence of this back reflection, data obtained from EWDLS experiments at $\theta > 90$ are often not reliable, which in the present case corresponds to $(Q_{\|}d)^2 \gtrsim 30$, given $\alpha_r = 60^\circ$ and the refractive index of the solution $n_S \approx 1.38$.

The agreement between experiment and the predictions is less satisfying in the case of the $Q_\perp$-scans, as shown in Fig. 5.10 (bottom graph), since the scatter of the experimental data is significantly larger, especially at large Debye length. At high salt concentration the experimental data are reasonably well represented by the prediction for a Debye length of 3nm, while the experimental data obtained from the sample without additional salt follow the prediction only qualitatively.

5.3.2.3 Influence of penetration depth

To investigate the influence of the evanescent wave penetration depth on the measured values of Γ we performed experiments at different angles of incidence. The top part of Fig. 5.11 shows data obtained from $Q_{\|}$-scans at two different penetration depths together with the corresponding theoretical prediction. Although the agreement is very good, the scatter of the experimental data is larger than the difference between the predictions for different penetration depths. In the bottom part of the figure we show results from $Q_\perp$ scans at different penetration depths. Although here, the expected difference is larger here than for the $Q_{\|}$ scans, the experimental scatter is even larger, due to the generally poor quality of $Q_\perp$ scan data. We observe the same behavior also at a volume fraction of 5% as is shown in Fig. 5.12. Therefore we conclude that in general the influence of the penetration depth is too small to be reliably detected experimentally.

5.3.2.4 Near-wall dynamics close to isotropic-ordered transition

So far, we have shown that in dilute suspensions, PEGylated FBMA particles behave like charged spheres, and their near-wall dynamics can be suitably described by a combination of hydrodynamic wall effect and the particles' static interaction with the wall. However, a more interesting and challenging question concerns the near-wall dynamics at increased volume fractions, at which the system changes from an isotropic solution to an ordered structure, stabilized by long-ranged particle interactions. As a first step to tackle this question we show data obtained from a suspension with a particle volume fraction of 7% in Fig. 5.13. The graph displays the normalized Γ versus $Q_{\|}^2$ data, obtained at κR=1.81 from a suspension without

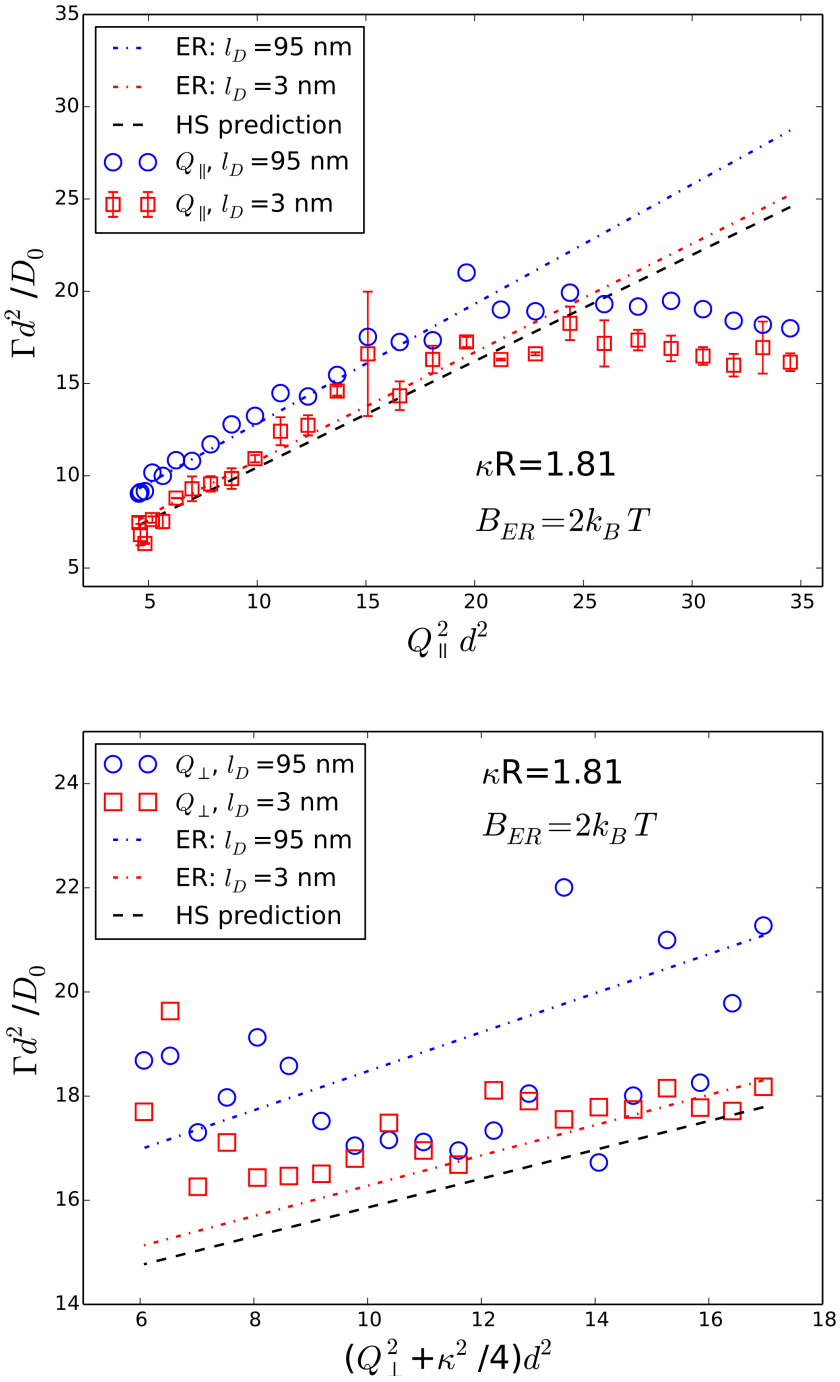

Figure 5.10: *Normalized initial relaxation rates* Γ *as a function of the parallel scattering vector component squared (top graph) and normal vector component squared (bottom graph). Symbols represent experimental data obtained from a* $\phi = 0.01$ *sample at different Debye screening lengths, as indicated in the legend. Blue and red lines represent theoretical predictions for infinite dilution according to eqs. 2.48 and 5.4. Black line shows hard sphere prediction. Error bars are assigned to the data obtained from* $Q_\parallel$ *scan for the sample with* l_D*=3 nm, and represent standard deviations from three repeated measurements.*

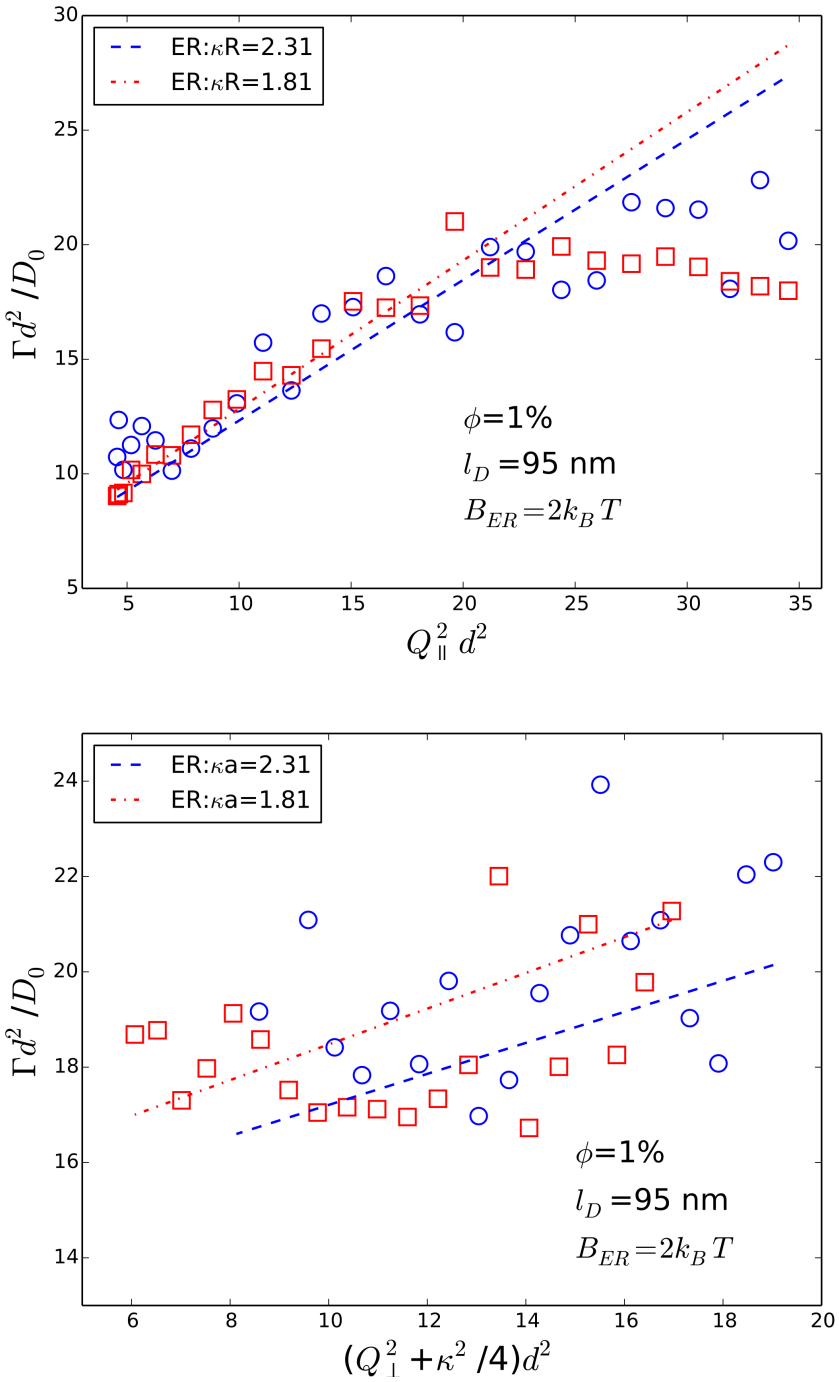

Figure 5.11: *Effect of evanescent wave penetration depth on measured* Γ*. Symbols represent experimental data obtained from a* $\phi = 1\%$ *sample at different penetration depths and lines of equal color represent theoretical predictions for infinite dilution according to eqs. 2.48 and 5.4. Penetration depths are indicated in the legend. Top graph is for a parallel scan and bottom graph is for normal scan.*

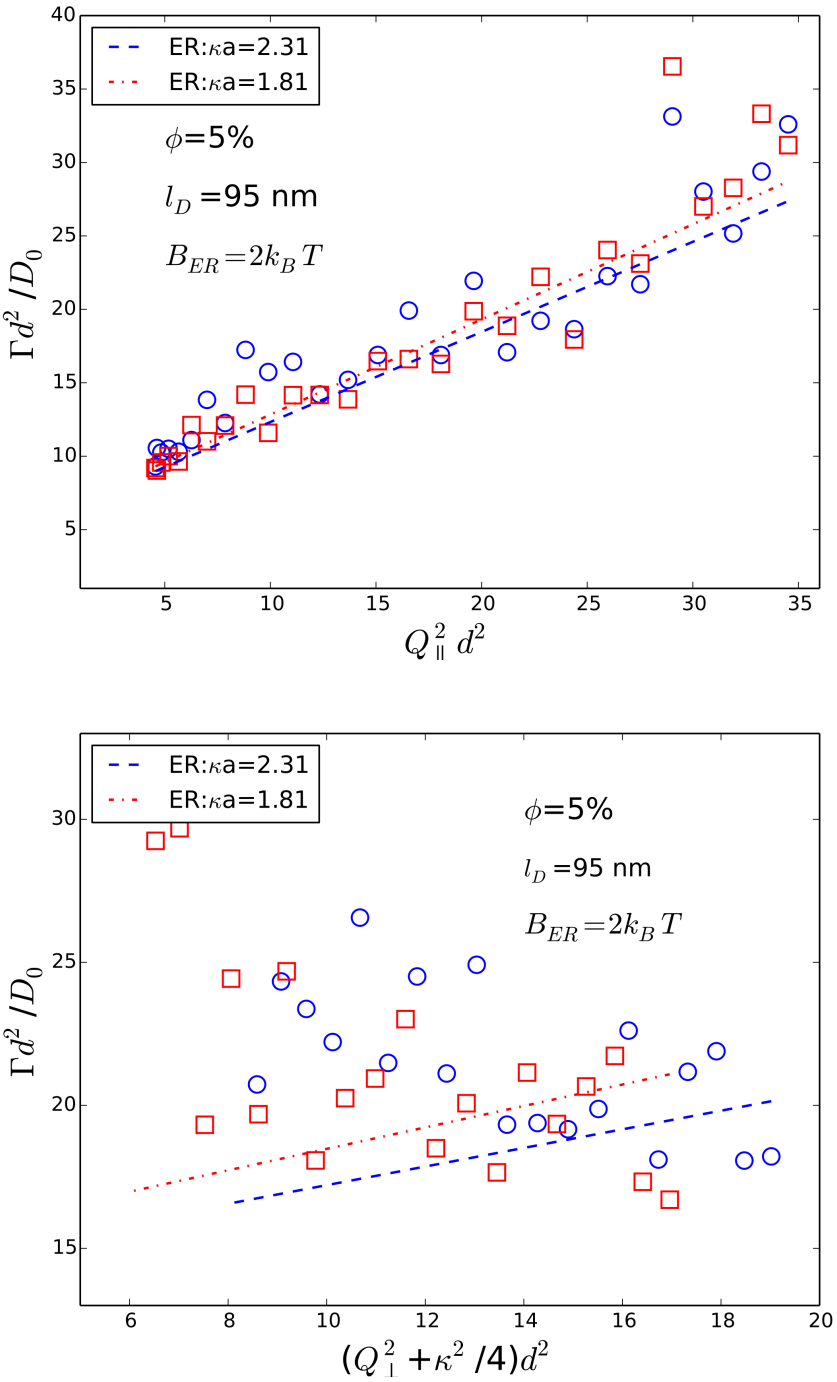

Figure 5.12: *Effect of evanescent wave penetration depth on measured* Γ*. Symbols represent experimental data obtained from a* $\phi = 5\%$ *sample at different penetration depths and lines of equal color represent theoretical predictions for infinite dilution according to eqs. 2.48 and 5.4. Penetration depths are indicated in the legend. Top graph is for a parallel scan and bottom graph is for normal scan.*

added salt. As a general trend we observe that the relaxation rates are lager at $\phi = 0.07$ than at infinite dilution, which is represented by the dashed dotted line. Further, there is a significant deviation from the linear $Q_{||}^2$ behavior, which was observed at low volume fraction. The relaxation rates rather undulate with $Q_{||}^2$ which is very reminiscent of the behavior we reported earlier for hard spheres at high volume fractions. For comparison we also show experimental data obtained from a suspension of hard spheres at a volume fraction of 30% together with a set of simulated data for the same system. Note that these data were obtained at $\alpha_r = 27.8^\circ$ and $n_S \approx 1.49$, thus the effect of back reflections will only become visible at $(Q_{\|}d)^2 \gtrsim 50$. Based on the observed qualitative similarity we conjecture that also the near-wall dynamics of the PEGylated FBMA particles at $\phi = 0.07$ are significantly affected by the suspension's structure factor, which is in line with our observation that suspensions with a volume fraction of 7% are close to the disorder/order coexistence of the system. A systematic experimental investigation and a quantitative theoretical analysis of this effect will be the subject of a future contribution.

5.3.2.5 Comparison with bulk DLS

It is shown in Chapter 4 that, at high particle volume fraction, the self diffusion coefficient of hard sphere particles is approaching the bulk value, due to the screening of the particles' hydrodynamic interaction with the wall. Further, in the previous section we show that close to the isotropic-ordered transition volume fraction ϕ=7%, FBMA particles show a near-wall dynamic behavior reminiscent of a hard sphere system at higher volume fraction ϕ=30%. We will therefore in this section contrast the near-wall dynamics to the bulk dynamics of FBMA particles at different volume fractions. For this purpose, we compare EWDLS data from $Q_{\|}$ scans to the bulk data obtained at the same volume fraction. We plot normalized relaxation rates from EWDLS versus the total scattering vector squared $Q^2 = Q_{||}^2 + Q_{\perp}^2$, instead of the parallel component $Q_{||}^2$ only, to make the near-wall data comparable to the bulk data. Note that in this representation the linear dependence of the EWDLS relaxation rates on Q^2 obtained at low volume fractions appear to have negative intersect as $Q \to 0$. This an artifact of presenting EWDLS data in dependence of the total scattering vector square. As

$$\begin{aligned}
\Gamma(Q^2) &= \langle D_{\|} \rangle_\kappa Q_{\|}^2 + \langle D_{\perp} \rangle_\kappa \left(Q_{\perp}^2 + \frac{\kappa^2}{4} \right) \\
&= \langle D_{\|} \rangle_\kappa \left(Q^2 - Q_{\perp}^2 \right) + \langle D_{\perp} \rangle_\kappa \left(Q^2 - Q_{\|}^2 + \frac{\kappa^2}{4} \right) \\
&= Q^2 \left(\langle D_{\|} \rangle_\kappa + \langle D_{\perp} \rangle_\kappa \right) - \left[\langle D_{\|} \rangle_\kappa Q_{\perp}^2 + \langle D_{\perp} \rangle_\kappa \left(Q_{\|}^2 - \frac{\kappa^2}{4} \right) \right]
\end{aligned} \tag{5.5}$$

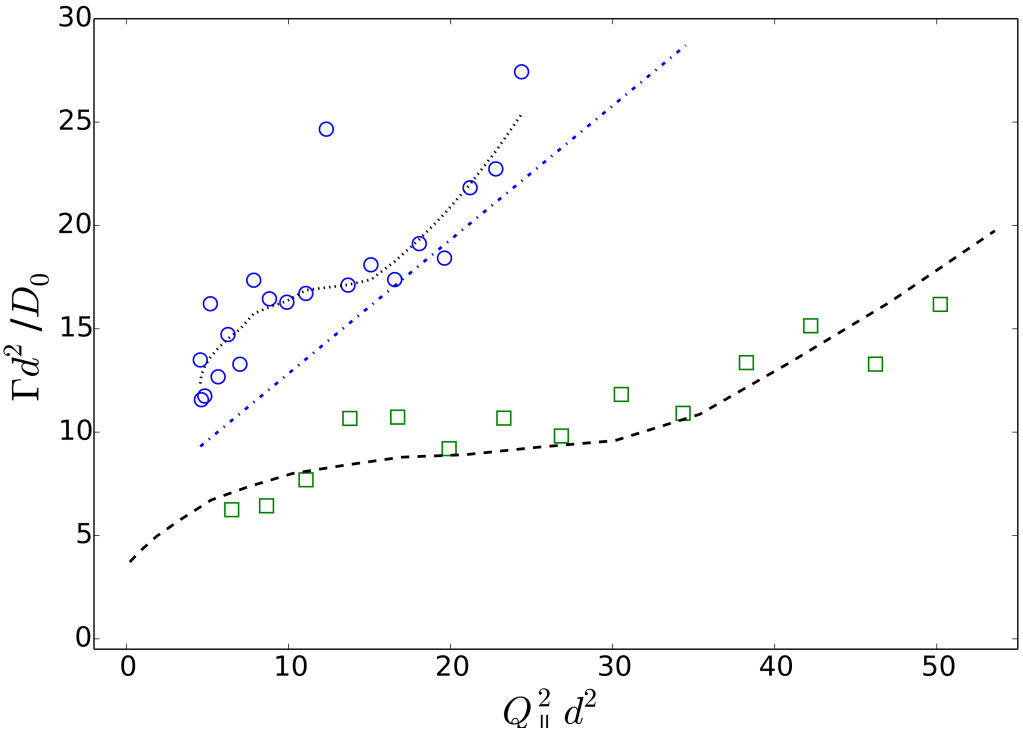

Figure 5.13: *Comparison of $Q_{\parallel}$-scans on a PEGylated FBMA suspension with $\phi = 0.07$ (open circles) and a hard sphere system at $\phi = 0.3$ (open squares). The dashed line represents simulation data for the hard sphere system, the dashed dotted line is the prediction for charged spheres at low ϕ according to eqs. 2.48 and 5.4 and the dotted line is a guide for the eyes.*

a linear extrapolation of Γ versus Q^2 will yield a negative intersect. This is however not a physical reality, since in a $Q_{\parallel}$ parallel scan $Q_{\perp}$ is fixed to a constant value, and therefore the range of the total scattering vector is limited to $Q^2 \geq Q_{\perp}^2$.

Fig.5.14, Fig.5.15 and Fig.5.16 show the experimental data of bulk and near-wall dynamics for PEGylated particles at three typical volume fractions, i. e. 1% , 5% , and 7%, where the isotropic-ordered transition is about to happen. The relaxation rates Γ and the scattering vector, for both bulk and near-wall measurements have been normalized with regard to diffusion coefficient D_0 and particle diameter d.

At the lowest volume fraction, the relaxation rates in bulk are by a factor of more then two larger than the values from EWDLS, which are quantitatively described by the low density prediction for charged spheres as discussed in section 5.3.2.2. The same prediction also describes the EWDLS data obtained at $\phi = 0.05$ correctly within experimental scatter. However, in this case the bulk data are only by a factor of ~ 1.5 larger than the EWDLS-data. At high volume fraction of 7%, the experimental EWDLS data are significantly different from the low density prediction, and largely overlapping with the bulk dynamic data throughout the entire accessible range of scattering vectors.

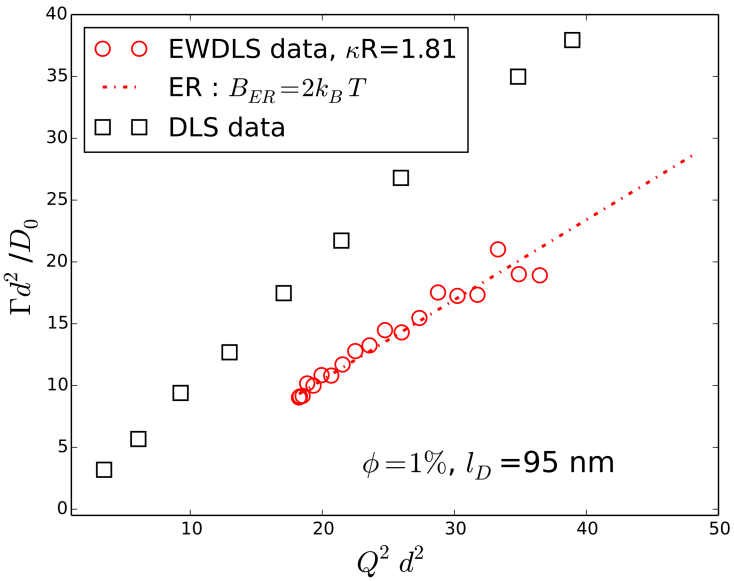

Figure 5.14: *Comparison of near-wall and bulk dynamics of PEGylated FBMA particles at $\phi = 1\%$. EWDLS data points obtained at $\theta < 90°$, which are affected by the back reflection effect are omitted for clarity.*

Thus, differently from the case of hard spheres, not only the near-wall self diffusion but the

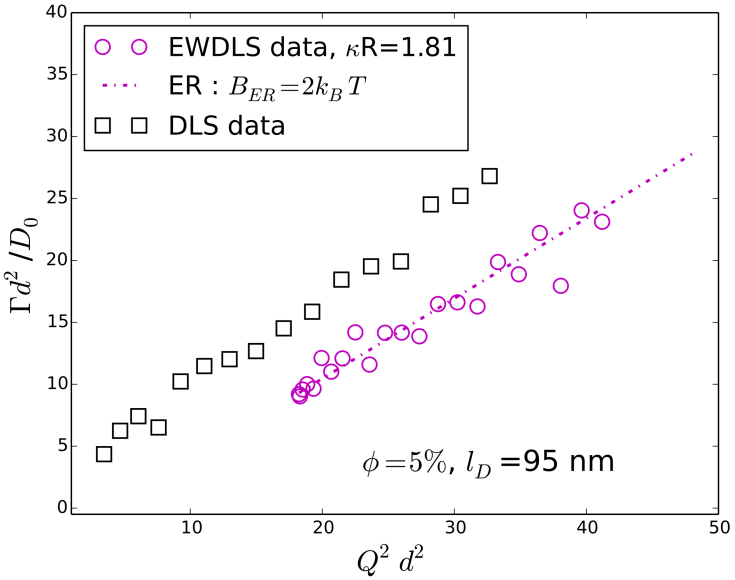

Figure 5.15: *Comparison of near-wall and bulk dynamics of PEGylated FBMA particles at $\phi = 5\%$. EWDLS data points obtained at $\theta < 90^\circ$, which are affected by the back reflection effect are omitted for clarity.*

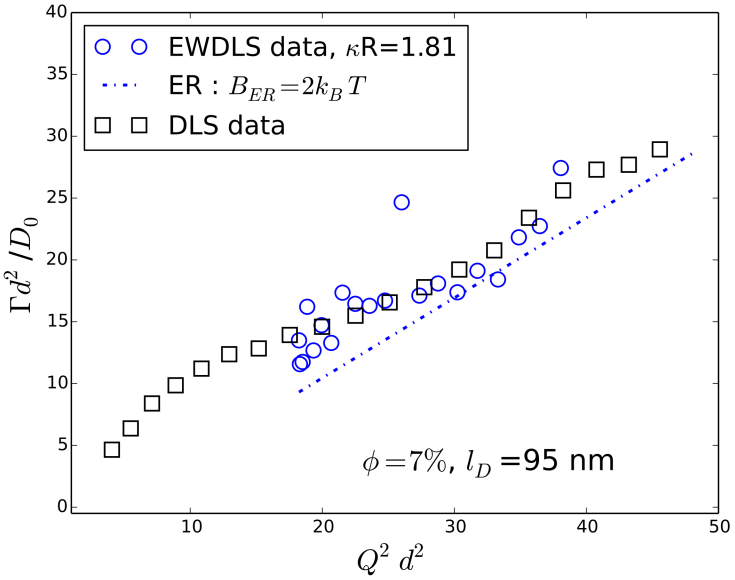

Figure 5.16: *Comparison of near-wall and bulk dynamics of PEGylated FBMA particles at $\phi = 7\%$. EWDLS data points obtained at $\theta < 90^\circ$, which are affected by the back reflection effect are omitted for clarity.*

general near-wall dynamics of charged approach bulk behavior at volume fractions close to the isotropic to ordered phase transition. In the context of hard sphere dynamics it was suggested that at high volume fractions, the particles located close to the wall are screening the walls' hydrodynamic interaction with the particles farther away, leading to the observed approach of the near-wall self diffusion coefficient towards the bulk value [24]. On the other hand, as can be seen from Fig. 4.6 in chapter 4 this screening effect is almost negligible for hard spheres at volume fractions below 10%. Therefore, it is questionable, whether the fact that the bulk and near-wall data from the FBMA sample at $\phi = 0.07$ fall on top of each other can be assigned to the screening of the hydrodynamic interaction with the wall. One might speculate that this is a generic feature of the vicinity to the phase transition, however since we do not yet have a sound theoretical description of charged spheres' near-wall dynamics available, we refrain from further interpretation of this observation.

5.4 Conclusion

In this chapter, we have synthesized PEGylated fluorinated particles by an emulsion polymerization, for the study of near-wall dynamics of colloidal particles in aqueous solution. Bulk characterizations show that the particles have a core shell structure, a negligible polydispersity, are stable against compression and addition of salt, and can be easily index-matched to aqueous solutions, which makes them a good model system for scattering experiments in aqueous suspensions at increased concentrations up to the transition from an isotropic solution to an ordered phase and beyond. By static light scattering we have shown that a coexistence of isotropic and ordered suspensions already occurs at a volume fraction of 8% in DMSO/water, if no additional electrolyte is present. In future we will use this system for the systematic investigation of near-wall dynamics of particles with long-ranging interactions. In this contribution we showed that EWLDS measurements on this system produce reliable and reproducible data. At low volume fractions the near-wall dynamics can be well predicted taking into account of the particles hydrodynamic and electrostatic interaction with the wall. However, even at moderate volume fractions the near-wall dynamics are reminiscent of the behavior which was observed for hard spheres at much higher volume fractions, which is attributed to the long range particle-particle repulsion. A thorough experimental investigation of the interaction effects on near-wall dynamics and the design of a theoretical framework for their prediction is the objective of ongoing work.

6

Scattering studies on polyurethane pre–polymer suspensions

In this chapter, the property, structure and dynamics, both bulk and near-wall, of polyurethane pre-polymer dispersions are extensively studied. Such colloids serve as a precursor for water-borne coating application. For the first time, EWDLS is applied to an industrial colloidal system.

6.1 Introduction

Polyurethane is a versatile material, which is widely used in coating and adhesives, electronics, building and construction, and automotive industry. [86–90] Waterborne polyurethane (WPU), with water as dispersion medium, provides an environment-friendly alternative to the traditional solvent-borne polyurethane materials. [91–93] One of the most common method to make aqueous polyurethane dispersion is the pre-polymer mixing process, which consists of three stages [94]: first, formation of isocyanate (NCO)-terminated pre-polymer by reaction of isophorone diisocyanates (IPDI) , polyol and a dihydroxy acid, such as dimethylolpropanic acid (DMPA), which introduces carboxylic functionality into the backbone of pre-polymer; second, neutralization of carboxylic group by teriary amine such as triethylamine (TEA), to produce ionic centers for particle formation; finally, chain extension for higher molecular weight and crosslink density.

The chem-physical properties of pre-polymers play a central role in the formation of polyurethane dispersion. In general, they are random co-oligomers made of three units, IPDI, polyol and DMPA, and the ratio of these building units can be varied. Duo to the amphiphilic molecular structure, such pre-polymers are expected to self- and co-assembled into colloidal particles in aqueous solution. [95] The nature, size and stability of these pre-polymer particles

will influence the property of subsequent chain extended PU dispersion and eventually the performance of WPU products.

Despite the high industrial relevance, few systematic studies have been conducted on the structure, property and dynamics of polyurethane pre-polymer dispersions. A recent theoretical study by F. Li *et al.* [96] showed that PU pre-polymers in aqueous solution self-assembly into spherical micelles and the stability of the micelles decreases with increasing ionic strength. An experimental inquest into this theoretical finding is necessary, and will be the starting point of this chapter. We first present the experimental results of self,co-organization behavior of the amphiphilic pre-polymers in water, by light scattering and small angle X-ray scattering, tuning both pre-polymer concentration and ionic strength. In the next step, we use the amphiphilic pre-polymer as surfactant agent to encapsulate the hydrophobic pre-polymer and study the size, shape and stability of the encapsulated particles. Two different amphiphilic pre-polymers are investigated here: random pre-polymer, synthesized through one-pot reaction, with mixed unit sequence; "micropure" pre-polymer with well defined structure and specific sequence, synthesized in the lab. Finally, the near-wall dynamics of these encapsulates are studied by evanescent wave dynamic light scattering.

6.2 Material and sample preparation

It is necessary to point out that in this chapter, the focus is on the property and dynamics of dispersions. Chain extension of polyurethane pre-polymers will not be included here. Pre-polymers have a typical molecular weight around 3000 g/mol and are made of three building units, as shown in Fig 6.1.

Three kinds of polyurethane pre-polymers were used in the experiments: amphiphilic random 228, hydrophobic random 229 and the amphiphilic Micropure . Pre-polymer 228 and 229, which have random unit sequence, are synthesized and provided by DSM Resins, Waalwijk. Samples are stored in acetone solution with a solid content of 80.6%. Pre-polymer 228 has a DMPA content of 8%, while 229 doesn't contain DMPA units.

Micropure is a pure substance consisting of oligomers with the same molecular structure, as shown in Fig 6.2. The DMPA content is 8%. Micropure pre-polymers are synthesized and provided by SyMO-Chem bv in Eindhoven. The sample comes in the form of solid, with no addition of acetone.

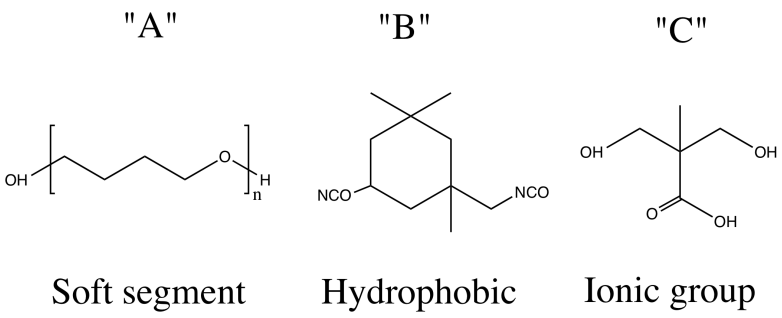

Figure 6.1: *Building blocks of polyurethane pre-polymer.*

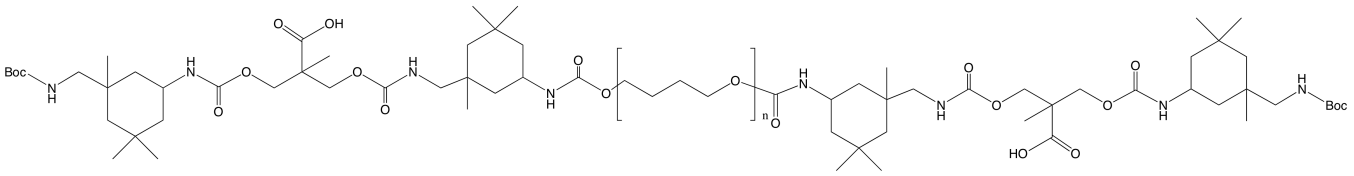

Figure 6.2: *Molecular structure of Micropure pre-polymer*

6.2.1 Preparation of dispersion

To prepare the colloidal dispersion of amphiphilic 228, a certain amount of acetone solution was preheated in a water bath at 60°C, to reduce viscosity and facilitate processing. TEA was added to neutralize DMPA groups, and the sample was stirred for 10 min. Water was then added to dilute the mixture. The sample was then shaken gently for 24 hours at room temperature and further diluted by water. The remaining acetone inside was removed by a rotary evaporator at 45°C. The remaining solution serves as stock solution, with a code name PP228.

To prepare colloidal dispersion with amphiphilic 228 encapsulating hydrophobic 229 encapsulated, a certain amount of 228 and 229 acetone solutions was weighted separately, mixed together and preheated in a water bath at 60°C. Then TEA was added to neutralize DMPA groups, and the sample was stirred for 10 min. Water was then added to dilute the mixture. The sample was then shaken gently for 24 hours at room temperature and further diluted by water. The remaining acetone inside was removed by a rotary evaporator at 45°C. The remaining solution serves as stock solution, with a code name 228-229.

To prepare colloidal dispersion of micropure encapsulated with 229, a certain amount of Micropure (in solid form) was weighed and dissolved in acetone. The obtained Micropure-acetone solution was mixed with a certain amount of 229 and preheated preheated in a water bath at 60°C. Then TEA was added to neutralize DMPA groups, and the sample was stirred for 10 min. Water was then added to dilute the mixture. The sample was then shaken gently for 24 hours at room temperature and further diluted by water. The remaining acetone inside was removed by a rotary evaporator at 45°C. The remaining solution serves as stock solution, with a code name MP-229.

The solid content of stock solutions were determined by drying a drop on an aluminum disk and weighing the wet-dry differences. From the stock solution, series of diluted samples with different concentrations and ionic strength were made.

In order to avoid confusion, a summary of three different kinds of colloidal dispersion was given here:

- PP228: self, co-organized colloidal particles from 228.
- 228-229: co-organized particles with amphiphilic 228 encapsulating hydrophobic 229.
- MP-229: Co-organized particles with amphiphilic Micropure encapsulating hydrophobic 229.

6.3 Self, co-organization of amphiphilic pre-polymers

It is known that amphiphilic polymers in selective solvents can self-assemble into various shapes, such as vesicles, rods, micelles [97–100]. If we consider PU as an amphiphile, with a hydrophilic carboxylic acid moiety as "head" and a hydrophobic isocynate moiety as "tail", we would expect them to pack densely into micelles in water. Fig 6.3 shows a time series of particle size and polydispersity of PP228 aggregates in dilute aqueous dispersion measured by a Malvern Zetasizer. From this simple measurement, we observe that amphiphilic pre-polymers self-,co-organize into relatively mono-disperse particles in water, with diameter around 20 nm, and the aggregates stay stable over time.

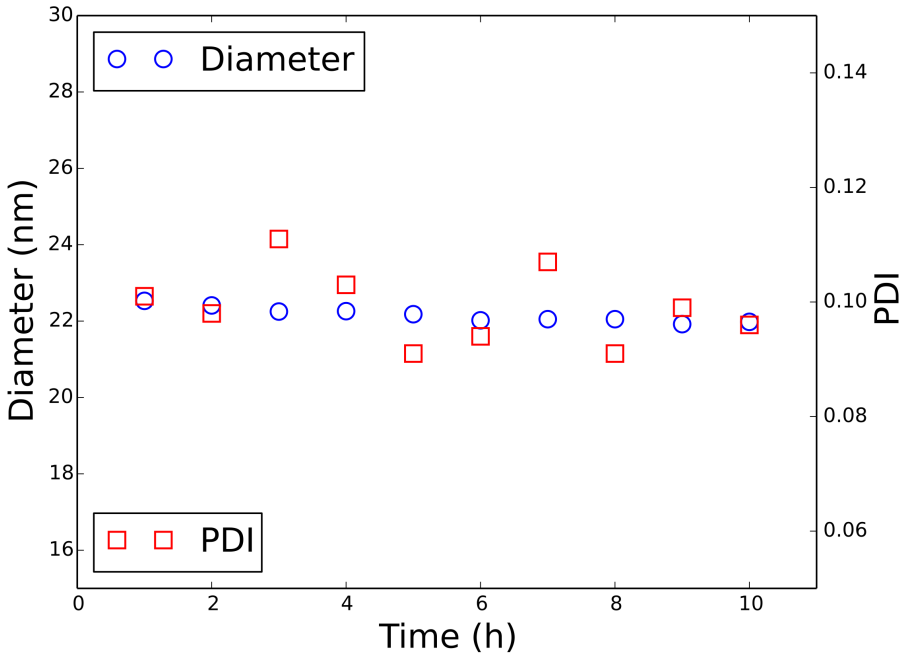

Figure 6.3: *Zeta sizer measurement on PP228 dispersion at 1 mg/mL concentration. Values of diameters and PDI are given by the build-in software.*

6.3.1 Static light scattering

The stability of amphiphilic charged copolymers is very sensitive towards pH and ionic strength of the solution [101]. In this section, we will probe the size, shape and stability with dependence on ionic strength of amphiphilic 228 aggregates. Firstly, static light scattering measurements were performed at four concentrations, 1 mg/mL, 2 mg/mL, 5 mg/mL

and 10 mg/mL, at seven different salt concentrations ranging from 0 mM to 100 mM. Fig 6.4 shows the Zimm-plot [102] of data from a PP228 particle dispersion at 1 mM NaCl concentration. According to eq. 2.17 the second viral coefficient A_2, and the molecular mass M_W are obtained are obtained from the linear extrapolation of the data versus concentration and versus Q^2 respectively. Corresponding plots were made and analyzed for all salt concentration and the resulting virial coefficients and molar masses are summarized in Table 6.1. The molecular mass of the aggregates is around $10^6 g/mol$ and it is slightly increasing with salt concentration. The second viral coefficient is fluctuating from 0 mM to 10 mM and undergoes a dramatic decrease at 50 mM NaCl. At 100 mM NaCl, the sign of A_2 becomes negative, which indicates that the particle interaction has changed from repulsive to attractive. This means that upon increasing ionic strength above 50 mM, PP228 particles experience a transition from repulsive to attractive interaction, i. e. the dispersions turn from stable at low salt concentrations to unstable at high ionic strength. This experimental finding agrees with the SCF calculation by Li *et al.* [96], which predicts that the micelles self-assembled by become unstable at ionic strength of 50 mM.

Table 6.1: *Summary of static light scattering results of PP228 aggregates*

$C_{NaCl}(mM)$	$A_2(mol*mL/g^2*10^{-3})$	$M_W(g/mol*10^6)$
0	1.110	1.1010
0.01	1.490	1.1465
0.1	1.220	1.1445
1	2.010	1.1480
10	1.167	1.7700
50	0.2300	1.6047
100	-0.0478	1.6480

6.3.2 Dynamic light scattering

Dynamic light scattering measurements are performed on diluted PP228 particle dispersion at different concentration and ionic strength. Relaxation rate Γ is obtained from a stretched exponential fitting of correlation function. The diffusion coefficient of the particles is determined from the slope of the observed linear relation of Γ vs. Q^2. The apparent hydrodynamic radius is then calculated through Stokes-Einstein relation from D_0. Table 6.2 lists the apparent hydrodynamic radius $R_{H,app}$ of PP228 particles, at different dispersion concentration and salt concentration. $R_{H,app}$ decreases with dispersion concentration. By extrapolating the concentration to zero, one could determine the hydrodynamic radius at infinite dilution, which

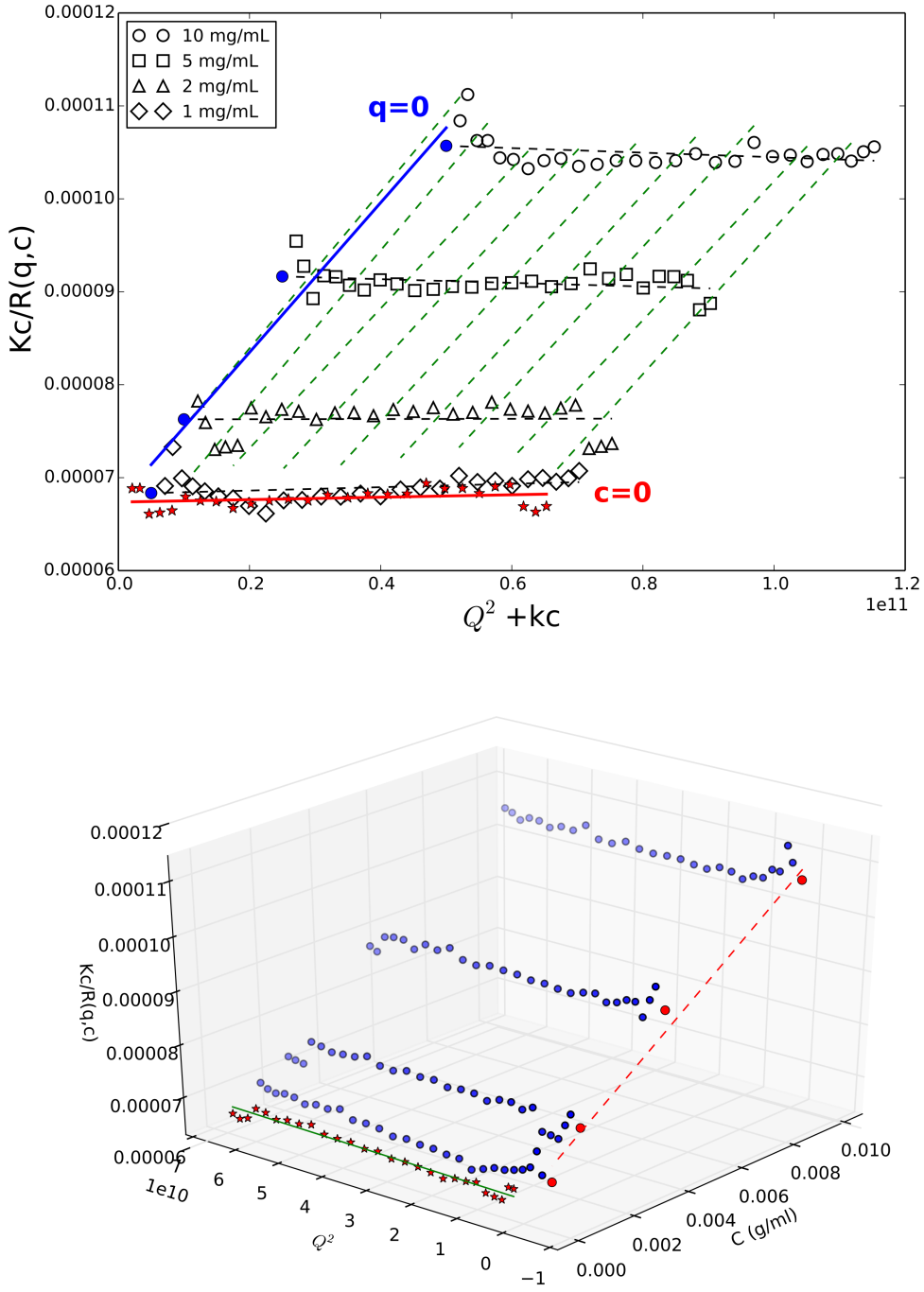

Figure 6.4: *Top: Zimm-plot of the scattering data from the polyurethane pre-polymer solution at 1 mM NaCl; Bottom: a 3D representation OF the Zimm-plot.*

decreases with salt concentration, up till 50 mM. At $c_{NaCl} = 100$mM, R_H increases again, which is also observed for the apparent values $R_{H,app}$ at all solute concentrations. The disruption of the trend indicates a change of the particle properties at high salt, which agrees with the result of SLS.

Table 6.2: *Summary of apparent hydrodynamic radius of PP228 particles at different dispersion concentration and salt concentration, measured by DLS*

	0 M	0.01mM	0.1 mM	1 mM	10 mM	50 mM	100 mM
0 mg	13.00	12.85	12.53	12.19	12.01	11.84	12.16
1 mg	13.01	12.77	12.58	12.12	11.89	11.84	12.25
2 mg	12.56	12.50	12.10	11.95	11.85	11.76	11.97
5 mg	11.85	11.79	11.59	11.58	11.68	11.73	11.75
10 mg	11.27	11.17	11.10	11.08	11.17	11.60	11.69

6.3.3 Small-angle X-ray measurement

As shown in the DLS study, the radius of PP particles is around 12 nm, which is too small for a reliable size determination by SLS. Therefore, Small Angle X-ray Scattering (SAXS) is employed to measure the radius of gyration R_g and the geometric radius R of the PP228 aggregates. Five salt concentrations are studied here. Fig 6.5 shows the scattered intensity dependence over Q (left) and a Guinier plot [103] of the initial part of the scattering curves (left). In the Guinier plot the curves are vertically displaced by an artificial factor for better visibility. Based on the assumption of a spherical particle shape, the location of first intensity minimum in the scattering curve gives the geometric radius of the PP228 particles by, $Q_{min}R = 4.49$. R is determined to be about 15 nm at all salt concentrations. The radius of gyration R_g is obtained by fitting the Guinier region of the scattering curve by the limiting expression

$$\lim_{QR_g<<1} ln[I(Q)] \sim exp(-R_g^2 Q^2/3) \tag{6.1}$$

as shown in Fig 6.5(right). The resulting values are listed in Table 6.3 together with the hydrodynamic radii determined by DLS, R_H, and the geometric radii R estimated from the first minimum in the scattering curve.

The radius of gyration and the molecular weight of the PP228 aggregates increase with salt concentration, while the hydrodynamic radius decreases. This indicates on the one hand

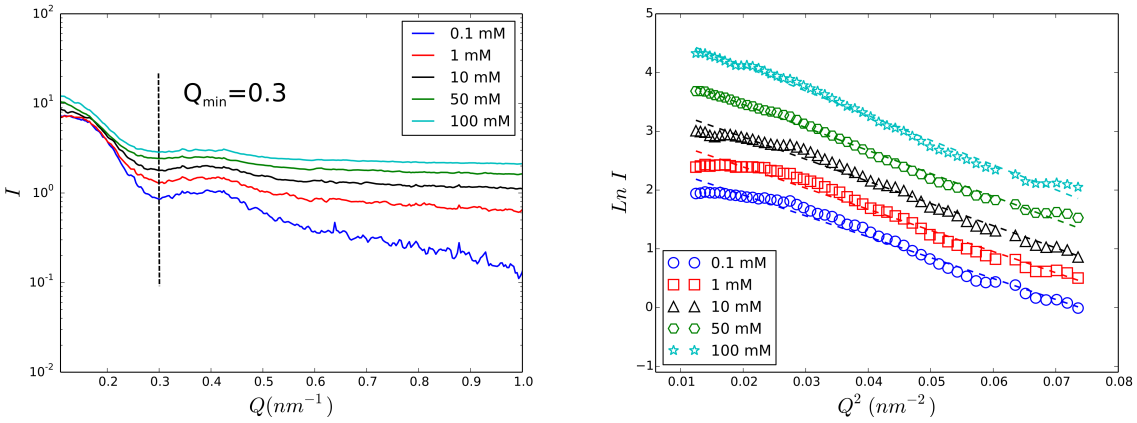

Figure 6.5: *SAXS measurements on five salt concentrations at 25°C. Left: Intensity vs. Q; right: Guinier plots*

Table 6.3: *Summary of R_g, R_H and R of PP*

$C_{NaCl}(mM)$	$R_g(nm)$	$R_H(nm)$	$R(nm)$	$\rho = R_g/R_H$
0.1	10.94	12.53	15	0.87/
1	11.25	12.19	15	0.92
10	11.76	12.01	15	0.98
50	11.97	11.84	15	1.01
100	12.30	12.16	15	1.01

that more and more chains aggregate into the colloidal particles as the ionic strength increases. On the other hand the ratio $\rho = R_g/R_H$ increases which implies a shape change of the aggregates [104, 105] from an almost perfectly spherical to a prolate object. As the salt concentration increases, the electrostatic interaction between the charged hydrophilic head groups are screened, which reduces the effective area per head group and by that the preferred curvature of the particles' surface [78], which supports the observation that the aggregates appear to adopt a prolate shape at high salt concentration.

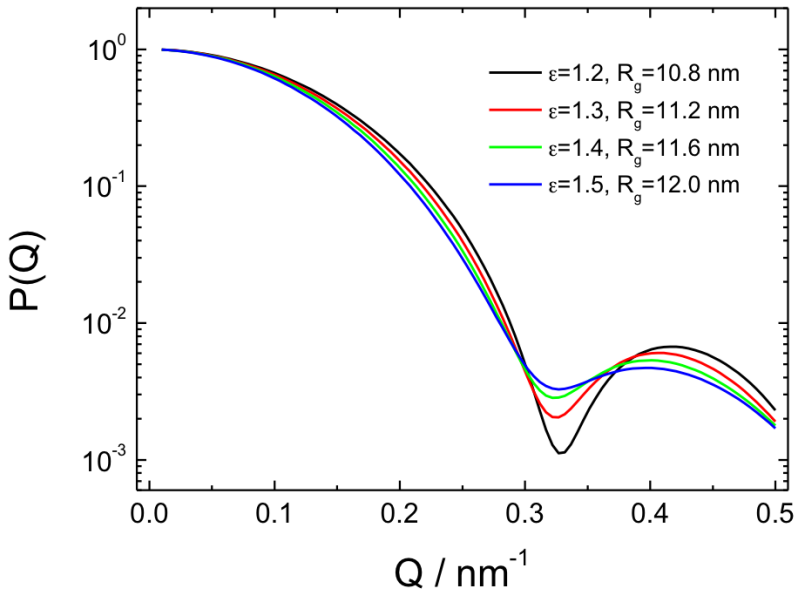

Figure 6.6: *Model calculations for the particle scattering factor of a prolate ellipsoid of revolution with elipticities and radii of gyration as indicated in the legend.*

The fact that the position of the minima in the SAXS curves does not change with salt concentration can not be explained with this model in a straight forward manner. However, the first minimum of the particle scattering factor of prolate ellipsoids of revolution is rather insensitive to the ellipticity, ε of the particle at $\varepsilon \geq 1.2$. This is shown in Fig. 6.6 where particle scattering factors for ellipsoids of revolution [106] are plotted for $1.2 \leq \varepsilon \leq 1.5$ covering a range of radii of gyration which is comparable to the values observed in the SAXS experiments.
From these model calculations it is obvious that the position of the minimum in the scattering curve does hardly change with elipticity, but it is very pronounced at small ε an becomes more shallow with increasing ε. This reflects qualitatively the evolution of the experimental curves

shown in Fig. 6.5, where the data obtained at the smallest NaCl concentration, which result the smallest value of ρ show the most pronounced minimum and vice versa.

6.4 Encapsulation behavior of amphiphilic pre-polymers

Amphiphilic polymers have been shown to be able to encapsulate hydrophobic components [107], which is of high relevance in practical applications. The amphiphilic contains a high amount of carboxylic acid group, i. e. 8 wt% in the case of 228, which in the long run will increase water absorption of a coating product and hamper its performance. [108]. Hence it is of practical importance to lower the content of acid group while maintaining the stability of dispersion. Using amphiphilic pre-polymers to encapsulate hydrophobic counterparts could be one potential strategy for the purpose. The self-,co-assembly behavior of amphiphilic polyurethane pre-polymers have been discussed in the previous sections. As shown above, amphiphilic pre-polymers assemble into colloidal particles in aqueous solution, which are of almost perfect spherical shape at low ionic strength. With increasing salt concentration they develop into prolate ellipsoids which are stable against further aggregation up to salt concentration of 50 mM. Only at a content of 100 mM NaCl the dispersions show signs of colloidal instability.
In this section, we are going to test out the encapsulation behavior of two kinds of amphiphilic pre-polymers. One is the 228 with random unit sequence; the other is molecularly designed Micropure with specific sequence. We are trying to answer the following questions: How many parts of amphiphilic pre-polymers are needed to successfully encapsulate one part of hydrophobic pre-polymers? What is the size and polydispersity of the encapsulated particles? Will there be a difference between the random and molecularly designed , when it comes encapsulation performance?

6.4.1 228 encapsulating 229

To study the encapsulation performance of amphiphilic pre-polymers 228, we prepare a series of dispersion with different hydrophilic/hydrophobic ratio, from 1:1 to 1:10. Fig.6.7 show a picture of dispersion at ratio 1:1 on the far left. Irreversible aggregation is found at the bottom of vials after shaking for 24 hours. It is clear that at this ratio, amphiphilic can hardly encapsulate the hydrophobic part. As we slowly increase the ratio, less aggregation is found. At the mixing mass ratio of m(228):m(229) = 5:1, we start to observe a homogeneous colloidal dispersion as shown in Fig. 6.7, thus this composition is taken as a threshold for successful

encapsulation. The following experiments are conducted at this mass ratio of 5:1. Stock so-

Figure 6.7: *Dispersions of 228-229 at various weight ratios of amphiphilic 228 over hydrophobic 229. From left to right: m(228):m(229) = 1:1, 5:1, 8:1, 10:1.*

lution is diluted into 0.1 mg/ml, 0.05 mg/ml, 0.02 mg/ml and 0.01 mg/ml at different salt concentration. Three representative salt concentrations have been chosen, from relatively low salt c_{NaCl}= 1 mM, to high salt 100 mM. Dynamic light scattering is conducted and correlation functions are analyzed via cumulant method, since a certain degree of polydispersity is expected. The method is described in Chapter 2 in detail. The apparent hydrodynamic radius $R_{H,app}$ is derived through Stokes-Einstein equation from diffusion coefficient, which is averaged over a series of scattering vectors. The polydispersity index at scattering angle of 90°was calculated by cumulant analysis using the second moment of the second order fitting, given by $PDI = \mu_2/\langle\Gamma\rangle^2$. Table 6.4 shows the result of dynamic light scattering. $R_{H,app}$ of 228-229 particles is around 120 nm and increases slightly with decreasing concentration, which is expected due to the particle particle interaction. Particles are stable against salt up till 100 mM NaCl, although the dependence of the apparent hydrodynamic radius $R_{H,app}$ on salt concentration is less clear.

Table 6.4: *Apparent hydrodynamic radius $R_{H,app}$ (nm) of encapsulated particles: 229 in 228*

C_{NaCl}(mM)	C_{PP}(mg/ml)	R_H(nm)	PDI
100	0.1	128	0.324
100	0.05	122	0.353
100	0.02	127	0.384
100	0.01	202	0.368
10	0.1	127	0.313
10	0.05	130	0.494
10	0.02	123	0.465
10	0.01	144	0.575
1	0.1	115	0.425
1	0.05	126	0.322
1	0.02	135	0.360
1	0.01	134	0.364

6.4.2 Micropure encapsulating 229

In the next step, we investigated the encapsulation properties of Micropure pre-polymers over hydrophobic pre-polymers 229. Micropure is a pure substance with well defined molecular structure, which can serve as a PU model system and therefore facilitate the comparison with potential theoretical predictions. To start with, we mix Micropure and 229 pre-polymers at the mass ratio of m(Micropure):m(229)=5:1, which in the case of 228-229, is the threshold for successful encapsulation. Similar to 228-229, we observe a homogeneous dispersion for MP-229 at this mixing ratio, and the solution is further diluted for the following measurements.
The hydrodynamic radius of MP-229 particles are show in Table 6.5, at different salt concentrations. At low salt concentration, 1 mM and 10 mM, the R_H of MP-229 is similar to that of 228-229, and the size distribution is narrower in the former case compared to the latter. This is an indication that the encapsulation of PP229 with the Micropure produces more homogeneous emulsions than with the random PP228. At high salt 100 mM, MP-229 encapsulates are significantly smaller than at lower salt concentrations and their polydispersity increases drastically; while the size and distribution of 228-229 encapsulates remain almost unchanged compared to suspensions at low salt concentration. This has to be interpreted as a drop of encapsulation efficiency of Micropure pre-polymers and the onset of colloidal instability of the MP-229 encapsulates at the highest salt concentration.

Table 6.5: *Apparent hydrodynamic radius $R_{H,app}$ (nm) of encapsulated particles: 229 in Micropure*

C_{NaCl}(mM)	C_{PP}(mg/ml)	R_H(nm)	PDI
100	0.1	79	0.479
100	0.05	93	0.451
100	0.02	94	0.406
100	0.01	95	0.394
10	0.1	131	0.221
10	0.05	129	0.204
10	0.02	129	0.191
10	0.01	128	0.221
1	0.1	133	0.194
1	0.05	131	0.212
1	0.02	133	0.263
1	0.01	134	0.255

6.5 Near-wall dynamics of encapsulated particles

In the previous sections, we have investigated the self-,co-organization behavior of amphiphilic pre-polymers, and the encapsulation efficiency of two kinds of amphiphilic pre-polymers over the hydrophobic ones. These studies are conducted in bulk. As coating process happens at liquid-solid interface, it would be both interesting and informative to know, how the interface influences the dynamics of the particles. For this purpose, we applied evanescent wave dynamic light scattering to polyurethane dispersion.

We have limited the study within the diluted regime because of of the dual complexity of technique and subject. The mass ratio of amphiphilic pre-polymers over hydrophobic pre-polymers is kept at 5:1. Three salt concentrations were chosen: 10^{-5}M, 10^{-3}M and 10^{-2}M, which correspond to ionic strength of 96 nm, 9.6 nm and 3 nm. At each salt concentration, three penetration depths were chosen: 111 nm, 143 nm and 216 nm, respectively. First, we compared the normalized Γ of particles to that of hard sphere prediction, as shown in Fig. 6.8. Both 228-229 and MP-229 show significantly slower dynamics with respect to hard sphere prediction. The slow-down is such that the difference induced by electrostatic interaction is almost indistinguishable in the plot. It might be explained by the strong absorption of particles onto glass surfaces. Although, it seems that the near-wall dynamics of MP-229 is more sensitive towards salt concentration than that of 228-229.

To quantitatively compare the near-wall dynamics of 228-229 and MP-229 at different salt concentrations and penetration depths, we try to extract the mean diffusivities from the experimental data. According to eq. 2.44, the mean diffusivities $\langle D_{\parallel,\perp} \rangle$ can be experimentally

obtained by linear fitting Γ over $Q_{\parallel,\perp}$. Fig. 6.9 show the linear fitting, represented by lines, and the experimental data, represented by symbols. The fitted value of mean diffusivities are presented in Table 6.6 and Table 6.7. In general, $\langle D_{\parallel} \rangle$ increases with penetration depth, as the influence of interface is diminished. The effect of salt concentration on the dynamics is however less obvious. As Debye length l_d decreases from 96 nm to 9.6 nm, in the case of 228-229, the value of $\langle D_{\parallel} \rangle$ fluctuates, and the direction of change depends on penetration depth; in the case of MP-229, the value of $\langle D_{\parallel} \rangle$ increases for all penetration depths.

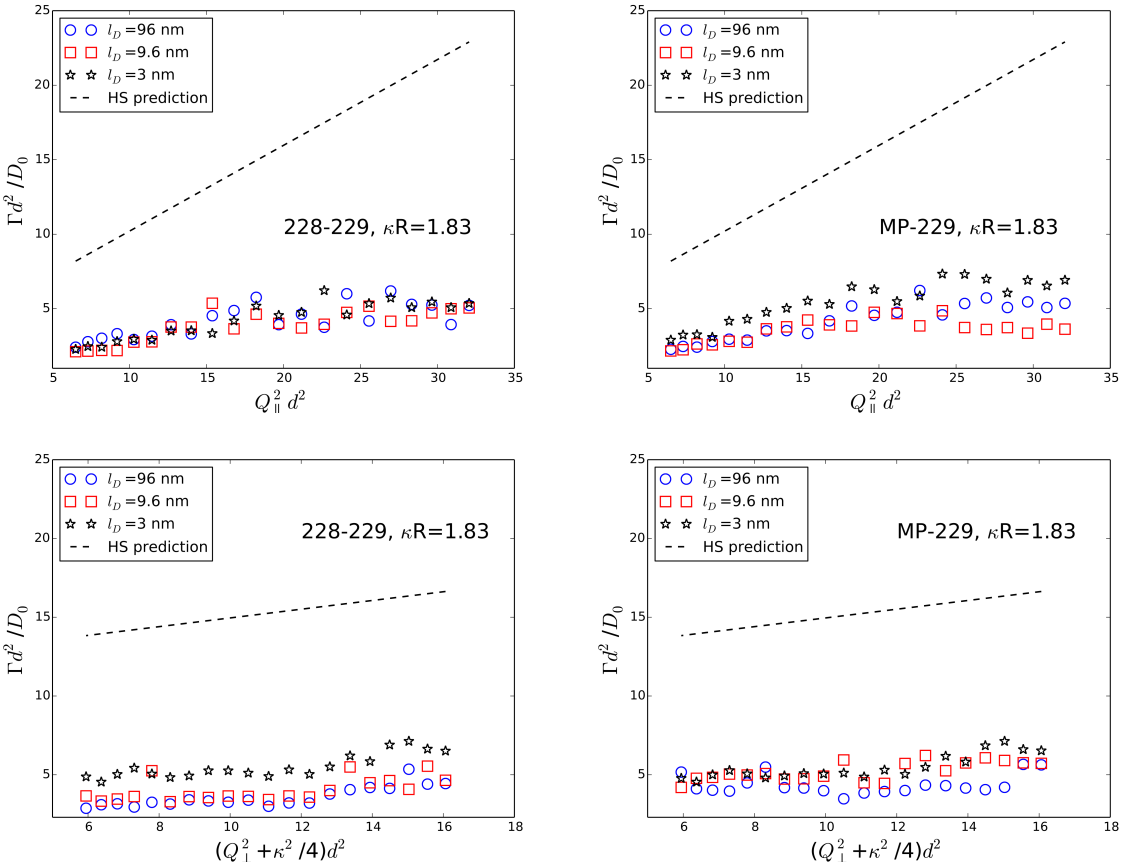

Figure 6.8: *Normalized initial relaxation rates* Γ *as a function of the scattering vector squared of encapsulated particles. Symbols represent experimental data and lines represent corresponding hard sphere prediction. Upper left:* $Q_{\parallel}$ *scan of 228-229; upper right:* $Q_{\perp}$ *scan of 228-229; lower left:* $Q_{\parallel}$ *scan of MP-229; lower right:* $Q_{\perp}$ *scan of MP-229.*

Likewise, we have obtained the $\langle D_{\perp} \rangle$ values by linear fitting Γ vs. $Q_{\perp}^2$. The data and fitting are shown in Fig. 6.10. And the corresponding $\langle D_{\perp} \rangle$ values are shown in Table 6.8 and Table 6.9. The experimental data during the perpendicular scan is much more scattered than that during the parallel scan, which makes it difficult to observe trends. Since data obtained at $\kappa a = 1.81$

is the least scattering, it is chosen as reference for comparison. In the case of MP-229, the value of $\langle D_\perp \rangle$ clearly increases with salt concentration, as shown in Table 6.9 , which agrees with the trend observed in parallel scan, shown in Table 6.7.

Table 6.6: *$\langle D_\parallel \rangle$ of 228-229, obtained from linear fitting of normalized initial relaxation rates* Γ *versus the parallel scattering vector component squared*

Penetration depth	l_d = 96 nm	l_d = 9.6 nm	l_d = 3 nm
κa=2.36	0.1424	0.09198	0.1186
κa=1.83	0.1485	0.1434	0.1852
κa=1.21	0.1676	0.1818	0.2145

Table 6.7: *$\langle D_\parallel \rangle$ of MP-229, obtained from linear fitting of normalized initial relaxation rates* Γ *versus the parallel scattering vector component squared*

Penetration depth	l_d = 96 nm	l_d = 9.6 nm	l_d = 3 nm
κa=2.36	0.1260	0.2519	0.2400
κa=1.83	0.1465	0.2211	0.2127
κa=1.21	0.1902	0.2510	0.2653

Table 6.8: *$\langle D_\perp \rangle$ of 228-229, obtained from linear fitting of normalized initial relaxation rates* Γ *versus the parallel scattering vector component squared*

Penetration depth	l_d = 96 nm	l_d = 9.6 nm	l_d = 3 nm
κa=2.36	0.06825	0.01568	0.05318
κa=1.83	0.1668	0.1292	0.1960
κa=1.21	0.1549	0.1223	0.03045

Table 6.9: *$\langle D_\perp \rangle$ of MP-229, obtained from linear fitting of normalized initial relaxation rates* Γ *versus the parallel scattering vector component squared*

Penetration depth	l_d = 96 nm	l_d = 9.6 nm	l_d = 3 nm
κa=2.36	0.04116	0.05587	0.07185
κa=1.83	0.03620	0.1347	0.2022
κa=1.21	0.08669	0.1298	0.1090

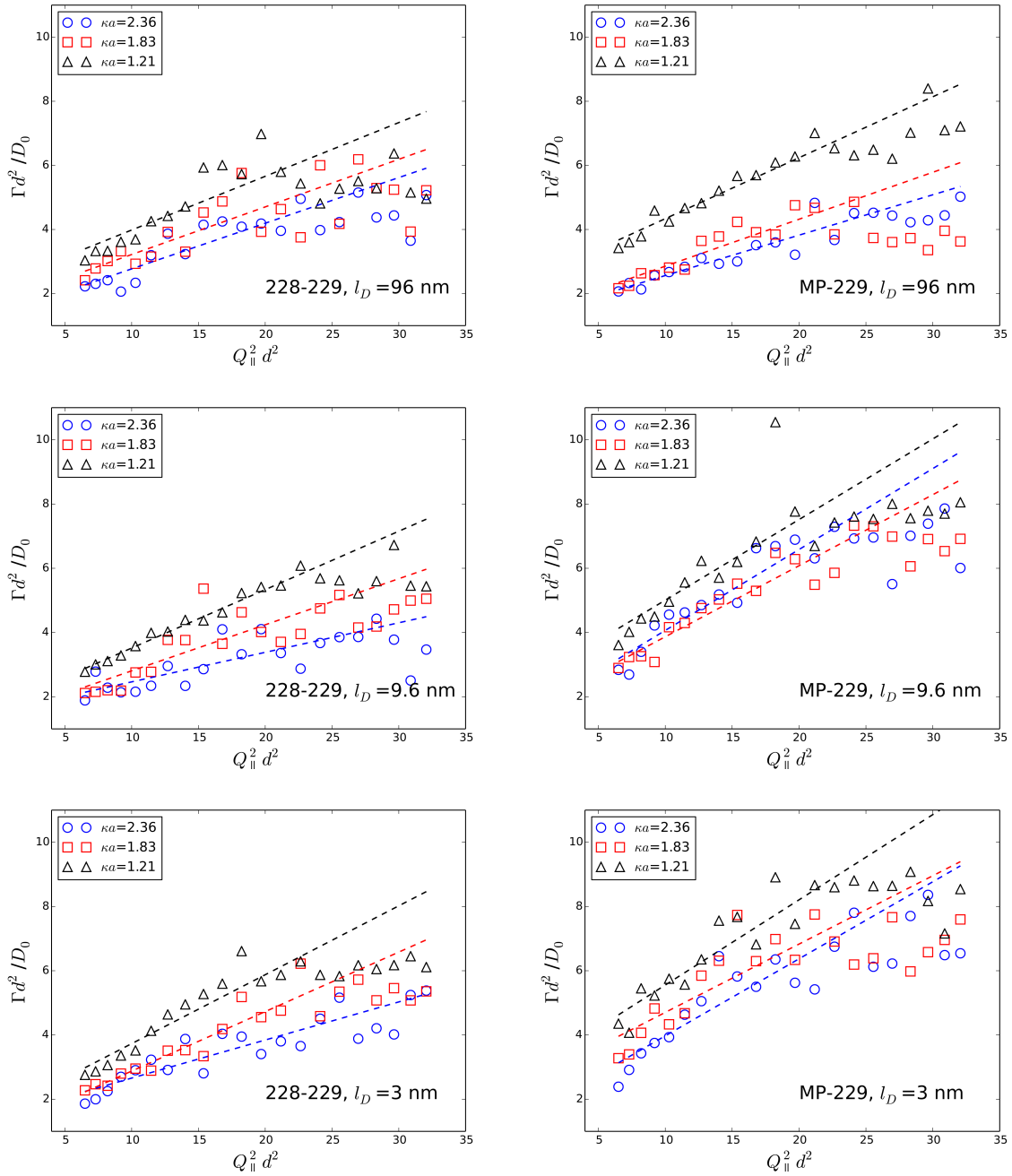

Figure 6.9: *Normalized initial relaxation rates* Γ *as a function of the parallel scattering vector component squared* $Q_\parallel^2$ *of 228-229 and MP-229at various salt concentration and penetration depth as indicated in the graph. Symbols represent experimental data and lines show the linear fitting (high-Q range is not included in the fitting due to back reflection error). Upper left: 228-229 with 0 mM NaCl; upper right: MP-229 with 0 mM NaCl; middle left: 228-229 with 1 mM NaCl; middle right: MP-229 with 1 mM NaCl; lower left: 228-229 with 10 mM NaCl; lower right: MP-229 with 10 mM NaCl.*

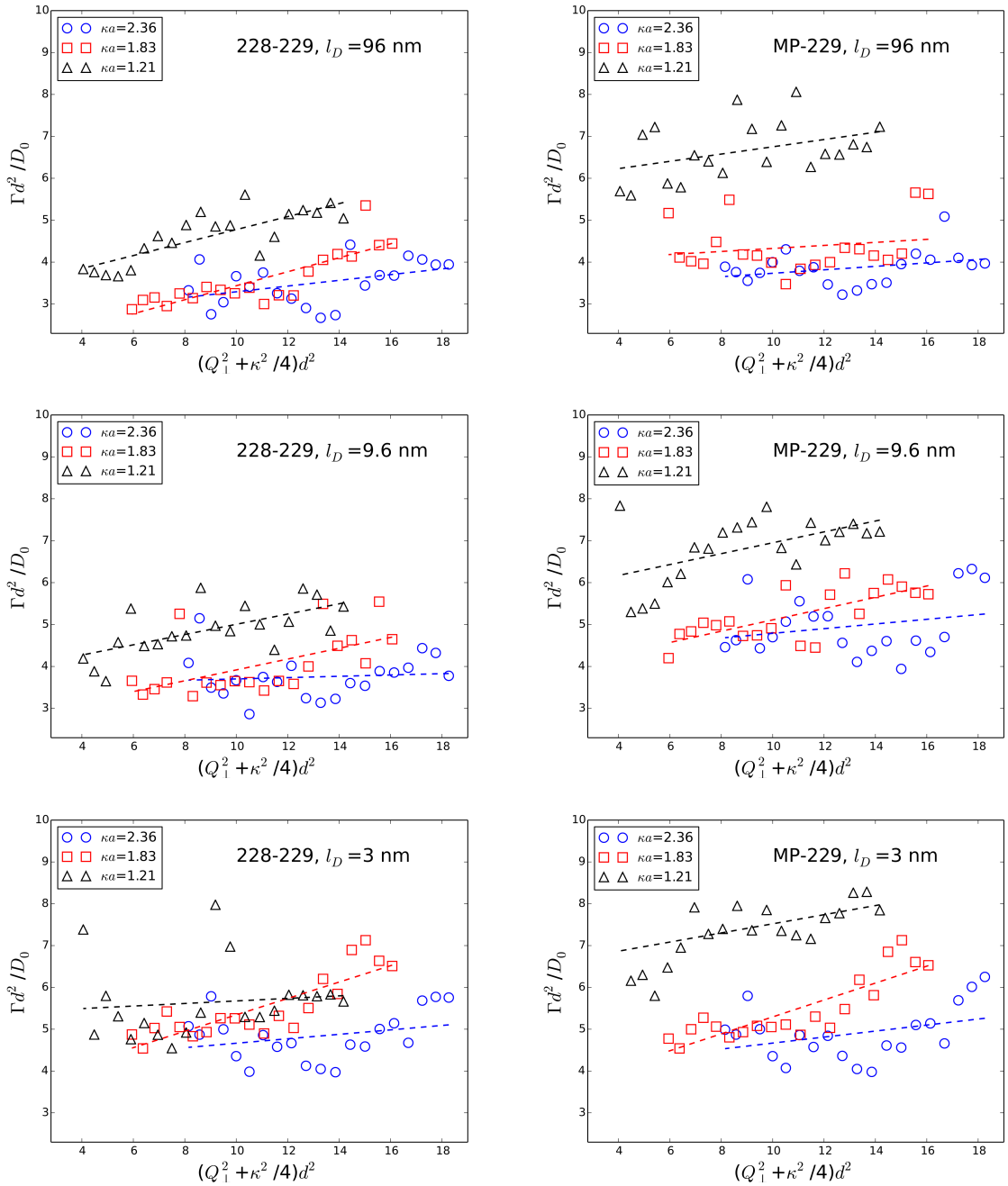

Figure 6.10: *Normalized initial relaxation rates* Γ *as a function of the perpendicular scattering vector component squared* $Q_\perp^2$ *of 228-229 and MP-229, at various salt concentration and penetration depth as indicated in the graph. Symbols represent experimental data and lines represent linear fitting (high-Q range is not included in the fitting due to back reflection error). Upper left: 228-229 with 0 mM NaCl; upper right: MP-229 with 0 mM NaCl; middle left: 228-229 with 1 mM NaCl; middle right: MP-229 with 1 mM NaCl; lower left: 228-229 with 10 mM NaCl; lower right: MP-229 with 10 mM NaCl.*

6.6 Conclusion

Water-born polyurethane is a promising material for eco-friendly coating application. The structure and property of colloidal dispersion play an important role for the performance of final products. In this chapter, we have systematically studied the self-,co-organization behavior of polyurethane pre-polymers and their dynamics in the bulk and at the liquid-solid interface.

In the first section, we studied an industrial grade amphiphilic polyurethane 228, by SLS, DLS and SAX. In aqueous solution, the pre-polymers self-,co-organize into sphere-shaped colloidal particles with a radius around 10 nm at low salt concentrations. Upon increasing the ionic strength, the particles become prolate ellipsoids. The colloidal dispersion is shown to be stable against further aggregation up to a salt concentration of 50 mM NaCl and only at a salt concentrations of 100 mM first signs of colloidal instability are observed.

In the second section, we used such amphiphilic pre-polymers to encapsulate hydrophobic pre-polymers, with the aim of reducing the total amount of acid group in the colloidal dispersion, while maintaining a stable particle system. Two different amphiphilic pre-polymers are studied here: industrial grade 228 with random sequence, as studied previously; and molecular-designed Micropure with specific unit sequence. At the weight ratio of 5:1, both amphiphilic pre-polymers succeed in encapsulating the hydrophobic counterparts, resulting in a homogeneous colloidal dispersion. The encapsulates have a radius around 120 nm. At low to medium salt concentration, Micropure encapsulates (MP-229) have a polydispersity of 0.2, while the random encapsulates (228-229) show a polydispersity of 0.4. This indicates that Micropure pre-polymers have better encapsulating properties at low and medium ionic strength.

In the last section, the near-wall dynamics of both 228-229 and MP-229 are studied by EWDLS. The motion of the encapsulated particles is significantly slower than that of hard spheres, which indicates absorption between particles and interface. The influence of ionic strength is not conclusive, although we observe that near-wall dynamics of MP-229 are more sensitive towards the change of ionic strength than that of 228-229.

7 Summary and Outlook

The motion of particles at interfaces is an essential feature in the field of colloidal science. It is highly relevant to many biological processes and industrial applications. Furthermore it offers intriguing insights when investigating fundamental questions. In this work, an attempt has been made to address this fundamental yet important question of how the liquid-solid interface influences the Brownian motion of colloidal particles. In order to answer this question the following points need to be addressed: improvement of the experimental technique – evanescent wave dynamic light scattering, finding a supporting theoretical description and a good colloidal model system.

7.1 Summary

Chapter 2 lays out the fundamental concepts used in this thesis, from standard light scattering techniques (DLS and SLS) to more complicated themes, such as Brownian motion at planar wall and light scattering at evanescent illumination. These fundamentals prepare the ground for further theoretical development.

In Chapter 3, a detailed description of the experimental method - evanescent wave dynamic light scattering (EWDLS) is given, including instrumentation, alignment procedure, evaluation of correlation functions, data reproducibility and error estimation. Through the improved alignment procedure introduced in this thesis, the reproducibility of EWDLS measurements has been largely improved. One major source of artifact has been identified as the back reflection of the totally reflected laser bean when exiting from the lens.

As near-wall dynamics is a complicated subject, it is important to validate the experimental method and define the particle systems. We start the investigation on a simple hard

sphere model system. Experimental results over a wide range of volume fractions have been conducted and compared with predictions based on virial approximation and numerical simulation, and reasonable agreement has been achieved.

In the next step, we applied EWDLS to an aqueous model system, with tunable interaction. Particles were synthesized through emulsion polymerization of fluorinated acrylate monomers, and grafted with PEG oligomers for extra stability. Subsequent characterization shows that particles adopt a core-shell spherical conformation, with a hydrodynamic radius of approximately 130 nm. Such particles can be easily refractive index matched to aqueous solvents and are stable against compression (the PEG layer prevents irreversible aggregation due to Van-der-Waals forces), which make measurements at higher volume fraction possible. Static light scattering shows that the salt free particle dispersions reach the isotropic-crystalline transition at a volume fraction as low as 7%, due to long-range electrostatic interaction.

At low volume fractions, e.g $\phi \approx 1\%$, the near-wall dynamics can be explained by a combination of the hydrodynamic wall effect and electrostatic potential, where only the interaction between particles and the interface is considered, and particle-particle interaction is ignored. A linear dependence of relaxation rates Γ over the scattering vector squared $Q_{\|}^2$ is observed experimentally and quantitatively described. However, as the volume fraction increases, the near-wall dynamics quickly deviate from this simple depiction. Starting from ϕ=5 %, a slight undulation is observed along the curve of relaxation rate Γ versus scattering vector squared $Q_{\|}^2$. The undulation gets more pronounced as the volume fraction approaches the transition value of 7%. Moreover, near-wall dynamics and bulk dynamics are compared over the entire experimentally accessible Q range. We see that, the difference diminishes with increasing volume fraction.

Finally, we applied bulk scattering methods and EWDLS to an industrial sample, i.e. aqueous suspension of polyurethane prepolymers, which is the precursor for water-borne coating applications. Due to their amphiphilic nature, the prepolymers can self-organize into micelle-like particles with a radius about 10 nm in aqueous solution. Such particles are relatively mono-disperse and stable against salt up till an ionic strength of 50 mM. Moreover, the amphiphilic prepolymers are able to encapsulate hydrophobic counterparts, and form homogeneous particle suspension at the threshold mass ratio of m(amphiphilic):m(hydrophobic) = 5:1. The encapsulated particles have a radius of about 130 nm and show a significant degree of polydispersity. The near-wall dynamics of these encapsulated particles are studied by EWDLS. We have obtained reasonable correlation functions and reproducible linear Γ vs. Q^2 dependence. Although the results are not yet conclusive, we find some distinctive features in this system, one of which is that the motion of PU particles are significantly slower than hard

sphere predictions.

7.2 Outlook

Improvement of the EWDLS instrumentation would open up various avenues to future work. For example, the addition of a shear-cell unit at the sample stage will enable EWDLS measurements under shear, which in the long run could be applicable for quality monitoring under industrial processing conditions; a temperature unit will allow measurements of thermosensitive samples at interfaces; a magnetic unit, as simple as a pair of Helmholtz coils, combined with commercially available super-paramagnetic particles will make it possible to look at near-wall dynamics of particles in a magnetic field.

The promising results on bulk and near-wall dynamics of the aqueous model system call for future investigations. First of all, the static light scattering results in bulk, such as the structure factor $S(Q)$ dependence on the volume fraction ϕ, may be compared to current theoretical predictions, in order to gain more insight into the system.

Secondly, a systematic investigation of the bulk dynamics is needed, with variations on both volume fraction and ionic strength. One interesting question is the bulk dynamics of particle suspensions in the ordered regime above $\phi \approx 10\%$, where we clearly observe an opalescent appearance of the particle suspension. Such studies on bulk dynamics will not only contribute to the current knowledge on aqueous colloidal systems, but will also help us better understanding their near-wall dynamics.

The third and most important aspect is to devise a quantitative theoretical description for the near-wall dynamics of the aqueous model systems. At volume fractions higher than 1%, only phenomenological explanations are given for the experimental observations in this thesis. Theoretical descriptions that allow predictions for a variety of interaction types and ranges are still needed.

As seen in Chapter 6 and from the work by Loppinet *et al.* [25] on near-wall Doppler velocimetry, evanescent wave dynamic light scattering has a high potential for industrial applications. However, there is still a long way to go before this interface method is technology ready. Some major issues to be addressed are: how to take sample size polydispersity into account, which is inevitable in most industrial cases; how to routinize and automatize the data acquisition and analysis; how to reduce the required measurement time.

List of Figures

List of Tables

Acknowledgements

First of all, I would like to express my sincere gratitude to my supervisor Peter R. Lang, who hired me and trusted me with this nice research project. During these three years, Peter has not only guided me through the project patiently, but also given me great freedom to develop and implement my own ideas. Peter is willing to give encouragement as well as criticism, which has helped me improve my scientific and presentation skills.

I would like to thank Prof. Jan K.G Dhont for hosting me in ICS-3 during my Ph.D, where I have been given a lot of scientific freedom and support.

I want to thank Prof. Matthias Karg, for his acceptance to review my thesis.

I thank for the support from Marie Sklodowska Curie initial Training network SOMATAI under the EU Grant Agreement No.316866. I would also like to thank the Ph.D fellows and supervisors within SOMATAI network, especially Dr. Reinhard Sigel and Dr. Benoit Loppinet for their helpful advices on EWDLS.

I thank Dr. Ilse van Casteren and Dr. Li Feng for the nice collaboration on the polyurethane project and for providing me with PU samples.

I thank Dr. Christoph July for helping me with physics and programming.

I would like to thank the whole ICS-3 for providing a nice working atmosphere and right distractions at the right time. I thank Marie and Ulrike for help with all bureaucratic issues and daily life problems, which is in particular important to me, as a foreigner living in Germany. I thank Hartmut, Simone and Johan for many helpful discussion and general kindness. I thank Gerhard for helpful theoretical input. I thank Doreen, for her willingness to put ego aside and engage in productive discussion, on top of being awesome (cite[Niether *et al.*]). I thank Blandine for her sincere and uncompromising attitude, as well as her crêpe recipe. I have to thank Mariano for the solidarity and friendship during a 10-hour flight delay we lived through.

And I sincerely thank Oli for the nice parties and pumpkin cakes.
I would like to thank my family and friends for sharing the ups and downs with me during these three years.

Bibliography

[1] Peter R. Lang and Yi Liu, editors. *Soft Matter at Aqueous Interfaces*. Lecture Notes in Pysics. Springer, 2016.

[2] Leonard MC Sagis. Dynamic properties of interfaces in soft matter: Experiments and theory. *Reviews of Modern Physics*, 83(4):1367, 2011.

[3] Hartmut Löwen. Colloidal soft matter under external control. *Journal of Physics: Condensed Matter*, 13(24):R415, 2001.

[4] To Ngai and Stefan Bon, editors. *Particle-Stabilized Emulsions and Colloids*. RSC Soft Matter Series. The Royal Society of Chemistry, 2015.

[5] J. D. Andrade and V. Hlady. *Biopolymers/Non-Exclusion HPLC*, chapter Protein adsorption and materials biocompatibility: A tutorial review and suggested hypotheses, pages 1–63. Springer Berlin Heidelberg, Berlin, Heidelberg, 1986.

[6] Linfeng Hu, Min Chen, Xiaosheng Fang, and Limin Wu. Oil–water interfacial self-assembly: a novel strategy for nanofilm and nanodevice fabrication. *Chemical Society Reviews*, 41(3):1350–1362, 2012.

[7] ML Zheludkevich, J Tedim, and MGS Ferreira. Smart coatings for active corrosion protection based on multi-functional micro and nanocontainers. *Electrochimica Acta*, 82:314–323, 2012.

[8] In Woo Cheong and Jung Hyun Kim. Synthesis of core-shell polyurethane-urea nanoparticles containing 4,4[prime or minute]-methylenedi-p-phenyl diisocyanate and

isophorone diisocyanate by self-assembled neutralization emulsification. *Chem. Commun.*, 21:2484–2485, 2004.

[9] Pramod Mathai. *Encyclopedia of Microfluidics and Nanofluidics*, chapter Brownian Motion in Microfluidics and Nanofluidics, pages 213–218. Springer New York, New York, NY, 2015.

[10] David M. Kaz, Ryan McGorty, Madhav Mani, Michael P. Brenner, and Vinothan N. Manoharan. Physical ageing of the contact line on colloidal particles at liquid interfaces. *Nature Materials*, 11(2):138–142, 2011.

[11] E. M. Herzig, K. A. White, A. B. Schofield, W. C. K. Poon, and P. S. Clegg. Bicontinuous emulsions stabilized solely by colloidal particles. *Nature Materials*, 6(12):966–971, 2007.

[12] Maxsim L Gibiansky, Jacinta C Conrad, Fan Jin, Vernita D Gordon, Dominick a Motto, Margie a Mathewson, Wiktor G Stopka, Daria C Zelasko, Joshua D Shrout, and Gerard C L Wong. Bacteria use type IV pili to walk upright and detach from surfaces. *Science*, 330(October):197, 2010.

[13] Ingmar H Riedel, Karsten Kruse, and Jonathon Howard. A self-organized vortex array of hydrodynamically entrained sperm cells. *Science*, 309(5732):300–303, 2005.

[14] Darsh T. Wasan and Alex D. Nikolov. Spreading of nanofluids on solids. *Nature*, 423:156–159, 2003.

[15] Darsh T. Wasan, Alex D. Nikolov, Andrij Trokhymchuck, and Douglas J. Henderson. *Encycopedia of Surface and Colloidal Science*, chapter Confinement-Induced Structural Forces in Colloidal Systems, page 1485. CRC Press Taylor and Francis, Boca Raton, FL, 2006.

[16] Dzina Kleshchanok, Remco Tuinier, and Peter R Lang. Direct measurements of polymer-induced forces. *Journal of Physics: Condensed Matter*, 20(7):073101, 2008.

[17] H Löwen. Twenty years of confined colloids: from confinement-induced freezing to giant breathing. *Journal of Physics: Condensed Matter*, 21(47):474203, 2009.

[18] MIM Feitosa and ON Mesquita. Wall-drag effect on diffusion of colloidal particles near surfaces: a photon correlation study. *Physical Review A*, 44(10):6677, 1991.

[19] N. Garnier and N. Ostrowsky. Brownian dynamics in a confined geometry. experiments and numerical simulations. *J. Phys. II*, 1:1221–1232, 1991.

[20] M. Hosoda, K. Sakai, and K. Takagi. Measurement of anisotropic brownian motion near an interface by evanescent light-scattering spectroscopy. *Phys. Rev. E*, 58:6275–6280, 1998.

[21] Binhua Lin, Jonathan Yu, and Stuart A. Rice. Direct measurements of constrained brownian motion of an isolated sphere between two walls. *Phys. Rev. E*, 62(3):3909–3919, 2000.

[22] Peter Holmqvist, Jan K. G. Dhont, and Peter R. Lang. Anisotropy of brownian motion caused only by hydrodynamic interaction with a wall. *Phys. Rev. E*, 74(2):021402, 2006.

[23] Peter Holmqvist, Jan K G Dhont, and Peter R Lang. Colloidal dynamics near a wall studied by evanescent wave light scattering: experimental and theoretical improvements and methodological limitations. *J. Chem. Phys.*, 126(4):044707, 2007.

[24] V. Michailidou, G. Petekidis, J. Swan, and J. Brady. Dynamics of Concentrated Hard-Sphere Colloids Near a Wall. *Phy. Rev. Lett.*, 102(6):068302, feb 2009.

[25] B Loppinet, JKG Dhont, and P Lang. Near-field laser doppler velocimetry measures near-wall velocities. *The European Physical Journal E*, 35(7):1–4, 2012.

[26] Eleutheria Antoniou, Panayiotis Voudouris, Antje Larsen, Benoit Loppinet, Dimitris Vlassopoulos, Isabel Pastoriza-Santos, and Luis M Liz-Marzán. Static and dynamic plasmon-enhanced light scattering from dispersions of polymer-grafted silver nanoprisms in the bulk and near solid surfaces. *The Journal of Physical Chemistry C*, 116(6):3888–3896, 2012.

[27] V. N. Michailidou, J. W. Swan, J. F. Brady, and G. Petekidis. Anisotropic diffusion of concentrated hard-sphere colloids near a hard wall studied by evanescent wave dynamic light scattering. *J. Chem. Phys.*, 139(16), 2013.

[28] Yi Liu, Jerzy Bławzdziewicz, Bogdan Cichocki, Jan K. G. Dhont, Maciej Lisicki, Eligiusz Wajnryb, Y.-N. Young, and Peter R. Lang. Near-wall dynamics of concentrated hard-sphere suspensions: comparison of evanescent wave DLS experiments, virial approximation and simulations. *Soft Matter*, 11(37):7316–7327, 2015.

[29] Dimitris Sofikitis, Lykourgos Bougas, Georgios E Katsoprinakis, Alexandros K Spiliotis, Benoit Loppinet, and T Peter Rakitzis. Evanescent-wave and ambient chiral sensing by signal-reversing cavity ringdown polarimetry. *Nature*, 514(7520):76–79, 2014.

[30] Howard Brenner. The slow motion of a sphere through a viscous fluid towards a plane surface. *Chemical engineering science*, 16(3-4):242–251, 1961.

[31] AJ Goldman, RG Cox, and H Brenner. Slow viscous motion of a sphere parallel to a plane wall- couette flow. *Chemical engineering science*, 22(4):653–660, 1967.

[32] Sambeeta Das, Astha Garg, Andrew Ian Campbell, Jonathan R Howse, Ayusman Sen, Darrell Velegol, Ramin Golestanian, and Stephen J. Ebbens. Boundaries can steer active Janus spheres. *Nature Communications*, Accepted:1–10, 2015.

[33] J Elgeti, R G Winkler, and G Gompper. Physics of microswimmers–single particle motion and collective behavior: a review. *Rep. Prog. Phys.*, 78(5):056601, 2015.

[34] Binhua Lin, Jonathan Yu, and Stuart A Rice. Direct measurements of constrained brownian motion of an isolated sphere between two walls. *Physical Review E*, 62(3):3909, 2000.

[35] Peter Huang and Kenneth S Breuer. Direct measurement of anisotropic near-wall hindered diffusion using total internal reflection velocimetry. *Physical review E*, 76(4):046307, 2007.

[36] Mauricio D Carbajal-Tinoco, Ricardo Lopez-Fernandez, and José Luis Arauz-Lara. Asymmetry in colloidal diffusion near a rigid wall. *Physical review letters*, 99(13):138303, 2007.

[37] K. H. Lan, N. Ostrowsky, and D. Sornette. Brownian dynamics close to a wall studied by photon correlation spectroscopy from an evanescent wave. *Phys. Rev. Lett.*, 57:17–20, Jul 1986.

[38] S. A. Rogers, M. Lisicki, B. Cichocki, J. K. G. Dhont, and P. R. Lang. Rotational Diffusion of Spherical Colloids Close to a Wall. *Physical Review Letters*, 109(9):098305, aug 2012.

[39] Antonio Stocco, Tahereh Mokhtari, Günter Haseloff, Andreas Erbe, and Reinhard Sigel. Evanescent-wave dynamic light scattering at an oil-water interface: Diffusion of interface-adsorbed colloids. *Phys. Rev. E*, 83:011601, Jan 2011.

[40] B. Loppinet, J. K G Dhont, and P. Lang. Near-field laser Doppler velocimetry measures near-wall velocities. *European Physical Journal E*, 35:1–4, 2012.

[41] H Cummins. *Photon correlation and light beating spectroscopy*, volume 3. Springer Science & Business Media, 2013.

[42] Jan KG Dhont. *An introduction to dynamics of colloids*, volume 2. Elsevier, 1996.

[43] Z Akcasu and H Gurol. Quasielastic scattering by dilute polymer solutions. *Journal of Polymer Science Part B: Polymer Physics*, 34(13):2117–2126, 1996.

[44] Dennis E Koppel. Analysis of macromolecular polydispersity in intensity correlation spectroscopy: the method of cumulants. *The Journal of Chemical Physics*, 57(11):4814–4820, 1972.

[45] Barbara J Frisken. Revisiting the method of cumulants for the analysis of dynamic light-scattering data. *Applied Optics*, 40(24):4087–kim–4091, 2001.

[46] Hendrik Antoon Lorentz. *Abhandlungen über theoretische Physik*. BG Teubner, 1907.

[47] Hilding Faxén. Die bewegung einer starren kugel längs der achse eines mit zäher flüssigkeit gefüllten rohres. 1923.

[48] Maciej Lisicki, Bogdan Cichocki, Simon A Rogers, Jan KG Dhont, and Peter R Lang. Translational and rotational near-wall diffusion of spherical colloids studied by evanescent wave scattering. *Soft matter*, 10(24):4312–4323, 2014.

[49] Maciej Lisicki, Bogdan Cichocki, Jan K G Dhont, and Peter R Lang. One-particle correlation function in evanescent wave dynamic light scattering. *J. Chem. Phys.*, 136(20):204704, 2012.

[50] Peter N. Pusey and W. van Megen. Phase behavior of concentrated suspensions of nearly hard colloidal spheres. *Nature*, 320:340–342, 1986.

[51] W. van Megen, R. H. Ottewill, S. M. Owens, and Peter N. Pusey. Measurement of the wave-vector dependent diffusion coefficient in concentrated particle dispersions. *J. Chem. Phys.*, 82:508–515, 1985.

[52] W. van Megen, Sylvia M. Underwood, R. H. Ottewill, Neal St. J. Williams, and Peter N. Pusey. Particle diffusion in concentrated dispersions. *Faraday Discuss. Chem. Soc.*, 83:47–57, 1987.

[53] J. W. Swan and J. F. Brady. Anisotropic diffusion in confined colloidal dispersions: The evanescent diffusivity. *J. Chem. Phys.*, 135:014701, 2011.

[54] B Cichocki, E Wajnryb, J Blawzdziewicz, J K G Dhont, and P R Lang. The intensity correlation function in evanescent wave scattering. *J. Chem. Phys.*, 132(7):074704, feb 2010.

[55] B Cichocki, ML Ekiel-Jeżewska, and E Wajnryb. Lubrication corrections for three-particle contribution to short-time self-diffusion coefficients in colloidal dispersions. *The Journal of chemical physics*, 111(7):3265–3273, 1999.

[56] Peter N Pusey. Intensity fluctuation spectroscopy of charged brownian particles: the coherent scattering function. *Journal of Physics A: Mathematical and General*, 11(1):119, 1978.

[57] PN Segre, OP Behrend, and PN Pusey. Short-time brownian motion in colloidal suspensions: Experiment and simulation. *Physical Review E*, 52(5):5070, 1995.

[58] Adolfo J Banchio and Gerhard Nägele. Short-time transport properties in dense suspensions: from neutral to charge-stabilized colloidal spheres. *The Journal of chemical physics*, 128(10):104903, 2008.

[59] Gustavo C Abade, Bogdan Cichocki, Maria L Ekiel-Jeżewska, Gerhard Nägele, and Eligiusz Wajnryb. Short-time dynamics of permeable particles in concentrated suspensions. *The Journal of chemical physics*, 132(1):014503, 2010.

[60] GK Batchelor. Brownian diffusion of particles with hydrodynamic interaction. *Journal of Fluid Mechanics*, 74(01):1–29, 1976.

[61] Jonas Riest, Thomas Eckert, Walter Richtering, and Gerhard Nägele. Dynamics of suspensions of hydrodynamically structured particles: analytic theory and applications to experiments. *Soft matter*, 11(14):2821–2843, 2015.

[62] Sangtae Kim and Seppo J Karrila. *Microhydrodynamics: principles and selected applications*. Courier Corporation, 2013.

[63] G. Nägele. *(for a more comprenhensive version)*, chapter Theory of Fluid Microstructures. Schriften des Forschungszentrum Jülich / Key Technologies, Jülich, Germany, 2008.

[64] Jerome K Percus and George J Yevick. Analysis of classical statistical mechanics by means of collective coordinates. *Physical Review*, 110(1):1, 1958.

[65] CWJ Beenakker and Peter Mazur. Self-diffusion of spheres in a concentrated suspension. *Physica A: Statistical Mechanics and its Applications*, 120(3):388–410, 1983.

[66] CWJ Beenakker and Peter Mazur. Diffusion of spheres in a concentrated suspension ii. *Physica A: Statistical Mechanics and its Applications*, 126(3):349–370, 1984.

[67] CWJ Beenakker. The effective viscosity of a concentrated suspension of spheres (and its relation to diffusion). *Physica A: Statistical Mechanics and its Applications*, 128(1):48–81, 1984.

[68] Guisheng Pan, Albert S Tse, R Kesavamoorthy, and Sanford A Asher. Synthesis of Highly Fluorinated Monodisperse Colloids for Low Refractive Index Crystalline Colloidal Arrays. 7863(22):6518–6524, 1998.

[69] Gijsberta H Koenderink, Stefano Sacanna, Chellapah Pathmamanoharan, Mircea Rasa, and Albert P Philipse. Preparation and properties of optically transparent aqueous dispersions of monodisperse fluorinated colloids. *Langmuir*, 17(20):6086–6093, 2001.

[70] Malte Wiemann, René Schneider, and Eckhard Bartsch. Synthesis of PEG-Stabilized Fluoro-Acrylate Particles and Study of their Glass Transition in Aqueous Dispersion. *Zeitschrift für Physikalische Chemie*, 226(7-8):761–778, aug 2012.

[71] Jeanette Ulama, Malin Zackrisson Oskolkova, and Johan Bergenholtz. Monodisperse PEGylated spheres: an aqueous colloidal model system. *J. Phys. Chem. B*, 118(9):2582–8, mar 2014.

[72] Malin Zackrisson Oskolkova, Anna Stradner, Jeanette Ulama, and Johan Bergenholtz. Concentration-dependent effective attractions between PEGylated nanoparticles. *RSC Adv.*, 5(32):25149–25155, 2015.

[73] Daniela Pozzi, Valentina Colapicchioni, Giulio Caracciolo, Susy Piovesana, Anna Laura Capriotti, Sara Palchetti, Stefania De Grossi, Anna Riccioli, Heinz Amenitsch, and Aldo Laganà. Effect of polyethyleneglycol (peg) chain length on the bio–nano-interactions between pegylated lipid nanoparticles and biological fluids: from nanostructure to uptake in cancer cells. *Nanoscale*, 6(5):2782–2792, 2014.

[74] W. Van Aarle, W. J. Palenstijn, J. De Beenhouwer, T. Altantzis, S. Bals, K. J. Batenburg, and J. Sijbers. The astra toolbox: a platform for advanced algorithm development in electron tomography. *Ultramicroscopy*, 157:35–47, 2015.

[75] PA Midgley and Matthew Weyland. 3d electron microscopy in the physical sciences: the development of z-contrast and eftem tomography. *Ultramicroscopy*, 96(3):413–431, 2003.

[76] P Schurtenberger. Contrast and contrast variation in neutron, x-ray and light scattering. *Neutrons, X-rays and Light: Scattering Methods Applied to Soft Condensed Matter*, 1, 2002.

[77] Malin Zackrisson, Anna Stradner, Peter Schurtenberger, and Johan Bergenholtz. Small-angle neutron scattering on a core-shell colloidal system: a contrast-variation study. *Langmuir*, 21(23):10835–10845, 2005.

[78] Jacob N Israelachvili. *Intermolecular and surface forces: revised third edition*. Academic press, 2011.

[79] Charles Tanford. *The Hydrophobic Effect: Formation of Micelles and Biological Membranes 2d Ed*. J. Wiley., 1980.

[80] Stefano Ottani, Daniele Vitalini, Fabio Comelli, and Carlo Castellari. Densities, viscosities, and refractive indices of poly (ethylene glycol) 200 and 400+ cyclic ethers at 303.15 k. *Journal of Chemical & Engineering Data*, 47(5):1197–1204, 2002.

[81] Jean-Pierre Hansen and Loup Verlet. Phase transitions of the lennard-jones system. *physical Review*, 184(1):151, 1969.

[82] Hong Seok Kang and Francis H Ree. New integral equation for simple fluids. *The Journal of chemical physics*, 103(9):3629–3635, 1995.

[83] D. C. Wang and Gast A.P. Properties of crystallizing soft sphere systems. *J. Phys.: Condens. Matter*, 11:10133 – 10141, 1999.

[84] Jacek Gapinski, G. Nägele, and A. Patkowski. Freezing lines of colloidal yukawa spheres. i. a rogers-young integral equation study. *J. Chem. Phys.*, 136:024507, 2012.

[85] Jacek Gapinski, G. Nägele, and A. Patkowski. Freezing lines of colloidal yukawa spheres. ii. local structure and characteristic lengths. *J. Chem. Phys.*, 141:124505, 2014.

[86] DK Chattopadhyay and KVSN Raju. Structural engineering of polyurethane coatings for high performance applications. *Progress in Polymer Science*, 32(3):352–418, 2007.

[87] Mariana D Banea, LFM Da Silva, and RDSG Campilho. The effect of adhesive thickness on the mechanical behavior of a structural polyurethane adhesive. *The Journal of Adhesion*, 91(5):331–346, 2015.

[88] Robert C Hale, Mark J La Guardia, Ellen Harvey, and T Matt Mainor. Potential role of fire retardant-treated polyurethane foam as a source of brominated diphenyl ethers to the us environment. *Chemosphere*, 46(5):729–735, 2002.

[89] Maged A Osman, Vikas Mittal, Massimo Morbidelli, and Ulrich W Suter. Polyurethane adhesive nanocomposites as gas permeation barrier. *Macromolecules*, 36(26):9851–9858, 2003.

[90] Prashant Jain and T Pradeep. Potential of silver nanoparticle-coated polyurethane foam as an antibacterial water filter. *Biotechnology and bioengineering*, 90(1):59–63, 2005.

[91] D Dieterich. Aqueous emulsions, dispersions and solutions of polyurethanes; synthesis and properties. *Progress in Organic Coatings*, 9(3):281–340, 1981.

[92] Karl-Ludwig Noble. Waterborne polyurethanes. *Progress in organic coatings*, 32(1):131–136, 1997.

[93] Byung Kyu Kim and Jong Cheol Lee. Waterborne polyurethanes and their properties. *Journal of Polymer Science Part A: Polymer Chemistry*, 34(6):1095–1104, 1996.

[94] B. K. Kim, T. K. Kim, and H. M. Jeong. Aqueous dispersion of polyurethane anionomers from H12MDI/IPDI, PCL, BD, and DMPA. *Journal of Applied Polymer Science*, 53(3):371–378, 1994.

[95] Ajaya K Nanda, Douglas A Wicks, Samy A Madbouly, and Joshua U Otaigbe. Effect of ionic content, solid content, degree of neutralization, and chain extension on aqueous polyurethane dispersions prepared by prepolymer method. *Journal of applied polymer science*, 98(6):2514–2520, 2005.

[96] Feng Li, Remco Tuinier, Ilse van Casteren, Ronald Tennebroek, Ad Overbeek, and Frans AM Leermakers. Self-organization of polyurethane pre-polymers as studied by self-consistent field theory. *Macromolecular Theory and Simulations*, 25(1):16–27, 2016.

[97] Stefan U Egelhaaf and Peter Schurtenberger. Micelle-to-vesicle transition: a time-resolved structural study. *Physical review letters*, 82(13):2804, 1999.

[98] Zhibo Li, Ellina Kesselman, Yeshayahu Talmon, Marc A Hillmyer, and Timothy P Lodge. Multicompartment micelles from abc miktoarm stars in water. *Science*, 306(5693):98–101, 2004.

[99] Yiyong Mai and Adi Eisenberg. Self-assembly of block copolymers. *Chemical Society Reviews*, 41(18):5969–5985, 2012.

[100] Radoslav Savić, Laibin Luo, Adi Eisenberg, and Dusica Maysinger. Micellar nanocontainers distribute to defined cytoplasmic organelles. *Science*, 300(5619):615–618, 2003.

[101] Yansen Lauw, Frans AM Leermakers, and Martien A Cohen Stuart. Self-consistent-field prediction for the persistence length of wormlike micelles of nonionic surfactants. *The Journal of Physical Chemistry B*, 107(39):10912–10918, 2003.

[102] Bruno H. Zimm. Apparatus and methods for measurement and interpretation of the angular variation of light scattering; preliminary results on polystyrene solutions. *J. Chem. Phys.*, 16:1099, 1948.

[103] A. Guinier and G. Fournet. *Small Angle Scattering of X-Rays*. Wiley, 1955.

[104] W Burchard, M Schmidt, and WH Stockmayer. Influence of hydrodynamic preaveraging on quasi-elastic scattering from flexible linear and star-branched macromolecules. *Macromolecules*, 13(3):580–587, 1980.

[105] Walther Burchard. Static and dynamic light scattering from branched polymers and biopolymers. In *Light scattering from polymers*, pages 1–124. Springer, 1983.

[106] André Guinier. La diffraction des rayons x aux tres petits angles: applications a l'etude de phenomenes ultramicroscopiques. 1939.

[107] S. a. Jenekhe. Self-Assembled Aggregates of Rod-Coil Block Copolymers and Their Solubilization and Encapsulation of Fullerenes. *Science*, 279(5358):1903–1907, 1998.

[108] Elena Jubete, Christopher M. Liauw, and Norman S. Allen. Water uptake and tensile properties of carboxylated styrene butadiene rubber based water born paints: Models for water uptake prediction. *Progress in Organic Coatings*, 59(2):126–133, 2007.

Erklärung

Ich versichere an Eides statt, dass die Dissertation von mir selbstständig und ohne unzulässige fremde Hilfe unter Beachtung der "Grundsätze zur Sicherung guter wissenschaftlicher Praxis an der Heinrich-Heine-Universität Düsseldorf" erstellt worden ist.
Des Weiteren wurde die Dissertation in der vorgelegten oder in ähnlicher Form noch bei keiner anderen Institution eingereicht, und ich habe bisher keine erfolglosen Promotionsversuche unternommen.

_____
Yi Liu